

INVESTIGATIONS IN PHASE STABILITY AND MECHANICAL ATTRIBUTES  
IN NICKEL-RICH NITINOL WITH AND WITHOUT  
HAFNIUM ADDITIONS

by

BILLY CHAD HORNBUCKLE

GREGORY B. THOMPSON, COMMITTEE CHAIR  
AMBER GENAU  
YUEBIN GUO  
RONALD D. NOEBE  
MARK L. WEAVER

A DISSERTATION

Submitted in partial fulfillment of the requirements  
for the degree of Doctor of Philosophy  
in the Department of Metallurgical Engineering  
in the Graduate School of  
The University of Alabama

TUSCALOOSA, ALABAMA

2014

Copyright Billy Chad Hornbuckle 2014  
ALL RIGHTS RESERVED

## ABSTRACT

In this work, the phase stability and mechanical attributes in Ni-rich Nitinol with and without Hf additions are investigated through an array of microanalysis techniques. The work has two distinct areas of interest: (1) establishing the structure-properties relationship for a slightly Ni-rich ternary shape memory alloy with macro-additions of Hf for use as solid-state actuators and (2) determining the primary strengthening mechanisms and its compositional limit in very Ni-rich alloys with and without solute additions of Hf for bearing applications. For the first area of interest, a 50.3Ni-29.7Ti-20Hf (at.%) alloy was aged at 550°C out to 300 hours. The shape memory transformation temperature and mechanical response were measured for samples aged to specified times with the microstructure yielding these transformation temperatures and mechanical response characterized via transmission electron microscopy and atom probe tomography. These instruments allowed for the role precipitation plays to be thoroughly established while resolving the optimal microstructure by determining precipitate number density, size, and composition. The alloy exhibited near optimum response for thermal and dimensional stability after aging for three hours.

The second area of interest focused on the lesser studied systems of very Ni-rich alloys with their extremely low transformation temperature. However they possess high hardness values on par with tool steels, corrosion resistance, and stably non-magnetic behavior making them promising candidates for bearing applications. A 55Ni-45Ti (at.%) alloy, initial found to possess such hardness, had its strengthening mechanism elucidated. The alloy was solutionized and aged

at 400°C to 300 hours with no considerable drop in hardness registered. This consistent hardness was revealed to be the result of a microstructure composed of a high volume fraction of Ni<sub>4</sub>Ti<sub>3</sub> precipitates within narrow channels of B2 matrix. Generalized stacking fault energies for the two phases composing the microstructure were determined confirming the difficulty to slip in such a microstructure.

The second study focusing on these bearing alloys was investigation of the compositional limit of this strengthening mechanism for a series of Ni-rich binary compositions ranging from 53NiTi to 58NiTi (at.%) solutionized and aged at various times and temperatures. The alloy set was found to increase in hardness with increasing Ni content until reaching a maximum at 56NiTi with its hardness equivalent to the 55NiTi alloy. This hardness was contributed to a high volume fraction of Ni<sub>4</sub>Ti<sub>3</sub> precipitates encased in narrow B2 matrix channels. Additionally, the precipitation sequence of these lesser studied Ni-rich alloys was observed at 625° and 750°C to better establish the decomposition pathways between the secondary precipitates phases.

Finally, a set of Ni-rich ternary alloys with solute additions of Hf were investigated to ascertain their practicality as second generation bearing alloys. The alloys containing 1-2% Hf were found to have a traditional parabolic aging behavior with hardness below those of binary 55NiTi and 56NiTi, interestingly the H-phase precipitates formed after extended aging at 400°C. The precipitation of H-phase appears to alter the typical precipitation sequence seen in Ni-rich alloys and expands the compositional limits of H-phase. Finally, the 4% Hf containing alloy's hardness was greater than 55NiTi and further increased with aging. This behavior was the result of H-phase forming in the narrow channels of B2 matrix phase seen in the binary alloy versions.

## DEDICATION

This dissertation is dedicated to my entire family, specifically my parents and grandparents, my fiancé, and close friends who supported me through my entire educational journey finishing with the completion of this manuscript.

## LIST OF ABBREVIATIONS AND SYMBOLS

APT	Atom Probe Tomography
at.%	Atomic Percent
BF	Bright Field
BSE	Back Scattered Electron
CAF	Central Analytical Facility
DSC	Differential Scanning Calorimetry
EBSD	Electron Backscattered Diffraction
EDS	Energy Dispersive Spectroscopy
FIB	Focused Ion Beam
GSFE	Generalized Stacking Fault Energy
HIP	Hot Isostatic Pressing
IVAS	Integrated Visualization and Analysis Software
LEAP	Local Electrode Atom Probe
MD	Molecular Dynamics
mol.%	Molar Percent
NASA	National Aeronautics and Space Administration
NiTi	Nickel Titanium
NiTiAu	Nickel Titanium Gold
NiTiHf	Nickel Titanium Hafnium
NiTiPd	Nickel Titanium Palladium
NiTiPt	Nickel Titanium Platinum

NiTiZr	Nickel Titanium Zirconium
PED	Precession Electron Diffraction
SAED	Selected Area Electron Diffraction
SMA	Shape Memory Alloy
SEM	Scanning Electron Microscope
TEM	Transmission Electron Microscope
wt. %	Weight Percent
XRD	X-Ray Diffractometry

## ACKNOWLEDGEMENTS

I would like to take this opportunity to thank my colleagues, friends, and faculty members who have helped me with this research project. I would be remiss if I did not express my deepest thanks to Dr. Gregory B. Thompson, the chairman of this dissertation, for sharing his knowledge on microscopy and materials science. I would also like to thank him for giving me the chance to do research and work within his group and being a mentor during my time at the University. I am also appreciative of all the members of my committee, Dr. Amber Genau, Dr. Yuebin Guo, Dr. Ronald Noebe, and Dr. Mark Weaver for their input, additional guidance, and interest in this dissertation research. I would like to thank Ron Noebe and Glen Bigelow for providing the multiple samples used in this research and conducting the shape memory behavior testing reported in this dissertation.

The author would like to thank several former and current colleagues. Drs. Karen Henry, Monica Kapoor, Robb Morris, Tai Sasaki, Billie Wang, and Shawn Yu for excellent training on the multiple microscopes and endless discussions on research. Additionally, all my other current and former member of the Thompson's research group that provided so many memorable moments in graduate school. I would also like to thank Rich Martens and Johnny Goodwin and the rest of the staff of the Central Analytical Facility at the University of Alabama for many hours of training and assistance on the various tools.

## CONTENT

ABSTRACT	ii
DEDICATION	iv
LIST OF ABBREVIATIONS	v
ACKNOWLEDGEMENTS	vii
LIST OF TABLES	x
LIST OF FIGURES	xi
CHAPTER 1 INTRODUCTION	1
1.1 Motivation	1
1.2 Shape memory effect and phase responsible	3
1.3 Formation and crystal structures of secondary phases in NiTi	5
1.4 Influence of composition on transformation temperature	9
1.5 Ti-rich and equiatomic NiTiX ternary alloys and their properties	11
1.6 Ni-rich and equiatomic NiTiX ternary alloys and their properties	14
1.7 Increasingly Ni-rich binary alloys	17
1.8 Experimental Procedure	20
1.8.1 Materials Fabrication	20
1.8.2 Thermal and Mechanical Testing	21
1.8.3 Microstructural Characterization	22
1.9 Dissertation Organization	24

CHAPTER 2 STRUCTURE-PROPERTY RELATIONSHIP WITH H-PHASE PRECIPITATION IN A 50.3NI-29.7-20HF (AT.%) SHAPE MEMORY ALLOY	25
CHAPTER 3 MECHANISMS FOR THE ANOMALOUS RISE IN HARDNESS IN 55NITI (AT.%) 'BEARING' ALLOY	47
CHAPTER 4 HARDENING BEHAVIOR AND PHASE DE-COMPOSITION IN NI-RICH NITINOL ALLOYS	62
CHAPTER 5 CO-PRECIPITATION AND HARDENING BEHAVIOR IN LOW HF-SOLUTE ALLOYED NI-RICH NITINOL	83
CHAPTER 6 CONCLUSIONS AND FUTURE WORK	100
REFERENCES	104
APPENDIX	111
APPENDIX A: A PROCEDURE FOR ESTABLISHING ISOCONCENTRATION SURFACES FOR THE DETERMINATION OF PRECIPITATE COMPOSITION AND VISUALIZATION	112

## LIST OF TABLES

2.1	Martensite and austenite start and finish temperatures (from DSC) and hardness for the Ni-29.7Ti-20Hf alloy in the solution treated and aged conditions.	35
2.2	Length, width, and ratio of length versus width measured from the STEM-HAADF image for the Ni-29.7Ti-20Hf alloy in the 3, 30, and 300 hours aged conditions with the H-phase precipitates present.	37
A.1	The compositional values taken of the matrix and precipitate phase using the proxigrams in Figure A.3 for the 50.3Ni-29.7Ti-20Hf (at.%) alloy aged at 550°C for 3 hours. Note how the composition of the matrix and precipitate phase was altered by the choice of the isoconcentration value used for the Ni, Ti, and Hf species.	120
A.2	The compositional values taken of the matrix and precipitate phase using the proxigrams in Figure A.4 for the 50.3Ni-29.7Ti-20Hf (at.%) alloy aged at 550°C for 3 hours. Note how the composition of the matrix and precipitate phase was altered by the choice of the isoconcentration value used for the Ni, Ti, and Hf species.	121

## LIST OF FIGURES

1.1	Schematic depicting the change in strain as a function of stress and temperature as an alloy is heated and cooled through an entire transformation cycle taken from [14].	3
1.2	Three transformation paths generally seen in NiTi based alloys [15].	4
1.3	Ni-Ti phase diagram containing inset showing the phase field of metastable Ni <sub>4</sub> Ti <sub>3</sub> .	6
1.4	Time-Temperature-Transformation diagram of 52Ni-48Ti (at.%) alloy providing insight into the varying kinetic of the secondary phases in Ni-rich binary alloys from [41].	7
1.5	Temperature breakdown for the precipitation of the various secondary phases in Ni-rich binary alloys.	8
1.6	Plot of martensite start temperature as a function of atomic percent Ni from [2,34,41,46-52].	10
1.7	Plot indicating effect ternary addition of Au, Hf, Pd, Pt, and Zr have on the martensite start temperature for equiatomic compositions of NiTiX alloys from [66].	12
2.1	(a) Hardening curve for Ni-29.7Ti-20Hf aged at 550°C for various times.(b) DSC curves for the alloy in the solution annealed/quenched condition and after aging for 0.3 hour, 3 hours,30 hours, and 300 hours at 550°C.	31
2.2	Ni-29.7Ti-20Hf aged 0.3 hrs at 550°C: (a) Bright field image, (b) SAED from [001] <sub>B2</sub> ,(c)SAED from[1 $\bar{1}$ 0] <sub>B2</sub> , and (d) SAED from [1 $\bar{1}$ 1] <sub>B2</sub> . Ni-29.7Ti-20Hf aged 3 hrs at 550°C (e) HAADF-STEM image,(f) SAED from [001] <sub>B2</sub> (arrows indicate the H-phase reflections), (g) SAED from [1 $\bar{1}$ 0] <sub>B2</sub> (arrows indicate the H-phase reflections), and (h) SAED from [1 $\bar{1}$ 1] <sub>B2</sub> (arrows indicate the H-phase reflections).	33

2.3	(a) Ion map showing H-phase precipitates in the 3 hr aged Ni-29.7Ti-20Hf alloy delineated with a 22.3 at.% Hf isoconcentration surface. (b) Proximity histogram generated from a 27.7 at.% Ti surface with the dashed line marking the interface between the matrix and H-phase precipitates. (c) Plot of number density of H-phase precipitates as a function of aging time. (d) Plot of Ni/(Ti+Hf) concentration in the precipitate phase as a function of aging time.	38
2.4	Load-biased shape memory behavior of the Ni-29.7Ti-20Hf alloy: (a) solution annealed and quenched, and aged at 550°C for (b) 0.3 hours, (c) 3 hours, and (d) 30 hours. The red curves indicate heating cycles and the blue curves are the cooling cycles.	40
2.5	Comparison of load-biased shape memory properties for the Ni-29.7Ti-20Hf alloy in the solution treated and aged conditions: (a) transformation strain as a function of compressive (engineering) stress, (b) unrecovered strain as a function of compressive (engineering) stress, and (c) thermal hysteresis as a function of compressive (engineering) stress.	42
3.1	Aging curve for a 55NiTi (at.%) alloy at various processing treatments.	51
3.2	(a) Many-beam bright field image of the as-received microstructure of the 55NiTi. (b) SAED pattern from the [111] zone of the SA condition confirming the presence of Ni <sub>4</sub> Ti <sub>3</sub> precipitates, evident by the x/7 reflections along the <123> reciprocal vector of the B2 phase (highlighted by the arrows) (c) Two-beam bright-field micrograph showing strain contrast around the Ni <sub>4</sub> Ti <sub>3</sub> precipitates in the B2 NiTi matrix of the SA condition. (d) STEM-HAADF image of the SA microstructure revealing a high volume fraction of the Ni <sub>4</sub> Ti <sub>3</sub> precipitate phase (bright contrast) with very narrow B2 NiTi matrix channels (dark contrast) between the individual precipitates.	53
3.3	(a) SEM back-scattered image of a 55NiTi specimen aged at 750°C for 1 hour revealing coarse Ni <sub>3</sub> Ti <sub>2</sub> and Ni <sub>3</sub> Ti phases. (b) SEM back-scattered image of a 55NiTi specimen aged at 400°C for 336 hrs showing the initial decomposition of the B2 NiTi+Ni <sub>4</sub> Ti <sub>3</sub> to B2 NiTi + Ni <sub>3</sub> Ti phases.	54
3.4	MD simulations of the GSFE surfaces for (a) (011) NiTi plane and (b) (111) Ni <sub>4</sub> Ti <sub>3</sub> plane. The x-y axis for each figure represents the crystallographic direction on each surface plane with the increments being the fractional displacements along that particular direction. Note the surface energies are nearly double for Ni <sub>4</sub> Ti <sub>3</sub> as compared to NiTi for equivalent colors.	58

- 3.5 Phase identification: (a) SAED pattern taken from the labeled  $\text{Ni}_3\text{Ti}$  region in Figure 3.2(a) (b) SAED pattern taken from the [111] B2 NiTi zone axis from the labeled  $\text{Ni}_4\text{Ti}_3$  region in Figure 3.2(a). Additional diffraction spots confirms  $\text{Ni}_4\text{Ti}_3$  (white arrows) and R-phase (red arrows). (c) XRD of the SA 55NiTi specimen (d) XRD of 55NiTi sample aged at  $750^\circ\text{C}$  for 1 hour (e) XRD of 55NiTi sample aged at  $400^\circ\text{C}$  for 336 hours. Note, the XRD scans are from bulk specimens (not powder) indicating care in any interpretation of the XRD peak intensities. 60
- 4.1 (a)  $400^\circ\text{C}$  aging curves for various Ni-rich Ni-Ti compositions. (b) XRD scans and phase identification for the various Ni-rich Ni-Ti compositions in the solutionized/quenched condition. (c) Binary Ni-Ti phase diagram from [11]. 67
- 4.2 (a) BSE SEM micrograph of the 57NiTi solutionized/quenched microstructure revealing coarse  $\text{Ni}_3\text{Ti}$  and  $\text{Ni}_3\text{Ti}_2$  precipitates, indicated by the arrows, in a B2 matrix. The fine scale of  $\text{Ni}_4\text{Ti}_3$  precipitates at this magnification could not be observed. (b) BSE SEM micrograph of the 54NiTi solutionized/quenched microstructure where no obvious coarse precipitates were observed at this magnification.. 69
- 4.3 Multiple beam bright field image of the solution annealed condition for (a) 53NiTi, (b) 56NiTi, and (c) 58NiTi. Note the stark difference in strain contrast as Ni content is increased especially from 53NiTi to 56Ni. SAED patterns for the solution annealed condition for the 54NiTi sample from (d) the [111] zone axis of B2 matrix phase with squares highlighting the  $\text{Ni}_4\text{Ti}_3$  reflections and circles highlighting the R-phase, (e) the [011] zone axis of B2 matrix phase, and (f) the [001] zone axis of B2 matrix phase. 70
- 4.4 (a) BSE micrograph of 53NiTi specimen aged 300 hours at  $400^\circ\text{C}$  consisting of a B2 matrix phase and coarsened  $\text{Ni}_4\text{Ti}_3$  precipitates, (b) BSE micrograph of 56NiTi aged 300 hours at  $400^\circ\text{C}$ , and (c) BSE micrograph of 58NiTi specimen aged 300 hours at  $400^\circ\text{C}$ . In the latter two samples,  $\text{Ni}_3\text{Ti}_2$  (b) and  $\text{Ni}_3\text{Ti}$  (c) were observed in addition to  $\text{Ni}_4\text{Ti}_3$  and B2 matrix phases. 71
- 4.5 Aging curves for various Ni-rich Ni-Ti compositions aged at (a)  $625^\circ\text{C}$  and (b)  $750^\circ\text{C}$  for various times. 73

- 4.6 BSE micrographs of 53NiTi specimens aged 48 hours at (a) 625°C and corresponding (b) EBSD scan identifying phases present; BSE micrographs of 56NiTi specimens aged 48 hours at (c) 625°C and corresponding (d) EBSD scan identifying phases present; BSE micrographs of 58NiTi specimens aged 48 hours at (e) 625°C and corresponding (f) EBSD scan identifying phases present. BSE micrographs of 53NiTi specimens aged 48 hours at (g) 750°C and corresponding (h) EBSD scan identifying phases present; BSE micrographs of 56NiTi specimens aged 48 hours at (i) 750°C and corresponding (j) EBSD scan identifying phases present; BSE micrographs of 58NiTi specimens aged 48 hours at (k) 750°C and corresponding (l) EBSD scan identifying phases present. 74
- 4.7 HAADF-STEM image from a 55NiTi alloy to give prospective of Ni<sub>4</sub>Ti<sub>3</sub> spacing and narrow B2 NiTi channels between the precipitates. Ni<sub>4</sub>Ti<sub>3</sub> volume fraction was ~71% [5]. 76
- 4.8 Consecutive images of 57NiTi specimen aged 1000 hours at 400°C starting at (a) and finishing at (c) from serial sectioning procedure highlighting a Ni<sub>3</sub>Ti heterogeneously growing off of Ni<sub>4</sub>Ti<sub>3</sub> precipitates, which act as a reservoir for the extra Ni needed for the growth of the Ni-rich phase; (d) Reconstructed model of the Ni<sub>3</sub>Ti growing from a Ni<sub>4</sub>Ti<sub>3</sub> precipitate. 80
- 5.1 (a) 400°C aging curves for various Ni-rich binary and ternary Ni-Ti alloys; note the binary data is from [8, 17]. (b) Bright-field image and (c) STEM-HAADF image of the 54Ni-44Ti-2Hf solutionized/quenched microstructure. Note the significant strain contrast generated from the high volume fraction of Ni<sub>4</sub>Ti<sub>3</sub> precipitates in (b) and the nanoscale Ni<sub>4</sub>Ti<sub>3</sub> precipitates and narrow B2 matrix channels revealed in (c). 88
- 5.2 (a) Bright-field image and (b) SAED pattern from the <111> zone axis of the 55Ni-44Ti-1Hf solutionized/quenched condition confirming the presence of the B2 and Ni<sub>4</sub>Ti<sub>3</sub> phases. The Ni<sub>4</sub>Ti<sub>3</sub> reflections are denoted by the rectangular boxes in Figure 5.2(b). Again note the significant strain contrast generated from the high volume fraction of Ni<sub>4</sub>Ti<sub>3</sub> precipitates in Figure 5.2(a). 89
- 5.3 54Ni-45Ti-1Hf alloy aged at 400°C/24 hours: (a) Bright-field image, (b) STEM-HAADF image, (c) SAED taken //<111>, and (d) SAED taken //<001>. The presence of the B2, Ni<sub>4</sub>Ti<sub>3</sub> precipitates, and H-phase precipitates (denoted by arrows), were all confirmed. 91

- 5.4 56Ni-40Ti-4Hf alloy solutionized and quenched condition: (a) STEM-HAADF image; (b) SAED taken  $//\langle 111 \rangle$ ; (c) SAED taken  $//\langle 001 \rangle$ . The presence of the B2 and Ni<sub>4</sub>Ti<sub>3</sub> precipitates were confirmed. 56Ni-40Ti-4Hf aged at 400°C/300hrs: (d) STEM-HAADF image; Note the formation of H-phase filling the narrow channels of B2 between the as-quenched Ni<sub>4</sub>Ti<sub>3</sub> microstructure. (e) SAED taken  $//\langle 111 \rangle$ ; (f) SAED taken  $//\langle 001 \rangle$ ; and (g) Dark field image generated using the H-phase reflection circled with the black dotted line in (f). The presence of the B2, Ni<sub>4</sub>Ti<sub>3</sub> precipitates, and H-phase precipitates (denoted by arrows) were all confirmed. 93
- 5.5 54Ni-45Ti-1Hf alloy: Solutionized and quenched condition (a) Atom map of Hf showing no clear Hf partitioning, (b) Proximity histogram generated from a 52.48% Ni isoconcentration surface showing slight enrichment of Hf in the matrix, (c) SAED taken  $//\langle 111 \rangle$  confirming B2 and Ni<sub>4</sub>Ti<sub>3</sub> precipitates (denoted by rectangular boxes). 400°C/15 minutes aged condition: (d) Atom map of Hf showing no clear Hf partitioning, (e) Proximity histogram generated from a 52.25% Ni isoconcentration surface showing Hf homogenizing between the two phases, (f) SAED taken  $//\langle 111 \rangle$  confirming B2 and Ni<sub>4</sub>Ti<sub>3</sub> precipitates (denoted by rectangular boxes). 400°C/72 hours aging: (g) Atom map of Hf showing Hf partitioning to the Ni<sub>4</sub>Ti<sub>3</sub> phase with cylinder displayed used to create 1D concentration profile, (h) 1D concentration profile indicating Ni<sub>4</sub>Ti<sub>3</sub> phase is enriched in Hf and Ni compared to the matrix, (i) SAED taken  $//\langle 111 \rangle$  confirming B2, Ni<sub>4</sub>Ti<sub>3</sub> precipitates, and H-phase (denoted by arrows), but not observed in the limited volume of the APT analysis. 96
- A.1 (a) Fe atom map from a Co-Fe-Zr-Hf alloy showing clear Fe partitioning; (b) A 6 at.% isoconcentration surface for Fe; (c) Proxigram of the composition profile into and out of the defined isoconcentration surfaces. These images were adapted from those previously reported in reference [14]. 116
- A.2 (a) Atom map of 50.3Ni-29.7Ti-20Hf (at.%) aged 3 hours @ 550°C; (b) STEM-HAADF image of the same aged condition with Hf-enriched nanoscale precipitate present throughout the microstructure; (c) Selected area electron diffraction patterns from the [001], [1 $\bar{1}$ 0] and [1 $\bar{1}$ 1] zone axes of the B2 phase with additional reflections (indicated with the arrows) indexed to the H-phase precipitate. 118
- A.3 50.3Ni-29.7Ti-20Hf (at.%) aged at 550°C specimen for 3 hours: (a) 48.39 at. % Ni isoconcentration surface and its corresponding proximity histogram with its mid-point marked with a dashed circle; (b) 28.24at.% Ti isoconcentration surface and its corresponding proximity histogram with its mid-point marked with a dashed circle; (c) 18.71 at.% Hf isoconcentration surface and its corresponding proximity histogram with its mid-point marked with a dashed circle. 119

- A.4 50.3Ni-29.7Ti-20Hf (at.%) aged at 550°C for 3 hours: (a) 46.27 at.% Ni isoconcentration surface and its proximity histogram generated using the listed Ni composition from the precipitate phase in the original 48.39 at.% Ni surface (Table A.1); (b) 23.44 at.% Ti isoconcentration surface and its proximity histogram generated using the listed Ti composition from the precipitate phase in the original 28.24 at.% Ti surface (Table A.1); (c) 22.69 at.% Hf isoconcentration surface and its proximity histogram generated using the listed Hf composition from the precipitate phase in the original 18.71 at.% Hf surface (Table A.1). Note the shift for all. 120
- A.5 50.3Ni-29.7Ti-20Hf (at.%) aged at 550°C for 3 hours specimen: (a) Atom map with a precipitate isoconcentration surface displayed showing the cylinder used to generate the corresponding 1D profile; (b) Atom map with a precipitate isoconcentration surface displayed showing the cylinder, turned 90 degrees to generate a second orientation, used to generate the corresponding 1D profile. 123

# CHAPTER 1

## INTRODUCTION

### 1.1 Motivation

Since the initial discovery of the shape memory effect in the binary NiTi system in 1963, the implementation of these alloys in a vast number of engineering applications has been discussed. The most successful implementation of binary NiTi is in the medical field as cardiovascular stents and orthodontic wires [1]. These alloys are able to recover their original shape even against an opposing load when thermal cycled through their transformation cycle from the low temperature martensite phase to the high temperature austenite phase. This has led to great interest recently in utilizing the NiTi system as solid-state actuators for the aerospace industry. However, the low transformation temperatures and poor dimensional stability of the current alloy systems have to be overcome before application as actuators is possible.

With regard to actuator applications, there are two key factors that determine the practicality of an alloy: a transformation temperature  $\geq 100^\circ\text{C}$  and dimensional stability during cyclic loading. It has been well established that Ni-rich binary compositions have transformation temperatures intrinsically lower than Ti-rich compositions, and are well below room temperature [2]. However, recent work has shown that Ni-rich compositions macro-alloyed with Pt, Pd, Zr and Hf precipitate out secondary phases leading to increased transformation temperatures to  $\sim 100^\circ\text{C}$  satisfying the first key factor [3-6]. The second requirement is the dimensional stability of the alloy. Prior work on binary alloys confirmed Ni-rich compositions have superior dimensional

stability despite their lower transformation temperatures compared to Ti-rich compositions [7]. This fact also holds true for ternary alloys with Ni-rich alloys having tremendous dimension stability compared to their Ti-rich counterparts [8].

The motivation of the first part of the dissertation is to optimize the microstructure of a Ni-rich system macro-alloyed with Hf, 50.3Ni-29.7Ti-20Hf (at.%), through a series of heat treatments. The microstructure attained after each of these treatments is comprehensively characterized via Transmission Electron Microscopy (TEM) and Atom Probe Tomography (APT) to identify the precipitates' size, number density, and composition responsible for the increased transformation temperature and dimensional stability.

The second part of this dissertation is focused on characterizing more Ni-rich compositions than generally studied with three primary objectives. As stated previously, Ni-rich alloys have extremely low transformation making them impractical for shape-memory applications, yet Buehler *et al.* discovered a 55Ni-45Ti (at.%) alloy possessed high hardness, stably non-magnetic, and excellent corrosion resistance [9]- This property set makes this alloy particularly suitable for roll bearing applications, yet the microstructure responsible for this property set has never been fully investigated. The first objective of the second portion of the dissertation is to determine the primary strengthening mechanism within the 55NiTi alloy's microstructure (microstructural features) yielding this unique alloy's property set. Second, establish if there is a compositional regime in Ni-rich binary alloys, 53-58Ni (at.%), to which this unique set of properties is limited. Third, several Ni-rich ternary alloys with solute additions of Hf were studied to investigate whether Hf could be used to: (1) further increase the hardness of the alloys through solid solution strengthening, (2) affect the phase stability within the alloys, and (3) lower the solution annealing temperature seen in the Ni-rich binary alloys.

## 1.2 Shape memory effect and phases responsible

While Nitinol was not the first alloy system discovered which possessed the shape memory effect, this honor belongs to 52.5Au-47.5Cd (at.%) [10] and In-Tl [11,12], it has quickly become the most well recognized alloy system in regards to the shape memory effect since its discovery in 1959 by Buehler *et al* [13]. The word Nitinol is simply a derivative of the constituent elements, Ni and Ti, and the acronym of the laboratory that discovered the effect, Naval Ordnance Laboratory. Current applications for Nitinol are primarily in the medical fields as stents, staples, and orthodontic wires.

The shape memory effect refers to a material that is able to undergo a reversible crystal structure change when heated and cooled through a temperature, as seen in Figure 1.1.

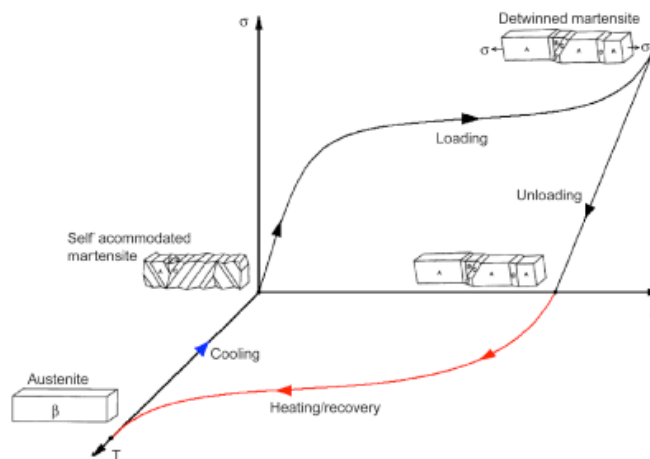


**Figure 1.1.** Schematic depicting the change in strain as a function of stress and temperature as an alloy is heated and cooled through an entire transformation cycle taken from [14].

During this process, any deformation undergone with the change in crystal structure is reversible which allows for the original shape to be recovered. The low temperature phase is known as martensite, and the high temperature phase is austenite. Martensite forms via a diffusionless transformation that occurs in solids, which is generally governed by a shearing-mechanism that allows for cooperative movement of atoms. As the temperature drops below the

martensitic transformation temperature, shear occurs generating twins in the austenite phase. In addition, the martensite can be further deformed by applying a load to the alloy too. There are several variants of martensite within the NiTi system. The austenite phase in NiTi is a B2 (ordered body centered cubic structure) crystal structure. The next section will briefly discuss the martensite variants and other secondary phases present in NiTi binary alloys. Understanding these phase is required before these alloys full potential can be reached regarding the shape memory effect.

These martensite variants each have their own unique crystal structures and parameters responsible for their formation. There are three variants of martensite in NiTi with two generally occurring as possible alternate pathways to the final form of martensite as seen schematically in Figure 1.2.

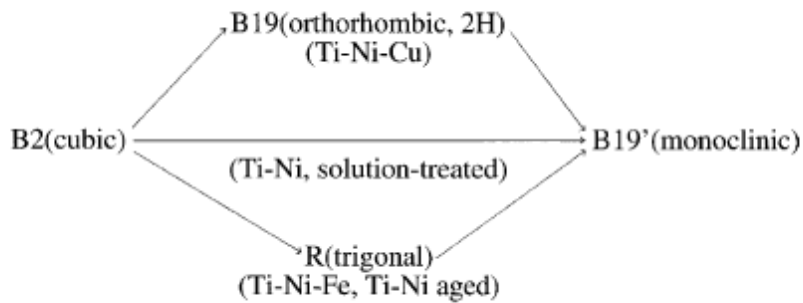


**Figure 1.2.** Three transformation paths generally seen in NiTi based alloys [15].

The final form of martensite most commonly seen is B19' with a monoclinic crystal structure [16,17] and a P21/m space group [18-20]. The transformation strain associated with B19' is the highest value of all the variants at (~10%). While this final form of B19' occurs in all NiTi based alloys, the B2 austenite phase can transform directly to B19' in solution treated binary NiTi alloys. There are two additional pathways leading to B19' and these pathways are

where the variants occur, B19 and R-phase. The B19 martensite has an orthorhombic crystal structure [21,22] with a  $Pmmb$  space group [23]. Its transformation strain is the second highest value of the variants at ~8%. This variant occurs as an alternative path to B19' in NiTiCu alloys [24] where the B2 austenite phase transforms to B19 then to B19'. Additionally, it has been identified to be the final form of martensite in ternary NiTiX (X = Au, Pt, Pd, Hf, and Zr) with macro-additions of the ternary element. The final variant and alternative pathway leading to B19' is referred to as the R-phase. The R-phase has a rhombohedral crystal structure [25,26] with a space still not completely settled upon but narrowed to being  $P3$  and  $P\bar{3}$  [27-33]. It has the lowest transformation strain value of the three variants at ~1%. This variant has been discovered to occur in three specific conditions [34]: (1) solute additions of Fe or Al are substituted for Ni in equi-atomic NiTi compositions; (2) Precipitation of the metastable  $Ni_4Ti_3$  by aging at appropriate temperatures for Ni-rich binary alloys; (3) cold working then heat treating to yield an altered dislocation structure in binary NiTi. For all these cases, the stress field of the solute additions, the  $Ni_4Ti_3$  precipitates, and altered dislocation structure effect the ability of R-phase and B19' to nucleate and thus their transformation temperature. Thus, the form or forms of martensite present in a NiTi based alloy depends on numerous factors, this holds true for other secondary phases within the system as will be seen shortly.

### **1.3 Formation and crystal structures of secondary phases in NiTi**

While the martensite and austenite phase are the two phases responsible for the shape memory effect, there are other secondary phases that play a crucial role in this effect. These secondary phases, i.e. precipitates, are known to influence the transformation temperature by a mechanical and chemical effect. The mechanical effects are a result of the stress fields generated around the precipitates. The stress field act as obstacles to the transformation requiring under-

cooling for it to occur [35,36]. Once the driving force of under-cooling reaches the required levels the transformation happens. Also, these stress fields can help to raise the transformation temperature if the stress field is sufficiently large and properly orientated allowing for martensite nucleation. The chemical effect is the precipitate absorbing Ni biasing the local matrix to be enriched in Ti [37] and alters the elastic constants. The enriched Ti local matrix and altered elastic constant will be further discussed shortly. The secondary phases that form in the binary NiTi system depend upon the bulk composition as seen in the Ni-Ti phase diagram, Figure 1.3.

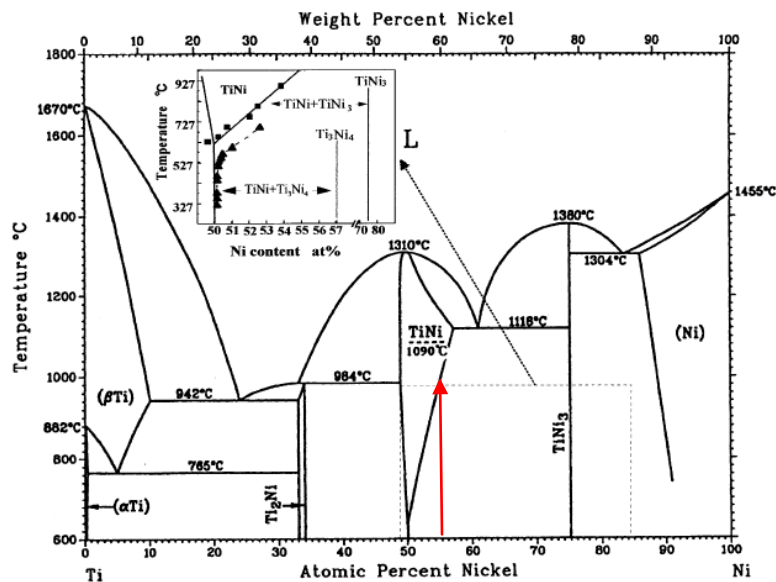


**Figure 1.3.** Ni-Ti phase diagram containing inset showing the phase field of metastable Ni<sub>4</sub>Ti<sub>3</sub> [38,39].

With regard to alloys possessing the shape memory behavior, the primary of interest for the phase diagram is the 50 atomic percent mark and extends above and below this mark by 5 atomic percent. At the 50 atomic percent mark, the phase boundary on the Ti side is nearly vertical making it impossible to get Ti-rich Ni-Ti solid solution. Moving to Ti-rich composition, leads to the formation of the cubic Ti<sub>2</sub>Ni phase with aFd3m space group [40].

Though the Ni side has more solubility, it drops drastically with temperature. This solubility behavior yields a range of secondary phases for Ni-rich compositions depending upon aging treatments as the Time-Temperature-Transformation (TTT) diagram (for a 52Ni-48Ti (at.%) alloy) illustrates, Figure 1.4.

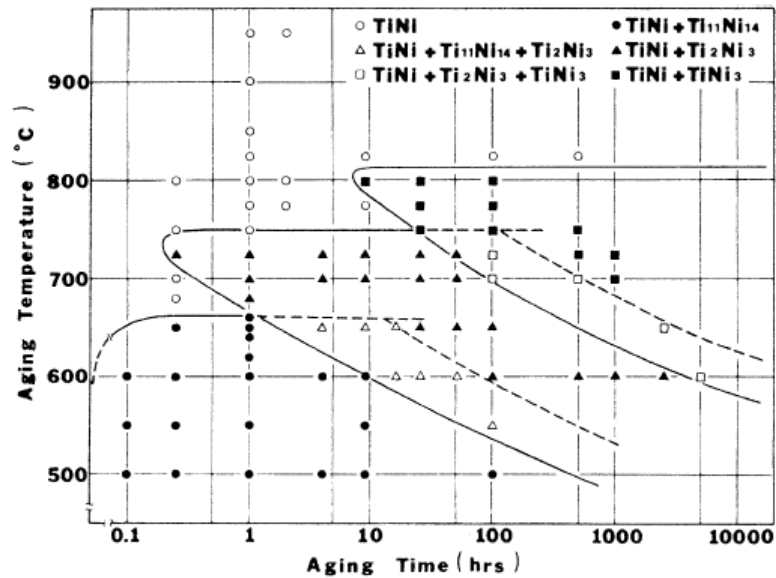


**Figure 1.4.** Time-Temperature-Transformation diagram of 52Ni-48Ti (at.%) alloy providing insight into the varying kinetic of the secondary phases in Ni-rich binary alloys from [41].

For Ni-rich composition, the NiTi phase with its B2 ordered structure becomes thermodynamically stable at temperatures above the solvus line. For a 55Ni-45Ti (at.%) alloy, the solvus temperature is  $\sim 950^{\circ}\text{C}$ , but decreases to  $\sim 700^{\circ}\text{C}$  for a 50Ni-50Ti (at.%) demonstrating the decreasing solubility with temperature. The B2 NiTi phase can be retained by quenching or slowly cooling to room temperature from the required solvus temperature for a given alloy's composition. The precipitation of the  $\text{Ni}_4\text{Ti}_3$  metastable phase takes place by aging below  $\sim 680^{\circ}\text{C}$  for a Ni-rich alloy consisting of the B2 NiTi phase. With extended aging at this temperature, the  $\text{Ni}_3\text{Ti}_2$  metastable phase will also form. The final secondary phase that would form with further aging is the equilibrium  $\text{Ni}_3\text{Ti}$  phase for Ni-rich alloys. Thus, the precipitation

sequence is  $\text{Ni}_4\text{Ti}_3 \gg \text{Ni}_3\text{Ti}_2 \gg \text{Ni}_3\text{Ti}$  for Ni-rich alloys. The schematic below, Figure 1.5, demonstrates with words how the precipitation sequence can be altered with increasing temperature for Ni-alloys (though it should be noted these temperatures are in reference to a 52Ni-48Ti (at.%) alloy).

Ni-rich NiTi alloy  
 Typical precipitation system.  
 $< 680^\circ \text{C}: \text{Ni}_4\text{Ti}_3 > \text{Ni}_3\text{Ti}_2 > \text{Ni}_3\text{Ti}$   
 $\sim 680\text{-}750^\circ \text{C}: \text{Ni}_3\text{Ti}_2 > \text{Ni}_3\text{Ti}$   
 $> 750^\circ \text{C}: \text{Ni}_3\text{Ti}$

**Figure 1.5.** Temperature breakdown for the precipitation of the various secondary phases in Ni-rich binary alloys.

The crystal structure and chemistry of  $\text{Ni}_4\text{Ti}_3$  metastable precipitate phase has been well-studied. When first observed, it was designated the X-phase. The proper crystal structure was determined to be rhombohedral with an R3 space group [42,43]. It has now become commonly identified using Selected Area Electron Diffraction (SAED) by extra reflections occurring at  $x/7$  positions, marked with arrows, along the  $\langle 123 \rangle$  reciprocal vectors of the B2 NiTi matrix phase looking down the  $[111]$  zone axis.

The metastable  $\text{Ni}_3\text{Ti}_2$  phase also required a great deal of research to confirm its crystal structure. It has now been established that  $\text{Ni}_3\text{Ti}_2$  has two crystal structures depending upon the temperature. The lower temperature crystal structure is orthorhombic with a Bbmm space group [44], whereas the higher temperature crystal structure is tetragonal with a I4/mmm space group [same as first part]. The equilibrium  $\text{Ni}_3\text{Ti}$  phase was found to have a hexagonal DO24 type ordered crystal structure [45]. With the numerous phases present in NiTi system identified and

their roles in the shape memory effect, the idea of this alloys implementation in a specific aerospace application of interest to this research will be touched upon.

While the discovery by Buehler *et al.* [13] of the shape memory effect in NiTi was significant, the truly groundbreaking finding was the ability of the alloy to recover its original crystal structure even when an opposing load is applied to it. This simply means the alloy is able to perform work, which leads to endless opportunities for industrial applications. One of the most promising applications is as solid-state actuators in aerospace applications. The NiTi alloy system will provide numerous advantages to the current actuator systems: lighter weight, more compact, high force (per volume/weight), quieter, frictionless, low maintenance, and eliminates extraneous systems. The two requirements for the successful implementation of a NiTi system in actuator systems are a martensitic transformation temperature  $>100^{\circ}\text{C}$  and good dimensional stability as the alloy undergoes thousands of transformation under a load during its service lifetime. Dimensional stability refers to the alloy's ability to maintain dimensional tolerances after undergoing numerous transformation cycles. The author has laid the microstructural foundation on which the NiTi shape memory field is based along with the promise it possess. Next, an in-depth review of the extensive research performed on the NiTi based system following its evolution to the current state is presented.

#### **1.4 Influence of composition on transformation temperature**

The early research focused on the transformation temperature of the varying alloys as a function of composition. The results from this research discovered that Ti-rich and equiatomic compositions have higher transformation temperatures than Ni-rich compositions as seen in Figure 1.6 [2,34,41,46-52].

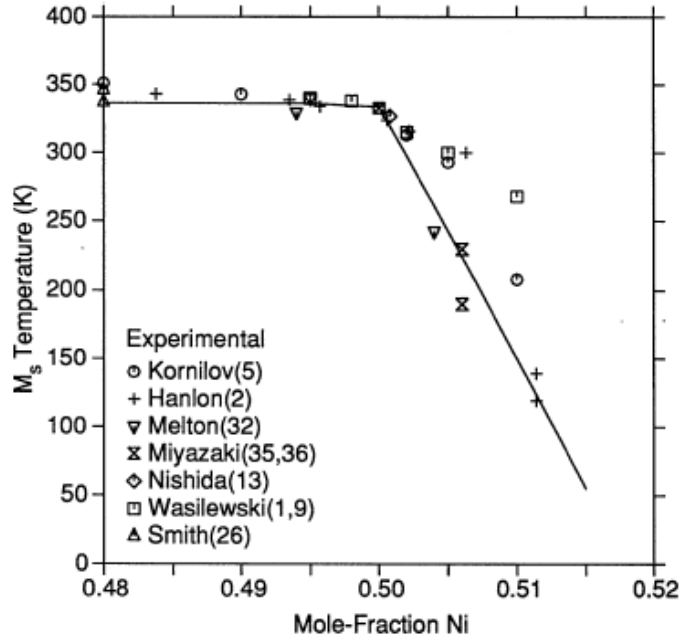


**Figure 1.6.** Plot of martensite start temperature as a function of atomic percent Ni [2,34,41,46-52]

These Ti-rich alloys have a constant transformation temperature of  $\sim 60^{\circ}\text{C}$  until reaching an equiatomic composition. The exact reason for Ti-rich compositions having higher transformation temperatures is still not completely understood. Some believe it is simply the lack of solubility on the Ti-rich side as seen with the nearly vertical solvus line in the phase diagram, Figure 1.3. This behavior makes it impossible to create a Ti-rich Ni-Ti solid solution. The other possible explanation is the softening of the elastic constant  $c'$  with lowering temperature [53]. In martensite alloys, this elastic constant is quite dependent on composition [54] since lattice dynamic properties can be significantly altered by alloying [15]. This means large changes in transformation temperature are required for small changes in composition which creates large changes in  $c'$  as  $c'$  is held constant at a transformation temperature. However, this hypothesis has only been validated for Ni-Ti-Cu; furthermore in the NiTi system both the  $c'$  and  $c_{44}$  elastic constants have vital roles in martensitic transformation [55].

While the Ti-rich binary alloys have intrinsically higher transformation temperatures than their Ni-rich counterparts, their maximum transformation temperatures ( $\sim 70^\circ\text{C}$ ) are still too low to allow for practical usage as actuator. Recall, the second key factor determining their possible usage as actuators is their dimensional stability. Research of the Ti-rich binary alloys has shown that their dimensional stability is poorer than that of Ni-rich binary alloys [7]. Furthermore, the mechanical performance of Ti-rich binary alloys degrades with increasing temperature [56,57]. Taking all the knowledge valuable to them at the time, researcher developed their next plan of act in researching this system. They turned to Ti-rich ternary alloys as the next alternative with the hopes of the ternary alloying would allow for secondary precipitation, beside  $\text{Ti}_2\text{Ni}$ , to improve the alloys' mechanical responses while still possessing the intrinsically higher transformation temperatures associated with Ti-rich alloys

### **1.5 Ti-rich and equiatomic NiTiX ternary alloys and their properties**

The elements used as ternary additions included Pd, Pt, Zr, Hf, and Au. Pd and Pt are believed to substitute for Ni due to similar electron configuration in their outer shell, while this same principle explains Hf and Zr substituting for Ti. Au is suspected to be substituting for Ni due to its electron configuration being more similar to Ni than Ti. However, Nakata et al. [58] found Au has no strong preference for a particular site but rather Au is strongly affected by the formula governing alloying element. As with any binary alloy system, the addition of a ternary element is generally going to alter the behavior of the system. This was noted for these ternary additions by the effect each had on the martensitic pathways and even varying amounts of the same ternary addition.

For NiTiAu alloys, Wu and Wayman established that B19' forms in  $\text{Ti}_{50}\text{Ni}_{50-x}\text{Au}_x$  alloys with  $x = 5$  and 10 at.% Au [59,60]; additionally, they confirmed the presence of B19 for even

more Au-rich compositions, where  $x = 40$  and  $50$  at.%. The compositional boundary that determines the type of martensite to form has not been fully established. For NiTiPd alloys with  $<10$  % (at.%) Pd, the martensitic transformation is a two-step transformation when cooling from B2 to B19' via R-phase [61]. Once the Pd content is increased to greater than 10%, the B19' martensite no longer occurs but rather B19 [61]. For NiTiPt with  $<10$  % (at.%) Pt, the martensitic transformation is single stage with cooling from B2 to B19'. In a similar fashion as seen in NiTiPd alloys, the B2 transforms to B19 with cooling with increasing content but the lower limit is 16% Pt [62]. For NiTiHf alloys, B19' transformation occurs until 20% Hf and at compositions greater than 20% B19 transforms from B2 [8,63]. For NiTiZr alloys, the same trend of B19' occurring with low Zr concentrations [62, 64], with debate over the limit being 15% or 20% Zr [65], and B19 occurring above that value.

The transformation temperatures for equiatomic and Ti-rich ternary alloys containing Pt, Pd, Au were found to increase with decreasing Ni content as seen in Figure 1.7 [66].

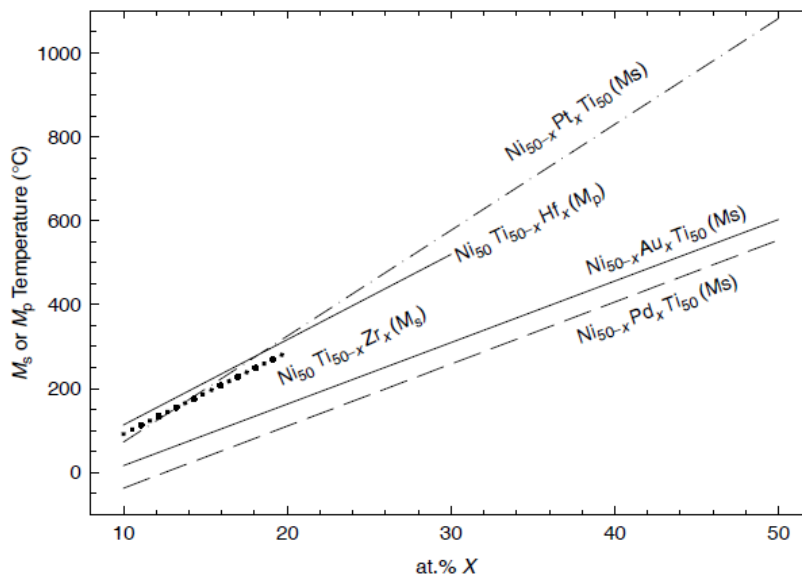


**Figure 1.7.** Plot indicating effect ternary addition of Au, Hf, Pd, Pt, and Zr have on the martensite start temperature for equiatomic compositions of NiTiX alloys [66].

However, all three precious metal containing systems require > 15% precious metal to increase the transformation above 100°C which continues to climb linearly with increasing content for all three. These increased transformation temperatures allowed the high cost associated with these ternary additions to be somewhat tolerated. While the transformation temperatures for these alloys has been researched extensively [1,59-61,67-71], the mechanical properties closely associated with shape memory applications have been reported in limited amounts.

Bigelow *et al.* [72] found for a series of Ti-rich, ternary  $\text{Ni}_{49.5-x}\text{Ti}_{50.5}\text{Pd}_x$  ( $x = 15, 20, 25, 30,$  and  $46$  at.%) alloys with increasing Pd content, a slight decrease in available work output and unrecoverable strain increased. A series of NiTiPt alloys were found to have narrow hysteresis during thermal cycling except for a 30 at.% Pt alloys reported by Lindquist and Wayman [1] and confirmed by several others [70,73]. This peculiar behavior as a function of composition is also continued with the load-bias behavior. A  $\text{Ni}_{30}\text{Ti}_{50}\text{Pt}_{20}$  alloy generated a maximum work output of  $8.7 \text{ J/cm}^3$  establishing it as a possible functional actuator material, while a  $\text{Ni}_{20}\text{Ti}_{50}\text{Pt}_{30}$  alloy was found to have little to no work output with its best measured work output being  $0.1 \text{ J/cm}^3$  [74]. With regard to Au, the cost of such large amounts have hindered any thorough investigation of Au-containing alloys' mechanical properties. As a result, lower cost alternative ternary additions of Hf and Zr were added to equiatomic and Ti-rich compositions.

These alloys, whether their initial composition is equiatomic or Ti-rich, see an increase in transformation temperature with increasing ternary additions as seen in the figure 1.7 above and Hsieh *et al.* [75]. It should be recalled that Hf and Zr substitute for Ti, thus Ni content is held at or below 50% since transformation temperature drop severely when going over this value

[76,77]. Even for these alloys, ternary addition > 10% are required to reach a transformation temperature >100°C required for actuator consideration, yet due to the lower cost these macro-additions are acceptable. The Hf containing alloys possess higher transformation temperatures with increasing Hf reaching a maximum of ~500°C at 30% Hf (at.%) than Zr containing alloy with a maximum transformation temperature of ~350°C reported by Hsieh *et al.* in a  $\text{Ti}_{26.5}\text{Ni}_{48.5}\text{Zr}_{25}$  alloy [75]. While these transformation temperatures are sufficient for high temperature actuator applications, multiple drawback were found to coincide with the increased transformation temperatures for these alloys: a decrease in the transformation temperature's thermal stability and recoverability, an increase in their thermal hysteresis, and poor dimensional stability during thermal cycling [75-80]. Furthermore, these alloy's microstructure could not be altered to address these issue since the only secondary phase possible in Ti-rich alloys are  $\text{Ti}_2\text{Ni}$  type phase, which provide no advantageous properties. As a consequence of these findings, the shape memory field again turned to equiatomic or Ni-rich composition, this time, with the ternary additions of Pd, Pt, Hf, and Zr.

## **1.6 Ni-rich and equiatomic NiTiX ternary alloys and their properties**

As a result of the good properties reported for a  $\text{Ni}_{30}\text{Ti}_{50}\text{Pt}_{20}$  [74,81], the microstructural features responsible for these promising property sets were investigated. While the alloy's composition is equiatomic, the alloy was found to precipitate out a secondary phase with aging. The secondary phase, termed P-phase, was identified as a monoclinic base-centered crystal structure with a C2/c space group and composition determined to be  $\text{Ni}_9\text{Ti}_{11}\text{Pt}_4$  [3]. A precipitate phase with the identical crystal structure was found to form in a Ni(Pd)-rich alloy,  $\text{Ni}_{27}\text{Ti}_{48}\text{Pd}_{25}$  [4]. The P-phase precipitates were found to help yield near perfect pseudoelastic behavior and superior dimension stability during load-bias thermal cycling of specified heat treated specimen

[4]. For both the NiTiPd and NiTiPt systems, the precipitates ensure the austenite phase is stronger than the martensite phase allowing them to exhibit good work output [66]. However, the precipitation of the P-phase is required before the transformation temperatures can be raised at all. Furthermore the transformation temperature and transformation strains cannot achieve the levels capable in Ti-rich ternary alloys. Despite the advantageous properties of these alloys, the high cost associated with Pd and Pt cannot be ignored, which has peaked interest in the cheaper alternative of Hf and Zr as ternary additions.

Ni-rich NiTiHf system first received attention when Meng *et al.* established that the transformation temperature could be raised to  $\sim 230^\circ\text{C}$  with aging for a  $\text{Ni}_{50.6}\text{Ti}_{29.4}\text{Hf}_{20}$  [82]. This aging resulted in the formation of nanoscale precipitate Meng *et al.* identified the precipitate by the extra reflection seen at  $x/7$  positions along the  $\langle 321 \rangle$  reciprocal vector of the B2 matrix phase looking down its [111] zone axis. These reflections matched those seen in Ni-rich binary NiTi for the metastable  $\text{Ni}_4\text{Ti}_3$  precipitates leading Meng to identify the precipitate as  $\text{Ni}_4(\text{Ti}+\text{Hf})_3$ . [82]. Bigelow *et al.* then performed the first known, preliminary shape memory testing on a  $\text{Ni}_{50.3}\text{Ti}_{29.7}\text{Hf}_{20}$  (at.%) alloy to determine the functionality of Ni-rich NiTiHf alloys as solid-state actuators [8]. Bigelow reported the alloy demonstrated a list of promising properties: high work output in tension and compression, tremendous dimensional stability at stresses up to at least 500 MPa, and near-perfect superelastic behavior at temperatures ranging from  $180\text{-}220^\circ\text{C}$  with  $>2\%$  transformation strain and full strain recovery upon unloading [8]. This is in stark contrast to Ti-rich versions of NiTiHf with their wide hysteresis, poor dimensional and thermal stability [83]. Bigelow also noted a fine dispersion of a secondary precipitate phase, different from the  $\text{Ni}_4(\text{Ti}+\text{Hf})_3$  observed by Ming and P-phases by Kovarik [3,82] in previous Ni-rich ternary alloys, contributing to the improved properties of the alloy. As

result of Bigelow's work, Yang *et al.* performed work on an identical  $\text{Ni}_{50.3}\text{Ti}_{29.7}\text{Hf}_{20}$  to determine the crystal structure of the precipitate Bigelow observed in his alloy [5]. Yang *et al.* determined the precipitate, referred to as the H-phase, to be slightly Ni-rich and have a face-centered orthorhombic lattice [5] matching the structure first identified by Han *et al.* [84] in an aged  $\text{Ni}_{48.5}\text{Ti}_{36.5}\text{Hf}_{15}$  alloy. This alloy system provides great promise as a candidate for solid-state actuator, yet the alloy requires further optimization of the microstructure through aging to generate the required properties for implementation.

The Ni-rich NiTiZr alloys have shown similar promising results as those noted in the Ni-rich NiTiHf alloys. The Zr additions provide a lower weight alternative to the NiTiHf system with a minimum of 20% weight reduction. Early work by Sandu *et al.* [85] established a nanoscale precipitate phase increasing strength in two alloys,  $\text{Ni}_{52}\text{Ti}_{42}\text{Zr}_6$  and  $\text{Ni}_{53}\text{Ti}_{41}\text{Zr}_6$  mol.%, that was later identified to be the H-phase. Recently, Evirgen *et al.* reported an aged  $\text{Ni}_{50.3}\text{Ti}_{29.7}\text{Hf}_{20}$  alloy to have excellent dimensional stability at stress levels up to 300 MPa [86], which is lower stress values than applied by Bigelow *et al.* [8] to their NiTiHf alloy . Furthermore, the Zr-containing alloy has a less vertical response during their load-bias thermal cycling than the Hf-containing alloys meaning a more gradual transformation occurring over a range of temperatures [8,86]. Thus, the Ni-rich NiTiHf and NiTiZr alloy systems have similar promising property sets with each having their own distinct advantages that would lead to their implementation when specific requirements must be achieved. This concludes the background for the evolution of NiTi based alloy for actuator applications. The remainder of the dissertation focus is on more Ni-rich compositions than typically investigated, which explains the diminished literature and background available for these alloys in the following sections.

## 1.7 Increasingly Ni-rich Binary Alloys

As previously mentioned, binary alloys with Ni content greater than 52 at.% have been shown to transformation temperatures  $< -100^{\circ}\text{C}$  [2]; thus, the implementation of these alloys in shape memory application is not practical. Fortunately, Buehler *et al.* [9] realized in his early work on a  $\text{Ni}_{55}\text{Ti}_{45}$  (at.%), converted to weight percent is  $\text{Ni}_{60}\text{Ti}_{40}$ , that despite its poor transformation temperature possessed other useful properties including high hardness, corrosion resistance (even in marine environments), stably non-magnetic, and lighter weight than most structural metals. With this property set, Buehler believed this alloy could be used in applications not possible with prior NiTi alloys such as hardened penetrators, (non -magnetic) hand tools, and bearing for water flooded rotating components [87]. However, the discovery of shape memory and superelastic behaviors in NiTi caused the research to largely disregard these more extremely Ni-rich alloys.

This unique properties set Buehler reported, while preliminary, contains many of the characteristics desired for roll bearing materials. During their lifetime are exposed to extreme condition where impact and corrosion resistance are required during their lifetime. The full array of properties required for bearing materials to handle such conditions is quite novel and still being investigated for a variety of materials as will be seen. The critical bearing's properties are the ones governing the material when it comes into contact with other parts within the system. The bearing material must have a sufficiently high hardness to prevent indent when contacting another machine part, but not be overly stiff that the stress is concentrated in a single spot leading to plastic deformation. The process of arriving at such a conclusion is not a recent achievement, but rather a long and continuous evolution in the research of bearing materials. In the late 19<sup>th</sup> century, Hertz developed one of the first analytical stress models relating a bearing

in contact with another material creating an interface [88]. Hertz's model was a generalized model that proved quite useful since it allowed for alterations to a number of terms including radii of curvature of the surfaces, their elastic moduli, and contact loads [89]. Using this model as a working guide, developments have led to the implementation of hard materials with equally high stiffness's and lower values of ductility and recoverable elastic strain, in comparison, for "hertzian" contact in industry applications [90]. This property combination yielded long lifetime and low friction at the cost of increased risk to local damage during high load events. This local damage is avoided by modifying contact geometry to reduce high stress levels and limiting overloads. The alternative approach to this situation is using softer, less rigid material in an attempt to reduce the local contact stresses, yet this creates another set of problems such as lower fatigue life, loss of load capacity, and higher operating frictions. Currently, the harder, more rigid materials are generally selected over the soft, less rigid materials for mechanical components. Thus, the ideal material for such application is one having adequately high hardness while simultaneously being compliant to reduce the peak stresses experienced during high-load events. However, this concept of a compliant material with a high hardness seems contradictory in nature since hardness and rigidity are considered complementary.

Developing a material with such a unique property set is not a new idea, T.L. Oberle first established in the 1950's that a ratio between a material's hardness (H) and elastic modulus (E), the H/E ratio, governs its wear resistance [91]. He referred to this ratio as the Modell ratio. With this ratio, Oberle made it clear a material possessing a high hardness with a low elastic modulus is the ideal candidate, but this property combination seems conflicting since high hardness and high elastic moduli are generally associated. Consequently, Oberle suggested a composite material with a hard chrome outer shell surrounding an inner substrate of steel. This composite

material idea has been further developed in the last decade with engineered coatings and surface treatments applied to materials to enhance their Modell ratio and overall tribological performance [92] Oberle developed the Modell ratio primarily focusing on sliding contacts, yet it has proven to be applicable for rolling contacts like bearings and gears as well. Despite this thorough understanding of the issue and solution, no material to date has been found to achieve a high Modell ratio so ceramic rolling elements and hybrid bearing are used even with their known issues.

With all this established knowledge, NASA began a study in the last decade to identify a material with high a Modell ratio making it an ideal bearing material. Their work concentrated on the Ni<sub>55</sub>Ti<sub>45</sub> (at.%) alloy Buehler initially reported as having potential in industry not possible for the lower Ni content versions of NiTi. DellaCorte *et al.* found the alloy to have a Rockwell C hardness (HRC) of 58 to 60 which is on par with a tool steel and is greater than the HRC of 55 generally established as the limit for a material as bearing and gear applications [93]. Furthermore, DellaCorte *et al.* found the alloy to exhibit a low effective modulus [93]. This property permits the alloy to undergo large strain without permanent deformation, meaning during shock loading contact points are less likely than current materials to undergo structural damage [93,94]. While these tremendous properties have led to the implementation of Ni<sub>55</sub>Ti<sub>45</sub> bearings in the water recycling system for the International Space Station [95], the microstructural features responsible for these properties have not been fully investigated. More recent work has begun to investigate more Ni-rich (>52 at.% Ni) binary alloy [96,97], yet these papers concentrated on higher temperature aging where the peak hardness is not fully optimized. Finally, the Ni<sub>55</sub>Ti<sub>45</sub> alloy is the gateway for future advance in the bearing materials research that will be further optimized through alloying of ternary alloys. The ternary addition will in theory

add strengthen through solid solution strengthening, and allow yield lower solution annealing temperature due to decreased Ni content to while maintaining the high hardness.

## **1.8 Experimental Procedure**

### **1.8.1 Materials Fabrication**

A multitude of alloys were analyzed using electron microscopy and atom probe tomography to correlate the microstructure to their mechanical response allowing for further engineering of the material in this dissertation. The varying alloys were fabricated one of three possible ways: heated extrusion, hot isostatic pressing (HIP), or arc melted. The particular method used for the fabrication of each alloy is described within the designated chapter of the dissertation examining said alloy. The materials were fabricated in collaboration with researchers from NASA Glenn (Ron Noebe and Glen Bigelow

The as-received specimens for all compositions were sectioned into smaller pieces for subsequent aging treatments. The initial step for all aging treatments of each alloy was solution annealing at 1050°C followed by water quenching. The alloys were then aged at various lengths of time and temperatures of 400°, 550°, 625°, and 750°C, which combination of time and temperature will be specifically designated within the dissertation. All solution annealing and subsequent aging treatments were performed in a tube furnace. During these treatments, the specimens were wrapped in Ta foil and a continuous flow of ultra high-purity Ar was used to reduce the possibility of oxidation. All specimens were immediately water quenched following all treatments. For treatments exceeding more than 24 hours, specimens were wrapped in Ta foil and encapsulated within quartz tubes that were backfilled with Ar. The tubes were broken and specimen water quenched once the heat treatment was completed.

## 1.8.2 Thermal and Mechanical Testing

Differential scanning calorimetry (DSC) was performed to examine the martensite to austenite phase transformation upon heating and the reverse order upon cooling. The transformation temperatures are determined by measuring the (exothermic and endothermic) heat flow during the phase transformations responsible for the shape memory effect. The measurements were performed using a TA Instrument DSC Q1000 with heating and cooling rates of 10°C/min.

All shape memory property related mechanical testing were conducted in collaboration with researchers (Ron Noebe and Glen Bigelow) from NASA GLENN. The procedures they utilized during the various tests will be briefly discussed here. Load-biased thermo-mechanical cycling tests in tension on an MTS 810 servo-hydraulic load frame using a MTS Flex Test SE digital controller. A CNC lathe was utilized in machining the tensile specimens into the cylindrical dog-bone shapes with 3.81 mm diameter by 16.4 mm long gage sections and threaded button ends. These tensile specimens were machined from the heat treated extrusion blanks. The specimens were held in threaded inserts at the end of hot grip extension rods gripped in water cooled hydraulic collets. A 100 kN/22 kip load cell was used to measure the load. Strain within the gauge section was measured with a high-temperature, water-cooled extensometer with a 12.7 mm gage length with a -10/+20% strain range, which used alumina extension rods via v-chisel tips held in contact with the sample surface by a frictionless knife-edge holding fixture.

Hardness testing was performed to observe the change in hardness as a function of aging time and temperatures for the various alloys. The measurements were taken using a Buehler Model 1600-6100 microhardness tester equipped with a Vickers diamond-pyramid indenter. A

load of 1 kilogram (kg) was applied to all alloys except the 50.3Ni-29.7Ti-20Hf which had a load of 500 grams (g) applied. Each specimen condition was indented 10 times with the mean hardness and standard deviation reported.

### **1.8.3 Microstructural Characterization**

A suite of advanced analysis techniques was utilized to study the effect of heat treatment on the microstructure. With regard to sample preparation for scanning electron microscopy (SEM), X-ray diffractometry (XRD), and dual beam SEM-focused ion beam microscopy specimen, the specimen were roughly polished with 800 grit SiC paper to remove any oxide layer present after the heat treatment. Once the oxide layer was removed, the specimen were polished using 9  $\mu\text{m}$  and 3 $\mu\text{m}$  diamond solution in consecutive steps before ending with a final step using 0.05 $\mu\text{m}$  colloidal Si on a Buehler AutoMet 250 Grinder Polisher. SEM secondary and back-scattered electron images were taken using a JEOL 7000F microscope. XRD was performed only to determine phase identification within bulk samples for various specimens. XRD was performed using a Bruker D8 Discover with General Area Diffraction System (GADDS) with a Co  $K_{\alpha}$  radiation source and a Phillips X'Pert MPD with a Cu  $K_{\alpha}$  radiation source.

Transmission electron microscopy (TEM) specimens were prepared by cutting a 3 mm disc from the heat-treated specimen of interest using a Fischione Model 170 ultrasonic disc cutter. The disc was then thinned down to a thickness of  $\sim 100\mu\text{m}$  using 1200 grit SiC paper followed by dimpling using 3 $\mu\text{m}$  diamond solution in a Fischione Model 200 Grinder to yield a final thickness  $< 10\mu\text{m}$  in the dimpled region. Once dimpled, the discs were ion milled using a Gatan Model 691 Precision Ion Polishing System (PIPS) until electron transparent perforations

formed in the dimpled region. Bright-field micrographs, selected-area electron diffraction patterns, energy dispersive x-ray spectrometry (EDS) line profiles, and scanning transmission electron microscopy-high angle annular dark field (STEM-HAADF) images were taken using a FEI Tecnai G<sup>2</sup> F-20 Supertwin (scanning) transmission electron microscope ((S)TEM) operated at 200 keV. STEM-HAADF image intensity is based on atomic number ( $\sim Z^2$ ) [98,99] rather than Bragg contrast as seen in a typical TEM image. Therefore, any difference in contrast between phases observed in the image provides insight to composition of the two phases with the brighter contrast phase containing higher atomic numbered atoms relative to the darker contrast phase.

Atom probe tomography (APT) specimen were lifted-out from the bulk sample and placed onto pre-fabricated Si posts using a FEI Quanta 200 3D Dual Beam scanning electron-focused ion beam microscope equipped with an Omniprobe micromanipulation lift-out system. Once attached to the Si post, the specimen were annular milled to yield the appropriate geometric needle shape with a radius of  $\sim 100$  nm required for field evaporation. The details of the FIB-based atom probe preparation can be found elsewhere [100,101]. Once the specimens were prepared, they were ran in a Cameca Local Electrode Atom Probe (LEAP) 3000XSi. All specimens were thermally assisted field evaporated using a laser mode at a pulse rate of 200 kHz. The specimens were held at a base temperature between 30-60K (-213 to -243°C) and ran using a pulse energy between 0.2-0.4nJ depending upon the evaporation field difference due to the varying composition levels of each constituent. The atom probe data was reconstructed using the software program IVAS 3.6 and above.

## 1.9 Dissertation Organization

The remainder of this work describes key findings of the microstructural analysis using electron microscopy of Ni-rich binary and ternary NiTiHf to their mechanical response. The dissertation is organized in a journal paper format, per the guidelines of The University of Alabama's Graduate School. Chapter 2 is a discussion on the microstructural optimization of a 50.3Ni-29.7Ti-20Hf alloy for solid state-actuator application. Multiple aged version of the alloy had their precipitates' size, number density, and chemistry correlated with their shape memory properties of the same condition. Chapter 3 is an investigation in the strengthening mechanism for a 55Ni-45Ti (at.%) alloy which is the first generation in a new class of bearing alloys based on more Ni-rich alloys than previously studied. Chapter 4 is a discussion on the compositional limits of the strengthening mechanism found in the 55Ni-45Ti alloy for a set of alloys from 53-58 at.% Ni. Additionally, the secondary phase stability in these Ni-rich alloys are investigated at multiple temperatures and times. Finally, Chapter 5 introduces a discussion on the second generation of the bearing alloys with solute additions of Hf in attempt to further improve on the alloy's property set. Chapter 6 is a summary of the research's results and ideas for direction of future work.

## CHAPTER 2

### STRUCTURE-PROPERTY RELATIONSHIP WITH H-PHASE PRECIPITATION IN A NI-29.7TI-20HF (AT.%) SHAPE MEMORY ALLOY<sup>1</sup>

#### **Abstract**

The martensitic transformation temperatures, load-biased thermomechanical properties, and microstructure (characterized by transmission electron microscopy and atom probe tomography) were investigated for a Ni-29.7Ti-20Hf (at.%) alloy aged at 550°C for 0 to 300 hours. Aging for three hours and longer resulted in the precipitation of a face-centered orthorhombic phase, previously denoted as the H-phase. The number density, size, and composition of this phase did not statistically change upon aging from 3 to 30 hours. Aging to 300 hours resulted in a decrease in the number density and significant coarsening of the precipitates at 550°C. The alloy exhibited near optimum response for shape memory behavior and dimensional stability after aging for three hours, though transformation temperatures continued to increase with aging time.

<sup>1</sup> A manuscript has been prepared for the work in this chapter for publication in Material Science and Engineering A.

## 2.1 Introduction

NiTi alloys, commonly referred to as Nitinol, exhibit a thermoelastic martensitic transformation and consequently are well-known for their shape memory and superelastic properties [1]. However, the transformation temperatures and thus the temperatures at which these various properties occur are highly dependent on composition. With regards to the shape memory effect, considerable interest has been in equiatomic and slightly Ti-rich Nitinol compositions because of their higher transformation temperatures as compared to Ni-rich compositions. Tang [2] has summarized the work of many groups that reported how minute increases in Ni-rich concentrations resulted in a precipitous drop in the transformation temperature to well below room temperature. Unlike the equiatomic and Ti-rich compositions, which generate significant residual strains during thermomechanical cycling through the transformation temperature [1,3,4], the Ni-rich compositions exhibit excellent dimensional stability during pseudoelastic stress cycling and load-biased thermal cycling because of precipitation strengthening effects [5-7]. Dimensional stability refers to the material maintaining a fixed dimensional tolerance during multiple transformation cycles, an attribute critical in actuator based applications. The ability to increase the transformation temperatures through ternary additions, while retaining the excellent dimensional stability observed in Ni-rich compositions, has been an active goal in shape memory alloy (SMA) research in recent years [8,9].

Several of the earlier efforts focused on the use of precious metal additions for increasing transformation temperatures in systems that were basically Ti-lean in stoichiometry. Kovarik *et al.* [10] reported the formation of a monoclinic precipitate phase, denoted as the P-phase, which had variant stacking options in a Ni-Ti-Pt alloy. Subsequent to this report, Sasaki *et al.* [11]

reported the same phase in a Ni-Ti-Pd SMA. In both systems, the precipitate was Ni-rich relative to the matrix and formed coherent/semi-coherent interfaces, which provided the necessary compositional alterations and strain that raised the transformation temperatures above 100°C [12]. Unfortunately, these types of precious metal additions are cost-prohibitive for developing alloys for wide-spread bulk applications.

A similar strategy has been used quite successfully to develop precipitate strengthened Ni-Ti-Hf [13,14,15] and Ni-Ti-Zr [16,17] high-temperature SMAs with good work output, stable large-strain pseudoelastic behavior at elevated temperatures, and nearly unprecedented dimensional stability during thermomechanical cycling. Relative to the precious metal additions, the Hf and Zr macro-additions provide a much lower cost alternative. As with the prior systems, the increase in the transformation temperatures, over solution treated conditions, was associated with the precipitation of nanoscale phases that affected the bulk composition and strain with the matrix. These precipitates, denoted as the H-phase, were confirmed as a face-centered orthorhombic structure in various Ni-rich compositions of Ni-Ti-Hf and Ni-Ti-Zr alloys [18,19], consistent with the phase that was first reported by Han *et al.* [20].

In this paper, we investigate the structure-property relationships in a Ni-29.7Ti-20Hf (at.%) alloy that undergoes H-phase precipitation. Using transmission electron microscopy (TEM) and atom probe tomography (APT), the precipitate structures formed at 550°C for various aging times were characterized and correlated to the transformation temperatures, the stability of the transformation temperatures with repeated thermal cycling, and the load-biased shape memory behavior of the alloy. This information provides necessary insights on the optimization of the H-phase precipitation with respect to shape memory properties of the alloy.

## 2.2 Experimental Procedure

An ingot of nominal composition Ni-29.7Ti-20Hf (at.%) was induction melted, homogenized at 1050°C for 72 hours in vacuum, and extruded at 900°C with an area reduction ratio of 7:1. The as-extruded bar was then sectioned, solution annealed at 1050°C for 3 hours and immediately water quenched followed by an aging treatment at 550°C for varying times up to 300 hours and also water quenched. All solution annealing and aging treatments were conducted in a tube furnace under a continuous flow of ultra-high purity Ar with the specimens wrapped in Ta foil to reduce oxidation of the specimens.

Hardness testing was conducted on a Buehler Model 1600-6100 microhardness tester equipped with a Vickers diamond-pyramid indenter using a load of 500 g. Each specimen was indented 10 times from which the mean hardness and standard deviation were determined and the values plotted as an age hardening curve.

Differential scanning calorimetry (DSC) was performed using a TA Instrument DSC Q1000 with heating and cooling rates of 10°C/min to determine the stress-free phase transformation temperatures. Austenite-start ( $A_s$ ) and austenite-finish ( $A_f$ ) temperatures on heating and the martensite-start ( $M_s$ ) and martensite-finish ( $M_f$ ) temperatures on cooling were determined by the baseline tangent method. At least four heating and cooling cycles were performed with the DSC instrument to determine the stability of the phase transformation temperatures for each condition.

The thermo-mechanical response of the alloy was determined using an MTS 810 servo-hydraulic load frame managed with an MTS FlexTest SE digital controller. Cylindrical samples, 5mm diameter by 10 mm in length, were compressed between Udimet-720 platens, which were backed by hot grip extension rods held by water-cooled MTS 646 hydraulic collet grips. Load was measured with a 100 kN load cell. Strain in the sample was measured with a high resolution

Micro-Epsilon OptoControl 2600 LED extensometer. Heating of the sample was performed using a Eurotherm temperature controller coupled with an Ameritherm Novastar 7.5 kW induction heater, which directly heated the hot grip extension rods. The platens and sample were then heated via thermal conduction through the hot grips. The specimen temperature was measured by a type-K thermocouple spot-welded directly to the middle of the specimen gage.

During the load-biased thermal cycling experiments, the “no load” condition in these tests corresponds to -1 to -3 MPa applied stress due to the applied force needed to maintain contact between the specimen and platens. This condition is labeled as “0 MPa” in the presentation of the data. Mechanical loading beyond the no load condition was controlled at a strain rate of  $1 \times 10^{-4} \text{ sec}^{-1}$  until the desired applied stress was reached at room temperature. The system was then switched to load-control followed by thermal cycling under a constant applied load. Specimens were tested at -50 MPa, and then in -100 MPa increments from -100 MPa to -700 MPa. At each stress level, temperature was cycled between 40°C and 300°C at a rate of 20°C /min or slower where the inherent convection of the material in room temperature air limited the temperature rate (i.e., upon cooling near ambient temperature). Two thermal cycles were carried out at each stress level; the second of these cycles is reported in the presentation of the data.

The microstructure after various aging conditions was characterized by TEM and APT. With regards to TEM specimen preparation, a 3 mm disc was cut from the heat-treated sample, ground to ~100  $\mu\text{m}$  in thickness using SiC papers, and then dimpled to a final thickness of < 15  $\mu\text{m}$  using a 6  $\mu\text{m}$  diamond suspension in a Fischione Model 200 Grinder. Once dimpled, the discs were then ion milled using a Gatan Model 691 Precision Ion Polishing System until electron transparent perforations formed in the dimpled region. The TEM analysis was

performed using a FEI Tecnai G<sup>2</sup> F-20 Supertwin (scanning) transmission electron microscope ((S)TEM) operated at 200 keV.

APT was performed using a Cameca Local Electrode Atom Probe (LEAP) 3000XSi. The atom probe specimens were lifted-out from the bulk sample and placed onto pre-fabricated Si posts using a FEI Quanta 200 3D Dual Beam scanning electron-focused ion beam microscope equipped with an Omniprobe micromanipulation lift-out system. Once attached to the Si post, the specimens were annular milled to yield the appropriate geometric needle shape with a radius of ~ 100 nm required for field evaporation. The details of the FIB-based atom probe preparation can be found elsewhere [21,22]. The specimens were maintained at a base temperature of 30K (-243°C) and thermally assisted field evaporated using a laser mode at a pulse rate of 200 kHz, pulse energy 0.2 nJ, and a target evaporation set at 0.5. The atom probe data was reconstructed using the IVAS 3.6.6 software package.

### **2.3 Results & Discussion**

Figure 2.1(a) shows the evolution of Vickers hardness as a function of aging time. The lowest hardness value of  $353 \pm 7.7$  VHN was recorded for the solution annealed condition and a slight increase to  $371 \pm 9.4$  VHN was noted after aging for 0.1 hour. The hardness peaked at  $492 \pm 7.7$  VHN after 100 hours aging and decreased to  $481 \pm 2.6$  VHN after 300 hours of aging.

Figure 2.1(b) shows the DSC curves containing four thermal cycles for each specimen for various heat-treated conditions. All the DSC curves show a set of endothermic peaks corresponding to the martensite-to-austenite transformation upon heating and exothermic peaks for the austenite-to-martensite transformation upon cooling. The start and finish temperatures of

the martensite and austenite phase transformations are listed in Table 2.1 for the second thermal cycle of each condition shown in Figure 2.1(b) (solution annealed, 0.3 hour, 3 hours, 30 hours and 300 hours) which are the focus of the remainder of this paper.

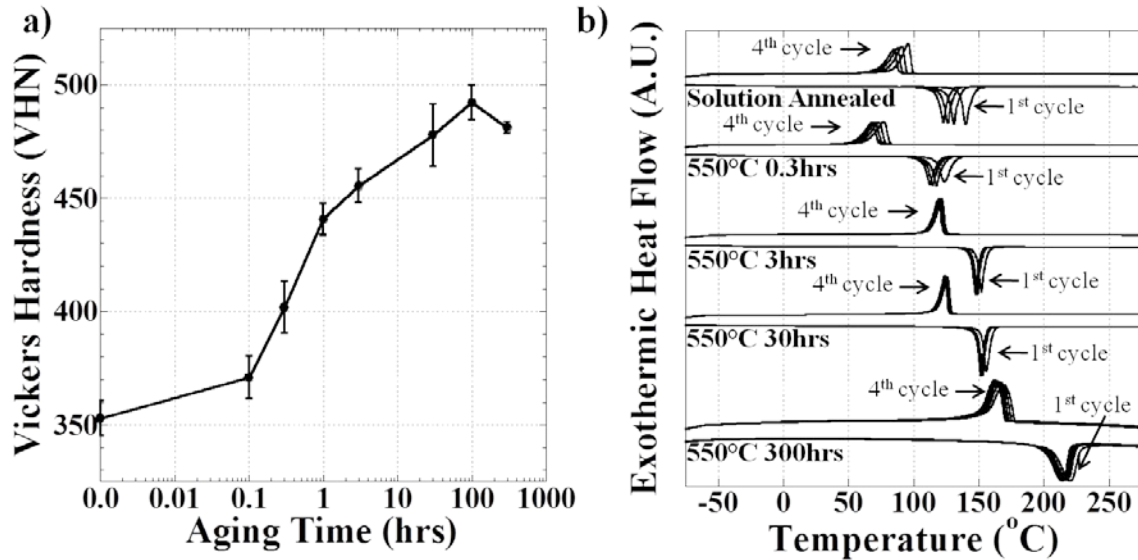


**Figure 2.1.** (a) Hardening curve for Ni-29.7Ti-20Hf aged at 550°C for various times.(b) DSC curves for the alloy in the solution annealed/quenched condition and after aging for 0.3 hour, 3 hours,30 hours, and 300 hours at 550°C.

Interestingly, the specimen with the 0.3 hour heat treatment exhibited a decrease in transformation temperatures compared to the solution annealed material. A similar decrease in transformation temperatures for early aging times and low aging temperatures has been observed in slightly Ni-rich NiTi alloys containing 15 and 20% Hf and Zr [23,24]. This decrease in transformation temperature is likely due to the dominance of one of the following two mechanisms, either a compositional effect or a mechanical effect. In terms of “composition,” in order for a decrease in transformation temperatures to occur, the overall matrix composition would need to become slightly enriched in Ni or depleted in Hf. “Mechanically,” it has been proposed that if there is such high a volume fraction of fine precipitates in the material that the inter-particle distance is actually less than the critical size for nucleation of martensite then

additional undercooling would be needed to reduce the critical nucleus size necessary to stabilize martensite formation [24]. To begin to determine the dominant mechanism in this case, it is necessary to look at the microstructure of the 0.3 hour aged material.

Figure 2.2(a) is the bright-field micrograph of the 0.3 hour aged specimen with its corresponding selected area diffraction (SAED) patterns, Figure 2.2(b-d), identifying the B2 austenite phase. In between the indexed B2 reflections, diffuse scattering is present that resembles the reflections of the H-phase seen in the 3 hour aged specimen, Figure 2.2(f-h). Similar diffuse scattering along with the distinct B2 reflections were noted in the solution annealed condition (not shown). In particular, the [001] zone axis in Figure 2.2(b) shows symmetrically similar arrangements to the H-phase reflections in Figure 2.2(f). However, viewing the  $[1\bar{1}1]$  zone, Figure 2.2(d), revealed a streaked appearance with the absence of the  $1/3$  reflections along the  $\langle 110 \rangle$  reciprocal vector of B2, which are clearly visible in the SAED pattern for the H-phase precipitate in Figure 2.2(h). The lack of consistent reflections between these zones, coupled with the diffuse intensity, lead to the conclusion that the solution annealed and 0.3 hour aged specimens are undergoing short range ordering [25] but not complete nucleation of the H-phase. The variation in discernible reflections between these zones suggests that the [001] is the preferential nucleation plane for the phase and is consistent with Han *et al.*'s determination of [001] being the habit plane in B2 [20]. Additionally, this plane (or direction) is the elastic soft direction for B2 [26]. X-ray diffraction for the 3 hour aged specimen indicated a B2 lattice parameter of 0.3088 nm, in agreement with Potapov *et al.* [27].

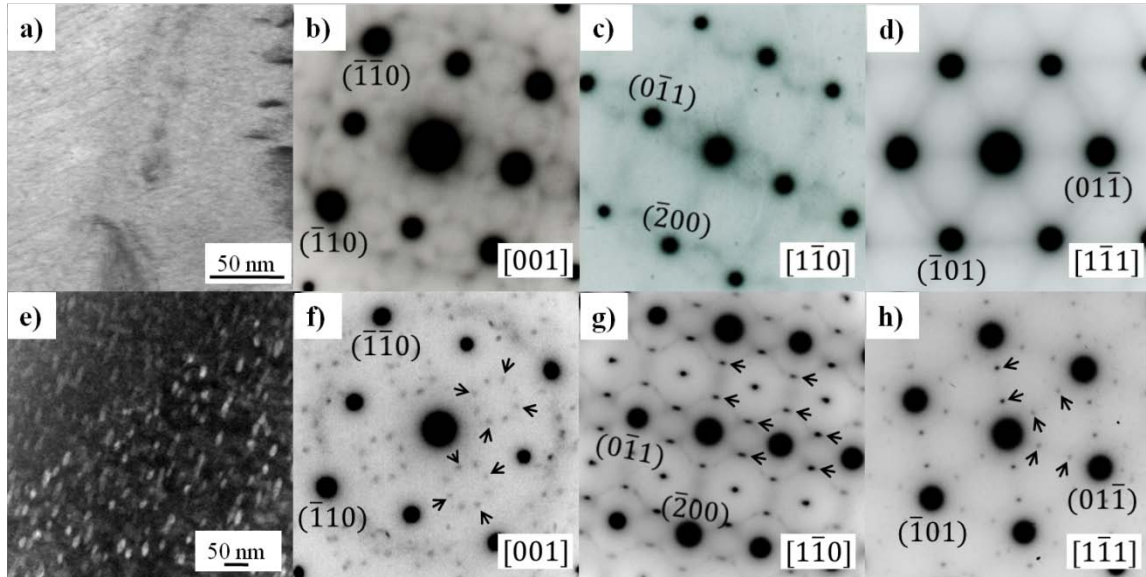


**Figure 2.2.** Ni-29.7Ti-20Hf aged 0.3 hrs at 550°C: (a) Bright field image, (b) SAED from  $[001]_{B2}$ , (c) SAED from  $[1\bar{1}0]_{B2}$ , and (d) SAED from  $[1\bar{1}1]_{B2}$ . Ni-29.7Ti-20Hf aged 3 hrs at 550°C (e) HAADF-STEM image, (f) SAED from  $[001]_{B2}$  (arrows indicate the H-phase reflections), (g) SAED from  $[1\bar{1}0]_{B2}$  (arrows indicate the H-phase reflections), and (h) SAED from  $[1\bar{1}1]_{B2}$  (arrows indicate the H-phase reflections).

Atom probe tomography analysis was performed to determine the presence of clustering within the solution annealed and 0.3 hour aged conditions to compliment the TEM diffraction evidence. Unfortunately, the high solute concentration (20 at.%Hf) prevented conclusive determination. Many of the APT clustering analysis techniques, such as the envelope method [28], are robust for cluster identification in low solute addition systems (< 10 at.%). With the large macro-alloy solute concentration in this alloy, the probability that the first, second, and so forth nearest neighbors being the solute atom is quite high, which makes statistically significant difference difficult if not impossible to discern. Still, the diffuse electron diffraction, Figure 2(b-d), and modest increase in hardness, Figure 1(a), provide experimental support for clustering behavior in the alloy.

Consequently, it is not clear which factor is dominating the decrease in transformation temperatures in this condition. It is possible that clustering could remove some Hf from the

matrix in turn making the matrix slightly richer in Ni and both of these effects would result in a slight decrease in transformation temperatures. However, this local change in composition could not be confirmed by either TEM or APT. It is also possible that the solute clusters, which do indeed increase the hardness of the material, would be very closely spaced and could affect the nucleation of martensite requiring additional undercooling to stabilize martensite formation. At this time, the exact mechanism for this common observation of initially decreasing transformation temperatures with early aging is still open for debate.

Aging for 3 hours and longer resulted in both an increase in the transformation temperatures and stabilization of the transformation temperatures with thermal cycling (Figure 2.1(b)) compared to the solution treated and 0.3 hr aged conditions. However, both the 3 and 30 hr aged samples had similar transformation temperatures including a martensite start temperature of approximately 133°C (Table 2.1). The conditions resulting in stable transformation temperatures also correlate with near peak hardness, Figure 2.1(a), indicating that precipitate formation both raises and stabilizes the transformation temperatures in the alloy. Figure 2.2(e) is a STEM-High Angle Annular Dark Field (HAADF) image of the 3 hour aged specimen, confirming the presence of nanometer sized H-phase precipitates. The HAADF image is sensitive to atomic-number contrast, with brighter contrast corresponding to phases with higher atomic number species. The white contrast of these nanoscale precipitates confirmed that the H-phase is enriched in Hf, compared to the matrix, consistent with the atom probe results, which are discussed below.

**Table 2.1.** Martensite and austenite start and finish temperatures (from DSC) and hardness for the Ni-29.7Ti-20Hf alloy in the solution treated and aged conditions.

Aging Time (hrs)	M <sub>f</sub> (°C)	M <sub>s</sub> (°C)	A <sub>f</sub> (°C)	A <sub>s</sub> (°C)	Hardness (VHN)
0 (Solution Annealed)	79.9	104.6	139.7	111.7	353 ± 8
0.3	60.7	89.2	128.6	98.8	402 ± 11
3	110.9	134.7	155.2	134.0	456 ± 7
30	115.7	133.1	158.7	139.6	478 ± 14
300	153.4	177.6	203.8	225.3	481 ± 3

The SAED patterns, corresponding to the STEM-HAADF microstructure in Figure 2.2(e), are given in Figure 2.2(f-h) for the three B2 matrix phase zone axes - [001], [ $1\bar{1}0$ ], and [ $1\bar{1}1$ ]. The arrows in each pattern indicated the reflections associated with the H-phase precipitate [18,20]. The 30 and 300 hour aged specimens also contained the same H-phase and B2 reflections in their SAED patterns (not shown). No other reflections (phases) were observed. Upon closer inspection of the H-phase precipitates in Figure 2.2(e), this phase forms an oblate spindle-like shape, which is consistent with its reported morphology in references [18,20].

The APT data presented in Figure 2.3 are for the clearly discernible H-phase precipitates observed during aging between 3 and 300 hours. Consistent with the TEM analysis, no distinct precipitates were observed in the solution treated or 0.3 hr aged sample. Figure 2.3(a) is an ion map revealing the H-phase precipitates in the 3 hr aged sample using a 22.3 at.% Hf isoconcentration surface. The size and shape of the precipitates is consistent with those seen in the STEM-HAADF image of Figure 2.2(e). The proximity histogram, based on a 27.7 at.% Ti isoconcentration surface for the 3 hour aged specimen is plotted in Figure 2.3(b). This surface is different than that used for the ion map image, Figure 2.2(e), because certain surfaces are more or less suitable for delineating the matrix-precipitate compositional profile or creating a visual image; the details of surface selection used for these alloys are found in reference [29]. The

compositional profile indicated that the precipitate phase was enriched in Hf and Ni and depleted in Ti as compared to the matrix. This would mean that the precipitation caused the bulk matrix composition to become leaner in both Ni and Hf. Hf depletion would cause a decrease in transformation temperatures, but Ni depletion results in a much greater increase transformation temperatures and appeared to dominate the overall transformation temperature effect [2,9]. Thus with increasing volume fraction of precipitate phase, transformation temperatures would increase [30, 31].

Upon aging, the number density of precipitates were statistically the same between 3 and 30 hours. Aging to 300 hrs resulted in an order of magnitude decrease in the number density of precipitates due to coarsening. This coarsening behavior was quantified by measuring the width and length of tens of precipitates via STEM-HAADF images for each aging conditions with precipitates and tabulated in Table 2.2. The APT determined volume fraction of H-phase was  $15.6 \pm 1.6$  (3 hour aged),  $14.8 \pm 1.5$  (30 hour aged), and  $22.2 \pm 2.2$  (300 hour aged). These results were consistent with values extracted from the STEM-HAADF images, similar to Figure 2.2(e), for each aged condition where the summed surface area of the precipitates were normalized to the total area of the HAADF image that contained the precipitates. The value for the 3 hr aged sample is also consistent with that determined previously by Coughlin for a similar Ni-29.7Ti-20Hf alloy [31]. With the increased volume fraction (i.e. decreased number density) coupled with the increased precipitate size, Table 2.2, for the 300 hours aged specimen would indicate that the precipitates coagulation and coalesced. This decreased number density was also noted in the drop in hardness as seen in the overaged portion of Figure 2.1(a).

**Table 2.2.** Length, width, and ratio of length versus width measured from the STEM-HAADF image for the Ni-29.7Ti-20Hf alloy in the 3, 30, and 300 hours aged conditions with the H-phase precipitates present.

Aging Time (hrs)	Length (nm)	Width (nm)	Ratio (L/W)
3	26.9 ± 4.0	11.5 ± 1.5	2.3 ± 0.4
30	27.1 ± 2.1	11.1 ± 2.3	2.4 ± 0.6
300	43.6 ± 11.3	17.4 ± 3.4	2.5 ± 0.8

Figure 2.3(d) is a plot of the Ni/(Ti+Hf) atomic compositional ratio of the H-phase from the APT data. The measured composition of the H-phase was 52.89 ± 0.018% Ni; 18.48 ± 0.032% Ti; 28.63 ± 0.028% Hf, taken from the 30 hours aged specimen. The composition ratio was statistically within the error of each aging treatment suggesting that the increase in transformation temperatures with increased aging time [30] is simply due to an increased volume fraction of precipitate phase and not necessarily due to a change in the precipitate-matrix composition with aging. This conclusion is also supported by the 3 and 30 hr aged conditions, which within the error of their compositional ratio, exhibited near equivalent volume fractions and nearly equivalent stress free transformation temperatures (Table 2.1).

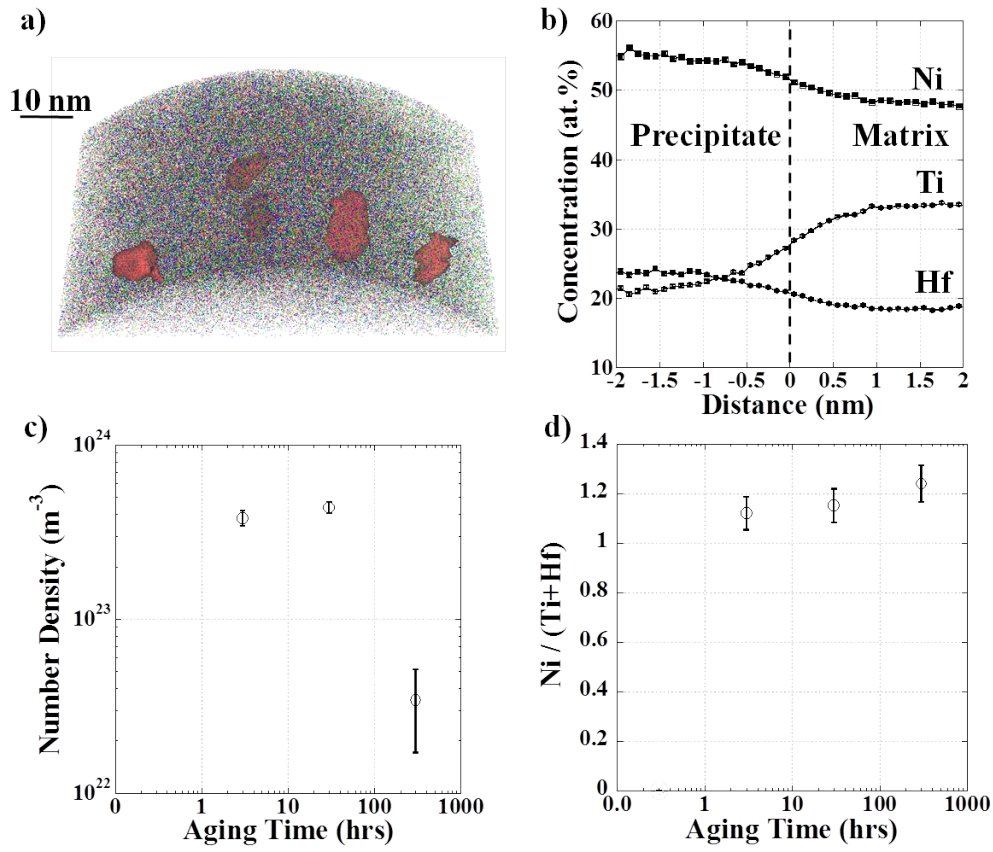


**Figure 2.3.** (a) Ion map showing H-phase precipitates in the 3 hr aged Ni-29.7Ti-20Hf alloy delineated with a 22.3 at.% Hf isoconcentration surface. (b) Proximity histogram generated from a 27.7 at.% Ti surface with the dashed line marking the interface between the matrix and H-phase precipitates. (c) Plot of number density of H-phase precipitates as a function of aging time. (d) Plot of Ni/(Ti+Hf) concentration in the precipitate phase as a function of aging time.

The compressive load-biased strain-temperature curves for the Ni-29.7Ti-20Hf alloy in four selected conditions are plotted in Figure 2.4 for constant stress levels from 0 to 700 MPa. In each material condition and stress level a notable change in true strain during thermal cycling was observed through the transformation regime. For actuator applications, a sharp transformation with narrow hysteresis is generally preferred in order to increase cycling rate. For the solution annealed specimen, the transformation region of the curve especially during heating shows a notable slope indicative of a shape memory response that requires significant temperature change to proceed (or sluggish propagation) and generally wide hysteresis compared

to the aged conditions. This is in agreement with the wider transformation hysteresis with thermal cycling observed in Figure 2.1(b) for the solution treated condition under stress-free conditions.

The 3 hour aged specimen, Figure 2.3(c), revealed a much more near vertical true strain response with transformation signifying a very rapid and easy propagation of the transformation front and a narrow hysteresis compared to the other conditions. Also the beginning and ending portion of the cooling and heating plots for the 3 hr aged sample lie almost completely on top of each other indicating exceptional stability with little or no unrecovered strains. The 30 hour aged sample showed a similar thermo-mechanical response at lower stresses consistent with the near equivalent number density of precipitates, Figure 2.3(d). However, at higher stress levels a decrease in dimensional stability compared to the 3 hours aged specimen was observed. Consequently, the longest aging condition (300 hours) was not conducted.

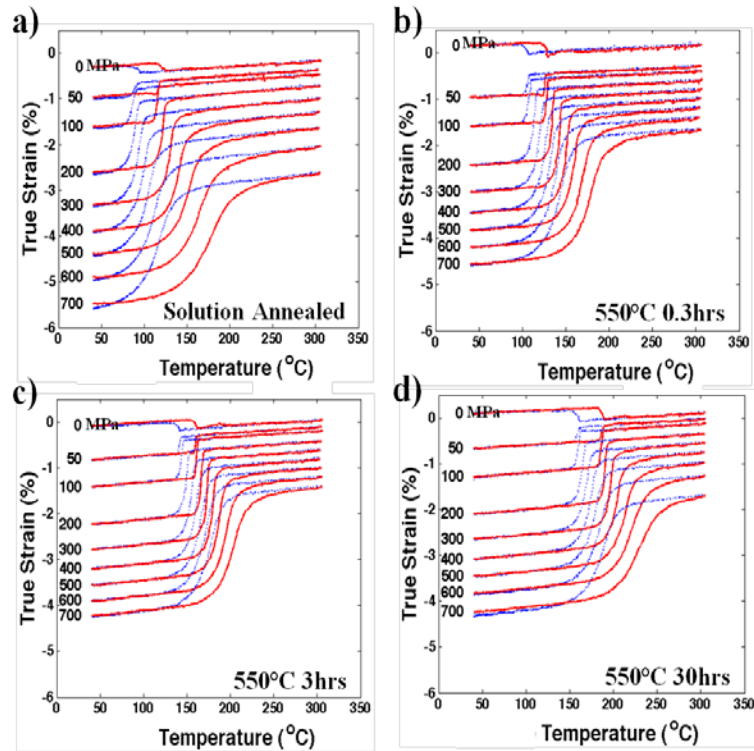


**Figure 2.4.** Load-biased shape memory behavior of the Ni-29.7Ti-20Hf alloy: (a) solution annealed and quenched, and aged at 550°C for (b) 0.3 hours, (c) 3 hours, and (d) 30 hours. The red curves indicate heating cycles and the blue curves are the cooling cycles.

A specific comparison of various shape memory properties as a function of aging condition is more clearly shown in Figure 2.5. Figure 2.5(a) is a plot of transformation strain in compression versus applied stress level. In all conditions, the transformation strain increased with increasing stress, though at higher stresses the rate of increase quickly decreased and the samples approached a maximum strain of approximately 2.0 - 2.5% by 700 MPa, consistent with [32]. At stress levels up to 200 MPa, the heat treatment does not seem to have a significant effect on transformation strain and the values are fairly similar. At the higher stress levels, the absolute differences in transformation strain are relatively small but are maximum for the solution annealed and the 0.3 hr aged samples (both precipitate free conditions) followed by the 3 and then 30 hr aged conditions. This is attributed to a higher volume fraction of precipitates and thus

a slightly smaller volume of transforming matrix phase. It is worth noting that the overall transformation strains are not large. It is worth noting that in polycrystalline NiTiHf alloys, depending on texture, can exhibit much larger transformation strains in tension and torsion, being a factor of 1.5 to 2.5 times greater than that in compression [33,13].

Figure 2.5(b) is a plot of unrecovered or residual strain measured in the martensite phase for the various heat treatment conditions as a function of stress providing a quantitative measure of dimensional stability. In general, the strain values are significantly lower, by an order of magnitude, compared to similar binary NiTi and high temperature SMAs like NiTiPd [34,35] demonstrating the excellent dimensional stability of the NiTiHf system. This intrinsic attribute is advantageous as the alloy would not necessitate subsequent ‘training’ (repeated cycling to stabilize) as required in other SMA alloys prior to use. Upon aging, with subsequent precipitation, an even lower residual strain than the solution treated condition was observed. The 550 °C/3hour condition exhibited the best stability particularly at the higher stresses, though these values are almost within the noise of the extensometer measurements and little difference in unrecovered strain was resolvable at lower stresses.

Finally, Figure 2.5(c) is a plot of the temperature hysteresis for the various conditions as a function of stress. Hysteresis is critical for thermal cycling considerations as it impacts the time it takes to drive through an entire heating and cooling cycle, which significantly affects cycle time. In this plot, the superior advantage of the 550 °C/3hour specimen is apparent compared to the other conditions. The hysteresis is relatively flat and between 15 and 20°C up to a stress levels of 500 MPa and does not surpass 30°C even at 700 MPa in this condition.

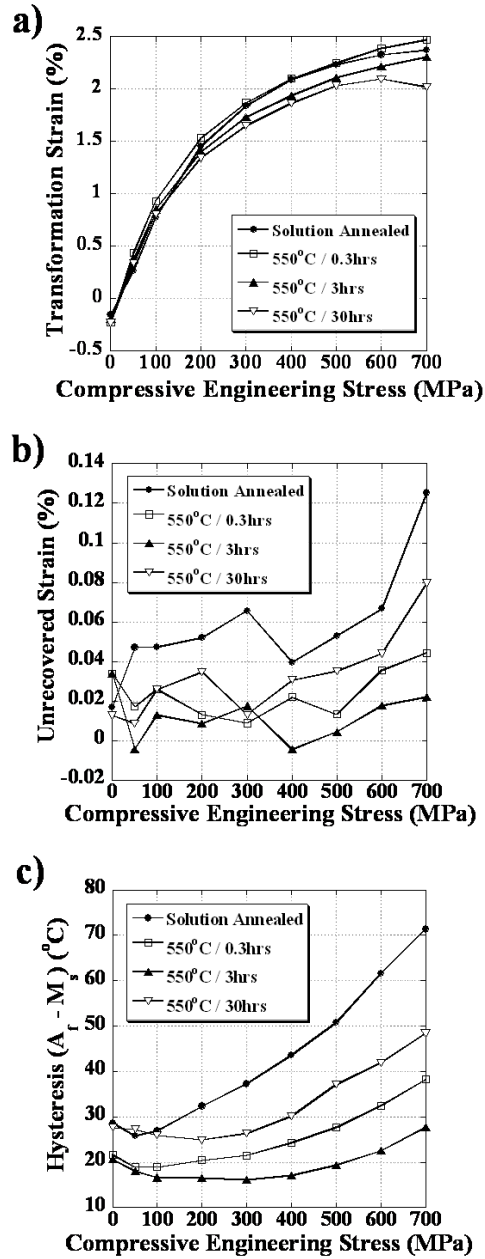


**Figure 2.5.** Comparison of load-biased shape memory properties for the Ni-29.7Ti-20Hf alloy in the solution treated and aged conditions: (a) transformation strain as a function of compressive (engineering) stress, (b) unrecovered strain as a function of compressive (engineering) stress, and (c) thermal hysteresis as a function of compressive (engineering) stress.

## 2.4 Conclusions

A Ni-29.7Ti-20Hf alloy was studied to determine transformation temperatures and load-biased thermomechanical behavior as a function of aging time at 550°C. The corresponding microstructures were characterized by TEM and APT. The alloy revealed diffuse scattering consistent with short-range ordering resembling the distinct reflections of the H-phase precipitate in the solution-annealed/quenched and 0.3 hour aged conditions. These reflections were most apparent in the [001] zone, suggesting it was the initial nucleating plane for this phase. Upon precipitation of the H-phase at 3 hours and longer, the transformation temperature increased and was stabilized for multiple thermal cycles. The precipitates also contributed to a near vertical transformation strain response for the 3 hours aged condition. In general, negligible strain accumulation was noted between cycles indicative of excellent dimensional stability, with the 550°C/3 hour condition optimal in terms of unrecovered strain and temperature hysteresis. Aging to 300 hours resulted in a drop in the number density of precipitates and a corresponding decrease in hardness, but a significant increase in transformation temperature. Since the precipitate composition (Ni/(Ti + Hf) ratio) was within the error of each other, the transformation temperature increase is believed to be more associated with fraction of precipitate than compositional changes.

Through this study, the heat treatment of a Ni-29.7Ti-20Hf alloy has been explored and the links between structure and properties determined. Though the primary focus is on actuator based applications, where maximizing transformation strain and minimizing unrecovered strain and temperature hysteresis is essential, the results also lend themselves to other needs. For example, if a wider hysteresis was required for a bonding or sealing application, then the solution treated condition would be preferable. Clearly, the ability to alter properties through heat

treatment is a significant advantage of this two phase NiTiHf alloy and provides ample microstructural engineering opportunities in the future.

## 2.5 References

- [1] K. Otsuka, X. Ren, *Prog. Mater. Sci.* 50 (2005) 511.
- [2] W. Tang, *Metall. Mater. Trans. A*, 28 (1997) 537.
- [3] C.H. Grossman, J. Frenzel, V. Sampath, T. Depka, and G. Eggler, *Metall. Mater. Trans. A* 40A (2009) 2530.
- [4] K.C. Atli, B.E. Franco, I. Karaman, D. Gaydosh, R.D. Noebe, *Mater. Sci. Eng.A* 574 (2013) 9.
- [5] K. Gall and H. Maier, *Acta Mater.* 50 (2002) 4643.
- [6] J.I. Kim and S. Miyazaki *Metall. Mater. Trans. A* 36A (2005) 3301.
- [7] J.I. Kim and S. Miyazaki *Acta.Mater.*53 (2005) 4545.
- [8] R.D. Noebe, T. Biles, S.A. Padula II, In: O. Winston, T.S.S. Soboyejo, editors. *Advanced structural materials: properties, design optimization, and applications*, vol. 7. Boca Raton, FL: CRC Press; 2007.
- [9] J. Ma, I. Karaman, R.D. Noebe. *Inter. Mater. Rev.* 55 (2010) 257.
- [10] L. Kovarik, F. Yang, A.Garg, D. Diercks, M. Kaufman, R.D. Noebe, *et al.* *Acta. Mater.* 58 (2010) 4660.
- [11] T.T. Sasaki, B.C. Hornbuckle, R.D. Noebe, G.S. Bigelow, M.L. Weaver, G.B Thompson, *Metall. Mater. Trans. A*, 44 (2013) 1388.
- [12] Y. Gao, N. Zhou, F. Yang, Y Cui, N. Hatcher, R. Noebe, M.J. Mills, and Y. Wang, *Acta Mater.* 60 (2012) 1514.
- [13] G.S. Bigelow, A. Garg, S.A. Padula II, D.J. Gaydosh, R.D. Noebe, *Scripta Mater.* 64 (2011) 725.
- [14] O. Benafan, R.D. Noebe, S.A. Padula, and R. Vaidyanathan, *Metal. & Mater. Trans. A*, 43 (2012) 4539.

- [15] O. Benafan, A. Garg, R.D. Noebe, G.S. Bigelow, S.A. Padula, D.J. Gaydos, N. Schell, J.H. Mabe, and R. Vaidyanathan, *Intermetallics* 50 (2014) 94.
- [16] A. Evirgen, I. Karaman, R.D. Noebe, R. Santamarta, J. Pons, *Scripta Mater.* 69(2013) 354.
- [17] A. Evirgen, I. Karaman, R. Santamarta, J. Pons, and R.D. Noebe, *Scripta Mater.* 81 (2014) 12.
- [18] F. Yang, D.R. Coughlin, P.J. Phillips, L. Yang, A. Devaraj, L. Kovarik, R.D. Noebe, M.J. Mills, *Acta Mater.* 61 (2013) 3335.
- [19] R. Santamarta, R. Arroyave, J. Pons, A. Evirgen, I. Karaman, H.E. Karaca, R.D. Noebe, *Acta Mater.* 61 (2013) 6191.
- [20] X.D. Han, R. Wang, Z. Zhang, D.Z. Yang, *Acta Mater.* 46 (1998) 273.
- [21] K. Thompson, D. Lawrence, D.J. Larson, J.D. Olson, T.F. Kelly, B. Gorman, *Ultramicroscopy* 107 (2007) 131.
- [22] L.A. Giannuzzi, *Microsc. Microanal.* 12 (2006) 1260.
- [23] A. Evirgen, I. Karaman, R.D. Noebe, J. Pons, and R. Santamarta, *Functional Mater. Lett.* 5 (2012) 1250038-1.
- [24] A. Evirgen, *Microstructural Characterization and Shape Memory Response of Ni-rich NiTiHf and NiTiZr High temperature Shape Memory Alloys*, Ph.D. Dissertation, Texas A&M University, August 2014.
- [25] D.B. Williams, C.B. Carter, *Transmission Electron Microscopy Part 2: Diffraction*, Springer Science + Business Media, 2009: p. 277.
- [26] X. Re, N. Miura, J. Zhang, K. Otsuka, K. Tanaka, M. Koiwa, *et al.* *Mater. Sci. Eng. A* 312 (2001) 196.
- [27] P.L. Potapov, A.V. Shelyakov, A.A. Gulyaev, E.L. Svistunova, N.M. Matveeva, D. Hodgson, *Mater. Lett.* 32 (1997) 247.
- [28] J.M. Hyde, C.A English, *MRS 2000 Fall Meeting*, 650 (2000) R6.6.1-R6.612.
- [29] B.C. Hornbuckle, G.B. Thompson, In preparation for submission to *Ultramicroscopy*. (Appendix A in dissertation).
- [30] H.E. Karaca, S.M. Saghaian, G. Ded, H. Tobe, B. Basaran, H.J. Maier, R.D. Noebe, Y.I. Chumlyakov, *Acta Mater.* 61 (2013) 7422.

- [31] D. Coughlin, Characterization of Stoichiometric and Aging Effects on NiTiHf High temperature Shape Memory Alloys, Ph.D. dissertation, The Ohio State University, 2013.
- [32] O. Benafan, A. Garg, R.D. Noebe, G.S. Bigelow, S.A. Padula II, D.J. Gaydos, N. Schell, J.H. Mabe, and R. Vaidyanathan, *Intermetallics* 50 (2014) 94.
- [33] A.P. Stebner, G.S. Bigelow, J. Yang, D.P. Shukla, S.M. Saghaian, R. Rogers, A. Garg, H.E. Karaca, Y. Chumlyakov, K. Bhattacharya, and R.D. Noebe, *ActaMater.* 76 (2014) 40.
- [34] O. Benafan, R.D. Noebe, S.A. Padula II, D.W. Brown, S. Vogel, and R. Vaidyanathan, *International Journal of Plasticity*, 56 (2014) 99.
- [35] G.S. Bigelow, S.A Padula, A. Garg, and R.D. Noebe, *Metall. Mater. Trans. A* 41 (2010) 3065.

## CHAPTER 3

### MECHANISMS FOR THE ANOMALOUS RISE IN HARDNESS IN A 55NiTi (AT.%) 'BEARING' ALLOY<sup>2</sup>

#### **Abstract**

A 55Ni-45Ti (at.%) bearing alloy was solutionized at 1050°C for 10 hours and water quenched. The hardness was  $644 \pm 5.1$  VHN, which compares to typical tool steels, and retained this high hardness after aging at 400°C for at least 100 hours. Transmission electron microscopy revealed that the strengthening was attributed to narrow B2 NiTi channels encasing nanoscale Ni<sub>4</sub>Ti<sub>3</sub> precipitates. Generalized stacking fault energies were determined for each phase by molecular dynamics confirming the difficulty to slip, contributing to the microstructural-driven high hardness.

<sup>2</sup> A manuscript has been prepared for the work in this chapter for publication in Scripta Materialia.

### 3.1 Introduction

NiTi and its variety of off-stoichiometric compositions, commonly referred to as Nitinol alloys, are well known for their ability to exhibit shape memory and superelastic behaviors [1]. The equiatomic NiTi and Ti-rich Nitinol alloys have received significant attention for actuator applications because of their higher transformation temperatures and large recoverable strains, while slightly Ni-rich compositions are primarily utilized for their superelastic behavior [1,2]. Of the Ni-rich alloys, compositions containing 50.7 to 52 at% Ni have been optimized for biomedical shape memory applications such as stents, staples, vascular filters, and orthodontic arch wires [2]. The exploration into even higher Ni-rich compositions has been largely ignored because the transformation temperatures readily drop well below room temperature with increasing Ni-content. Consequently, increasingly Ni-rich Nitinol alloys are impractical for many shape memory and superelastic designs.

Deviations from equiatomic NiTi stoichiometry result in the precipitation of a variety of intermetallic phases [3]. For example, the  $Ti_2Ni$  phase is observed in Ti-rich compositions whereas  $Ni_3Ti$ ,  $Ni_3Ti_2$ , and  $Ni_4Ti_3$  phases form on the Ni-rich side of stoichiometry depending on the heat treatment and cooling conditions [4]. These latter phases, in particular  $Ni_4Ti_3$ , have been shown to help stabilize the shape memory and superelastic behaviors [5]. As with other precipitation hardened alloys, optimized strengthening in these near stoichiometric compositions [5] is only achieved over particular aging times and temperature conditions. This is of particular concern for Ni-rich alloys, as  $Ni_4Ti_3$  and  $Ni_3Ti_2$  are metastable and decompose to  $Ni_3Ti$  [4].

Early on in the investigation of Nitinol alloys, Buehler *et al.* [6] noted that Ni contents on the order of 55 at.% (60 wt.%) exhibited unique sets of properties, which included high hardness, stably non-magnetic, lighter weight than most structural metals, and corrosion resistance even in

marine environments. Subsequently Buehler proposed the use of such alloys in non-magnetic hand tools, hardened penetrators, and bearings for water flooded rotating components [7]. Arguably, much of this work was over shadowed by the discovery of shape memory and superelastic behaviors in NiTi alloys.

Recently, interest in 55Ni-45Ti (at.%) as a bearing alloy has resurfaced with the realization that the material can be lubricated, unlike Ti alloys [8]. This property coupled with the exceptionally high hardness and its very low modulus allows it to undergo very large strains without permanent deformation. These latter traits reduce the chance for structural damage at contact points during shock loading [8,9]. Hence, the combination of these properties with those previously mentioned makes very Ni-rich Nitinol alloys promising candidates for bearings and other mechanical components. In fact the imminent use of this very Ni-rich Nitinol composition is as a bearing in the water recycling system for the International Space Station [10].

The hardening mechanisms resulting in such high strength [9] and the reported peculiar lack of conventional age hardening behavior [11] has not been fully understood in these alloys. Without such knowledge, systematic advancements will be dependent on chance trial and error discoveries. In this paper, the microstructure of a 55NiTi (at.%) alloy is characterized, and coupled to molecular dynamics simulations of generalized stacking fault energies (GSFE) for crystallographic slip, to elucidate the hardening behavior.

### **3.2 Experimental Procedure**

The Ni-rich 55NiTi (at.%) alloy was acquired from ATI Wah Chang, Portland, Oregon. In former reports [6-10] this material is referred to as 60NiTi or 60Nitinol, which is in reference

to its weight percent. The as-received condition of the material was a hot-rolled plate that had been heated to  $\sim 980^{\circ}\text{C}$  for 150 minutes then oil quenched. The as-received material was sectioned into smaller specimens and solution-annealed (SA) at  $1050^{\circ}\text{C}$  for 10 hours, placing it in the B2 phase field [3]. At the conclusion of SA, the specimens were water quenched and subsequently aged at  $400^{\circ}\text{C}$  for a variety of times. The SA grain size was  $\sim 110$  microns. One SA specimen was aged at  $750^{\circ}\text{C}$  for 1 hour to determine the temperature stability of the hardening mechanism. For all SA and aging processes, the specimens were placed in a tube furnace under a continuous flow of ultra-high purity Ar.

The alloy's phases and microstructure were characterized by transmission electron microscopy (TEM), scanning electron microscopy (SEM), and X-ray diffraction (XRD) and prepared in manners previously reported in [12]. Hardness testing was done on a Buehler Model 1600-6100 microhardness tester equipped with a Vickers indenter using a 1 kg load. Each specimen was indented 10 times with the mean hardness and standard deviation reported.

### **3.3 Results and Discussion**

The hardness of the 55NiTi alloy is plotted as a function of aging time in Figure 3.1. In as-received (hot-rolled) condition, the alloy's hardness was  $386 \pm 6.1$  VHN whereupon SA the hardness increased to  $644 \pm 5.1$  VHN, a 66% rise in hardness. This value is equivalent to a Rockwell hardness of 57-58 HRC, which is a typical value for fully hardened 440C tool steels [9]. Upon aging at  $400^{\circ}\text{C}$ , the hardness of the 55NiTi alloy was unaffected and remained relatively constant up to 100 hours aging with a slight decrease in hardness noted after 336 hours, Figure 3.1. Interestingly, the material did not exhibit a characteristic parabolic hardening

curve with aging time which is generally associated with a precipitation hardened alloy. When an equivalent SA specimen was aged at 750°C for 1 hour, a dramatic decrease in hardness to  $388 \pm 4.0$  VHN was noted; this value is similar to the as-received sample. Clearly, a processing dependent behavior is present for optimizing this alloy's hardness.

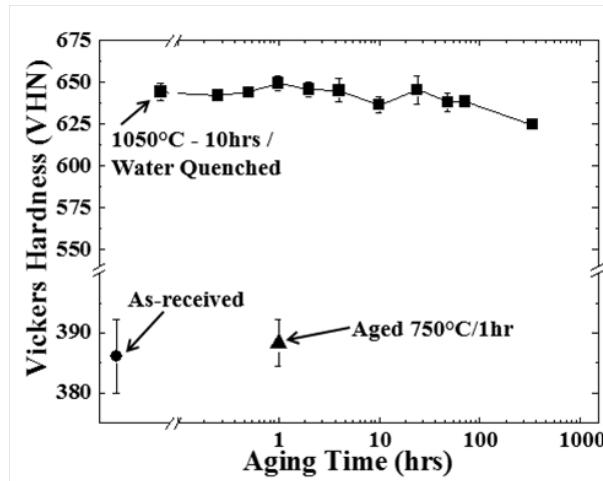


**Figure 3.1.** Aging curve for a 55NiTi (at.%) alloy at various processing treatments.

The TEM bright-field image of the as-received 55NiTi, Figure 3.2(a), shows a B2 NiTi matrix with precipitates of  $Ni_4Ti_3$ ,  $Ni_3Ti$ , and R-phase (a martensitic phase in Nitinol). The selected area electron diffraction (SAED) patterns that confirm each phase is found in the appendix figure available on-line. The SAED pattern from the SA 55NiTi alloy, Figure 3.2(b), was indexed only to B2 NiTi phase (matrix) and  $Ni_4Ti_3$  phase (precipitate). The  $Ni_4Ti_3$  precipitate reflections appear at  $x/7$  positions along  $\langle 123 \rangle$  reciprocal vectors of the B2 phase, confirming its rhombohedral structure and orientation relationship discussed [13]. Since metastable  $Ni_4Ti_3$  decomposes to  $Ni_3Ti_2$  and/or  $Ni_3Ti$  with increasing temperatures above 700°C [4], the absence of these other Ni-rich phases indicates that the alloy was solutionized in the B2 phase field. Though this alloy was quickly removed from the tube furnace and water quenched, the precipitation of the  $Ni_4Ti_3$  phase from the B2 NiTi matrix was not suppressed. Based on the

time-temperature transformation curves found in references [1,4], this phase transformation occurs within tens to hundreds of milliseconds and would be difficult, if not impossible, to prevent in these Ni-rich alloys.

The TEM bright-field image of the SA 55NiTi, Figure 3.2(c), reveals strain contrast within the microstructure, which masked the microstructure morphology. These Bragg-scattering effects are substantially reduced in a scanning TEM – high angle annular dark field (STEM-HAADF) image where scattering is primarily from Rutherford or nuclear effects. In such images, bright contrast originates from phases with higher atomic number atoms, which will be the Ni-rich phases. The STEM-HAADF image of Figure 3.2(d) clearly reveals a microstructure composed of a high volume fraction of individual, nanoscale  $\text{Ni}_4\text{Ti}_3$  precipitates separated by a continuous B2 NiTi matrix in the form of thin channels (~5-10 nm in width). SEM micrographs (not shown for space considerations) could not resolve these nanoscale precipitates nor were any coarse precipitates observed. The numerous and small length scale of  $\text{Ni}_4\text{Ti}_3$  supports a high driving force for nucleation and growth upon quenching. The same nanoscale microstructure was noted for specimen aged at 400°C for 100 hours. The lack of an evolving microstructure contributed to the retained high hardness, Figure 3.1.

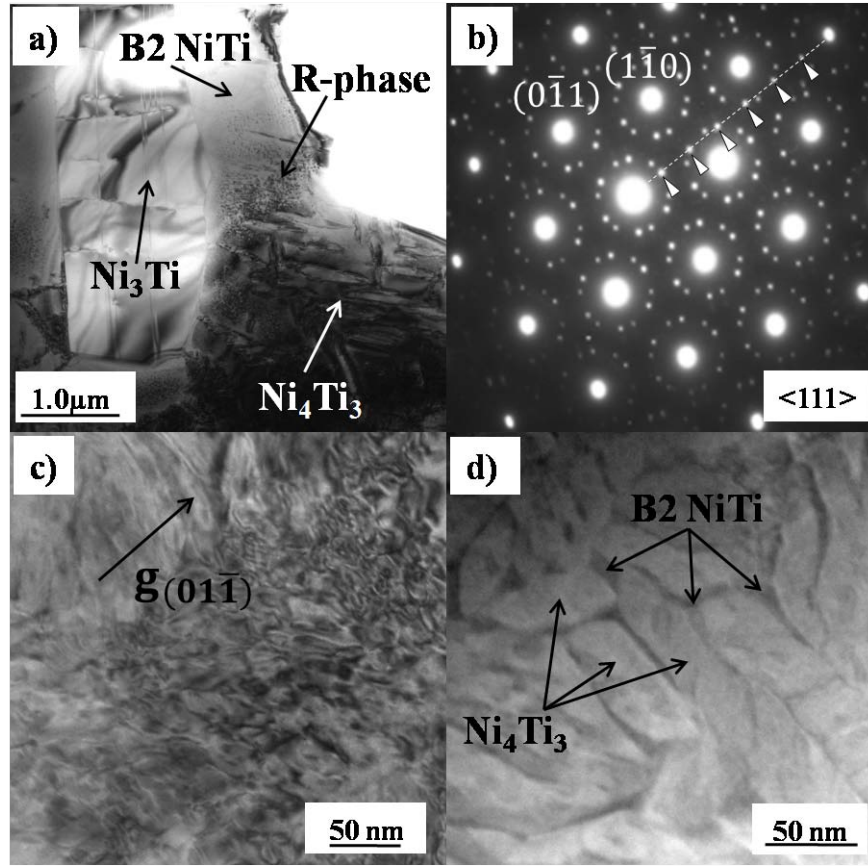


**Figure 3.2.** (a) Many-beam bright field image of the as-received microstructure of the 55NiTi. (b) SAED pattern from the [111] zone of the SA condition confirming the presence of Ni<sub>4</sub>Ti<sub>3</sub> precipitates, evident by the x/7 reflections along the <123> reciprocal vector of the B2 phase (highlighted by the arrows) (c) Two-beam bright-field micrograph showing strain contrast around the Ni<sub>4</sub>Ti<sub>3</sub> precipitates in the B2 NiTi matrix of the SA condition. (d) STEM-HAADF image of the SA microstructure revealing a high volume fraction of the Ni<sub>4</sub>Ti<sub>3</sub> precipitate phase (bright contrast) with very narrow B2 NiTi matrix channels (dark contrast) between the individual precipitates.

In contrast, the microstructure of the 55NiTi specimen aged at 750°C for 1 hour is dramatically different. The back-scattered SEM image of Figure 3.3(a) reveals much coarser precipitate morphologies as well as the presence of Ni<sub>3</sub>Ti<sub>2</sub> and Ni<sub>3</sub>Ti. These phases, along with the B2 NiTi matrix, were confirmed by XRD, whose scan is plotted in the Appendix Figure (Figure 3.5). The higher aging temperature (750°C) provided sufficient thermal energy for the decomposition of the metastable Ni<sub>4</sub>Ti<sub>3</sub> phase to the more thermodynamically stable Ni<sub>3</sub>Ti<sub>2</sub>

and  $\text{Ni}_3\text{Ti}$  phases [4,11]. The presence and coarsening of these phases resulted in a dramatic decrease in hardness on par with those measured and characterized in the as-received condition.

While the hardness decrease in the specimen aged at  $400^\circ\text{C}$  for 336 hours was relatively slight as compared to that observed in the  $750^\circ\text{C}$  for 1 hour, the onset of the decrease is apparent in the microstructure. The SEM micrograph in Figure 3.3(b), with its XRD scan shown in the online appendix figure, indicated that the  $\text{Ni}_4\text{Ti}_3$  has begun to decompose to the coarser  $\text{Ni}_3\text{Ti}$  phase, which as previously shown results in a drop in hardness. Though this decomposition has initiated, the hardness remained relatively high indicating that significant  $\text{Ni}_4\text{Ti}_3$  strengthening is still present. Interestingly, the SEM micrographs (and TEM not shown for space considerations) did not reveal the presence of  $\text{Ni}_3\text{Ti}_2$  phase. This result may suggest a direct decomposition of B2  $\text{NiTi} + \text{Ni}_4\text{Ti}_3$  to B2  $\text{NiTi} + \text{Ni}_3\text{Ti}$  without the intermediate metastable  $\text{Ni}_3\text{Ti}_2$  phase formation.

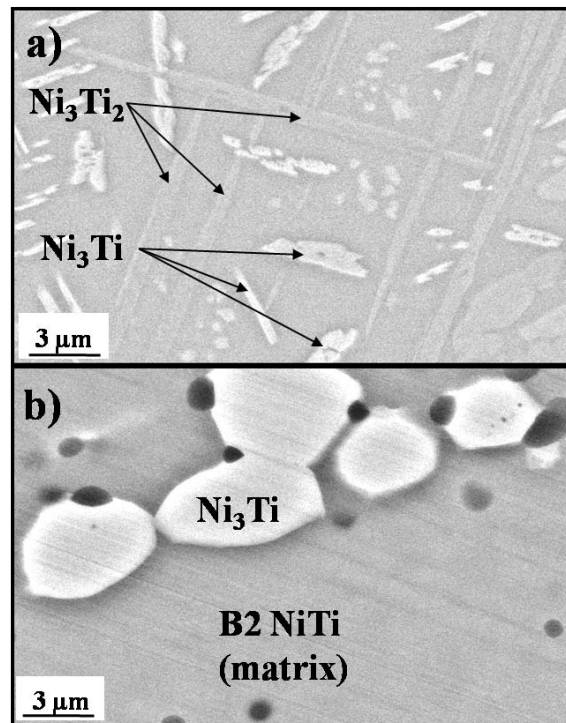


**Figure 3.3.** (a) SEM back-scattered image of a 55NiTi specimen aged at  $750^\circ\text{C}$  for 1 hour revealing coarse  $\text{Ni}_3\text{Ti}_2$  and  $\text{Ni}_3\text{Ti}$  phases. (b) SEM back-scattered image of a 55NiTi specimen aged at  $400^\circ\text{C}$  for 336 hrs showing the initial decomposition of the B2  $\text{NiTi} + \text{Ni}_4\text{Ti}_3$  to B2  $\text{NiTi} + \text{Ni}_3\text{Ti}$  phases.

Future work is underway to definitively address the decomposition pathways.

Figure 3.1 clearly demonstrates that the 55NiTi alloy does not exhibit a peak in hardness as commonly observed in typical precipitation strengthened alloys. Since the alloy's peak hardness occurs upon water quenching and remains unaffected with aging at 400°C to at least 100 hours, this suggests that the maximum amount of Ni<sub>4</sub>Ti<sub>3</sub> formed on quenching and did not undergo appreciable changes in size or volume fraction. This conclusion is supported by comparison of the observed and expected fraction of Ni<sub>4</sub>Ti<sub>3</sub> phase in the alloy. The fraction of the Ni<sub>4</sub>Ti<sub>3</sub> phase in the SA alloy was estimated by the area of precipitates relative to the total image area in the STEM-HAADF micrograph of Figure 3.2(d), which assumes the precipitate is through the foil thickness. This value was approximately 69% and is in excellent agreement, considering its assumptions, with the expected 71% value determined from a simple lever rule. The lever rule calculation was done by projecting Ni<sub>4</sub>Ti<sub>3</sub> as a line compound at 57NiTi (at.%) and the B2 NiTi also being a line compound at 50NiTi. This latter line composition is validated by the phase diagram in reference [12] in which B2 NiTi does indeed exhibit a line compound composition at temperatures below approximately 600°C. Hence, these two phase compositions bound the only two phases seen experimentally in the SA 55NiTi specimen.

It is well known that as the microstructure grain size decreases, the hardness increases, commonly referred to as the Hall-Petch effect. Considering the micron-plus grain size of the starting material created by solutionizing and holding at such a high temperature, this is not a contributing microstructural effect for the anomalous increase in hardness. In general, there are three principle strengthening mechanisms attributed to precipitation of secondary phases in an alloy matrix. The first mechanism is coherency strain hardening where dislocations interact with the strain fields that result from the misfit between the matrix and precipitate phase. The strain

contrast for the 400°C specimen, Figure 3.2(c), is directly related to the coherency strain and high volume fraction of the Ni<sub>4</sub>Ti<sub>3</sub> precipitates present in the B2 matrix. Such strain would be a contributing factor to the overall hardness of the material. Tirry *et al.* [14] reported for 52NiTi (at.%) that the strain in the B2 NiTi matrix was at its greatest value when the precipitate-to-precipitate spacing was approximately 16 nm. Though higher Ni concentration-strain relationships have not been reported, this spacing would decrease with increasing volume fraction of precipitate and would be expected to contribute even more to the overall strength and hardness of the alloy.

The second and third mechanisms of precipitation strengthening are associated with direct dislocation interactions with the precipitates' crystallography, size, and morphology. For example, chemical hardening occurs when a dislocation cuts through the precipitate by the creation of additional surface area as well as the formation of an anti-phase boundary. However, this mechanism is limited to matrix - precipitate systems with similar or related slip systems that are aligned across the interface [15]. The third is dispersion hardening when a dislocation has to move around or over a precipitate. This is generally accomplished by dislocations either bowing between the particles resulting in Orowan loops or cross slipping around them to produce prismatic loops [15]. In either case, the flow stress increases inversely to the distance between precipitates [15]. The relative contributions of each will depend on the particular matrix – precipitate properties and microstructure morphology.

The high volume fraction of Ni<sub>4</sub>Ti<sub>3</sub> precipitate phase and its morphology in the matrix, Figure 3.2(d), would imply that the latter strengthening mechanism is substantial. Yang *et al.* [16] reported the Young's modulus of Ni<sub>4</sub>Ti<sub>3</sub> and B2 NiTi to be  $163 \pm 4$  and  $118 \pm 4$  GPa, respectively, with the precipitate phase being elastically stiffer. Additionally, both phases are

ordered intermetallic structures where the generalized stacking fault energy (GSFE) for slip would be high. Unfortunately, the experimental strain contrast in Figure 3.2(c) prevents clear identification of dislocations or slip planes in either phase. To determine the energy hierarchy for slip, molecular dynamic (MD) simulations [17] were utilized to calculate the GSFE surfaces for the most probable slip systems in the B2 NiTi matrix and the Ni<sub>4</sub>Ti<sub>3</sub> precipitate phases. The MD simulations presented in figure 4 have been performed utilizing the LAMMPS code [18] and the Ni-Ti embedded atom method potentials found in reference [19]. The GSFE curves were calculated by rigidly shifting two semi-infinite blocks of crystal on the NiTi (011) and Ni<sub>4</sub>Ti<sub>3</sub> (111) planes with either a 20 x 20 or 40 x 40 displacement mesh, respectively, and the atom positions perpendicular to the slip plane were allowed to relax. The choice of planes is based on either experimental observation in B2 NiTi [20] or close-packed plane arrangements in Ni<sub>4</sub>Ti<sub>3</sub>, where to the authors' knowledge, no experimental data of slip has been reported.

The calculated GSFE surfaces for B2 NiTi, Figure 3.4(a), as compared to Ni<sub>4</sub>Ti<sub>3</sub>, Figure 3.4(b), is nearly one-half the energy. Given the higher GSFE and the lower rhombohedral symmetry of the Ni<sub>4</sub>Ti<sub>3</sub> phase, deformation would most likely be accommodated in the cubic B2 NiTi phase. Considering that the B2 NiTi matrix consists of extremely narrow channels (<10 nm spacing between precipitates), Orowan dislocation propagation by a bypass mechanism would be quite difficult, as the stress to propagate a dislocation scales inversely with precipitate spacing, and result in extremely high strength and hardness. Hence, the coupled intrinsic mechanical attributes of each phase and the microstructure formed from solutionizing and water quenching is believed to account for the anomalous high hardness values observed. With sufficient time or

higher aging temperatures, the strengthening  $\text{Ni}_4\text{Ti}_3$  phase decomposes and coarser  $\text{Ni}_3\text{Ti}_2$  and/or  $\text{Ni}_3\text{Ti}$  precipitates form. This change in microstructure results in a dramatic loss of hardness, as confirmed by the  $750^\circ\text{C}$  aged specimen.

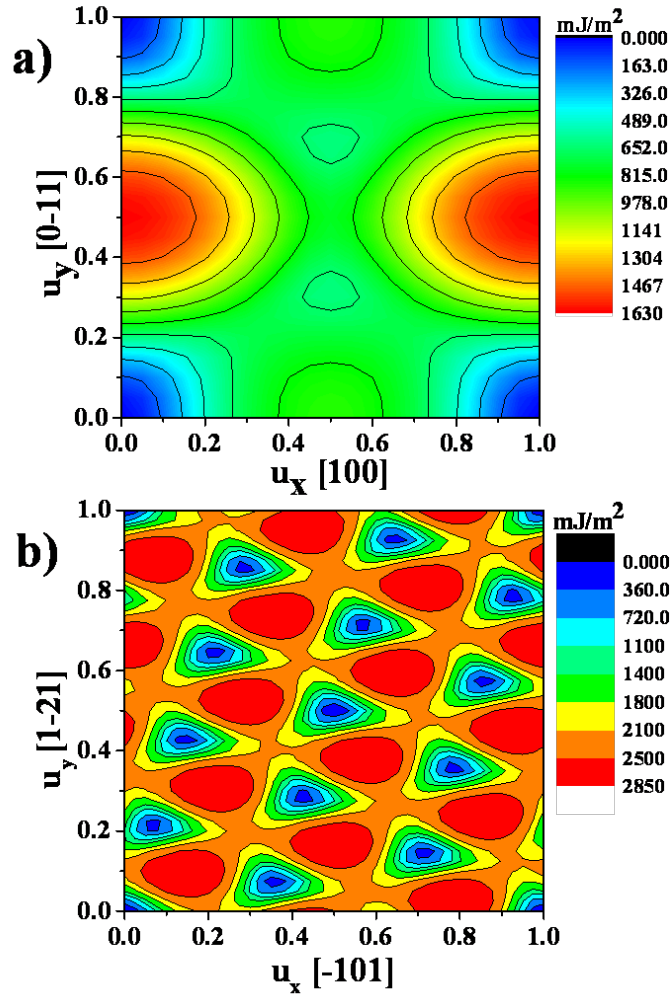
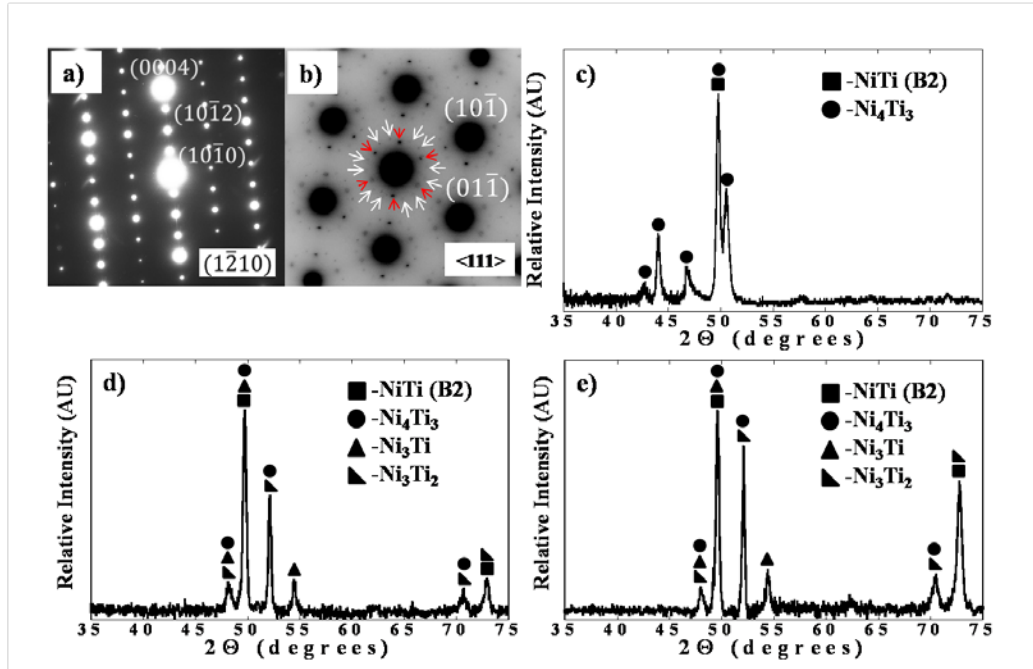


**Figure 3.4.** MD simulations of the GSFE surfaces for (a) (011) NiTi plane and (b) (111)  $\text{Ni}_4\text{Ti}_3$  plane. The x-y axis for each figure represents the crystallographic direction on each surface plane with the increments being the fractional displacements along that particular direction. Note the surface energies are nearly double for  $\text{Ni}_4\text{Ti}_3$  as compared to NiTi for equivalent colors.

### 3.4 Conclusions

A 55NiTi alloy was SA at 1050°C in the B2 NiTi phase field and subsequently water quenched. After quenching, electron imaging and diffraction indicated that the alloy was comprised of a B2 NiTi matrix with a nearly instantaneous pseudo-equilibrium fraction of nanoscale Ni<sub>4</sub>Ti<sub>3</sub> precipitates. The SA alloy had a hardness of 644 ± 5.1 VHN, which is comparable to tool steels, and retained this high hardness after aging at 400°C to least 100 hours. This processing resulted in an approximate 66% increase in hardness as compared to the as-received (hot-rolled) alloy. MD simulations of the GSFE suggested that deformation would most likely be accommodated by the softer B2 NiTi matrix than the harder Ni<sub>4</sub>Ti<sub>3</sub> precipitates. However, the narrow, channel-like morphology of the B2 matrix would make it difficult to propagate dislocations within this microstructure. The sluggish decomposition kinetics of Ni<sub>4</sub>Ti<sub>3</sub> contributed to its ability to retain the high hardness for extended times at modest temperatures. Aging the alloy at 750°C for 1 hour resulted in the rapid decomposition of the Ni<sub>4</sub>Ti<sub>3</sub> towards the thermodynamically stable Ni<sub>3</sub>Ti phase and the loss of the narrow, nanoscale channel morphology. Consequently, the hardness decreased significantly. This alloy's high hardness now expands generic Nitinol uses beyond traditional shape memory and superelastic applications, thus yielding a material that would be advantageous in various turbomachinery and other structural applications.



**3.5 (Appendix Figure).** Phase identification: (a) SAED pattern taken from the labeled  $\text{Ni}_3\text{Ti}$  region in figure 2(a) (b) SAED pattern taken from the  $[111]$  B2 NiTi zone axis from the labeled  $\text{Ni}_4\text{Ti}_3$  region in Figure 3.2(a). Additional diffraction spots confirms  $\text{Ni}_4\text{Ti}_3$  (white arrows) and R-phase (red arrows). (c) XRD of the SA 55NiTi specimen (d) XRD of 55NiTi sample aged at  $750^\circ\text{C}$  for 1 hour (e) XRD of 55NiTi sample aged at  $400^\circ\text{C}$  for 336 hours. Note, the XRD scans are from bulk specimens (not powder) indicating care in any interpretation of the XRD peak intensities.

### 3.5 References

- [1] K. Otsuka, X. Ren, Prog.Mater. Sci. 50 (2005) 511.
- [2] T.W. Duerig, K.N. Melton, D. Stockel, C.M. Wayman, Engineering Aspects of Shape Memory Alloys, Butterworth-Heinemann, London, 1990.
- [3] T.B. Massalski, H. Okamoto, P.R. Subramanian, L. Kacprzak, Binary alloy phase diagrams, second ed. ASM International, Materials Park, OH; 1990. p. 2874.
- [4] M. Nishida, C.M. Wayman, T. Honma, Metall. Mater. Trans. A, 17 (1986) 1505.
- [5] J.I. Kim, S. Miyazaki, Acta Mater. 53 (2005) 4545.
- [6] W.J. Buehler, F.E. Wang, Ocean Eng. 1 (1968) 105.

- [7] W.J. Buehler, "Intermetallic Compound Based Materials for Structural Applications," 7th NAVY Science Symposium: Solution to NAVY Problems Through Advanced Technology, Office of Naval Research, Arlington, VA, report number AD421708(64N15101), May 1963.
- [8] C. DellaCorte, S.V. Pepper, R. Noebe, D.R. Hull, G. Glennon, "Intermetallic Nickel-Titanium Alloys for Oil-Lubricated Bearing Applications," NASA/TM 2009-215646 (March 2009).
- [9] C. DellaCorte, R.D. Noebe, M.K. Stanford, S.A. Padula, Resilient and Corrosion-Proof Rolling Element Bearings Made from Superelastic Ni-Ti Alloys for Aerospace Mechanism Applications, in: Y.R. Takeuchi, W.F. Mandler (Eds.), Rolling Element Bearings, ASTM International, West Conshohocken, PA, 2012, p. 143-166.
- [10] C. DellaCorte, W.A. Wozniak, Design and Manufacturing Considerations for Shockproof and Corrosion-Immune Superelastic Nickel-Titanium Bearings for a Space Station Application, NASA/TM 2012-216015 (May 2012).
- [11] R.R. Adharapurapu, F. Jiang, K.S. Vecchio, *Mater. Sci. Eng. A*, 527 (2010) 1665.
- [12] T.T. Sasaki, B.C. Hornbuckle, R.D. Noebe, G.S. Bigelow, M.L. Weaver, G.B. Thompson, *Metall. Mater. Trans. A*, 44 (2013) 1388.
- [13] T. Saburi, S. Nenno, T. Fukuda, *J. Less-Common Met.* 125 (1986) 157.
- [14] W. Tirry, D. Schryvers, *Acta Mater.* 53 (2005) 1041.
- [15] G. Gottstein, *Physical Foundations of Material Science*, Springer, Germany, 2004.
- [16] Z.Q. Yang, W. Tirry, D. Larnoen, S. Kulkova, D. Schryvers, *Acta Mater.* 56 (2008) 395.
- [17] H. Van Swygenhoven, P.M. Derlet, A.G. Froseth, *Nat. Mater.* 3 (2004) 399.
- [18] S. Plimpton, *J. Comput. Phys.* 117 (1995) 1.
- [19] L. Ward, A. Agrawal, K.M. Flores, W. Windl, Rapid Production of Accurate Embedded-Atom Method Potentials for Metal Alloys. arXiv:1209.0619. (2012).
- [20] T. Ezaz, J. Wang, H. Sehitoglu, H.J. Maier, *Acta Mater.* 61 (2013) 67.

## CHAPTER 4

### HARDENING BEHAVIOR AND PHASE DE-COMPOSITION IN VERY NICKEL-RICH NITINOL ALLOYS<sup>3</sup>

#### **Abstract**

A series of Ni-rich Nitinol compositions spanning from 53NiTi to 58NiTi (at.%) have been solutionized at 1050°C and aged at 400, 625, and 750°C for varying lengths of time to determine the effect of precipitation strengthening on hardenability. Compositions of 55NiTi, 56NiTi, and 57NiTi displayed peak hardness values of  $649.4 \pm 4.5$ ,  $649.4 \pm 4.7$ , and  $634.4 \pm 5.4$  VHN, respectively, on quenching from the solutionizing temperature of 1050°C. These hardness values are on par with tool steels. Upon aging at 400°C, all but the 55NiTi and 56NiTi compositions exhibited a decrease in hardness initiating between 1 and 10 hrs for the lower Ni alloys and after 100 hrs for the highest Ni containing alloys. The high hardness was attributed to the precipitation of a high volume fraction of platelet-shaped Ni<sub>4</sub>Ti<sub>3</sub> that resulted in narrow B2 NiTi matrix channels. These channels provided a microstructure-driven strengthening morphology. Upon increasing Ni content to greater than 56NiTi and increasing the aging time and temperature, the Ni<sub>4</sub>Ti<sub>3</sub> phase decomposed to either Ni<sub>3</sub>Ti<sub>2</sub> and/or Ni<sub>3</sub>Ti with a subsequent loss in hardness. The decomposition morphology between the precipitates was characterized by serial sectioning showing that Ni<sub>4</sub>Ti<sub>3</sub> platelets act as a heterogeneous nucleation sites and subsequent Ni-reservoirs during the growth of globular Ni<sub>3</sub>Ti precipitates.

<sup>3</sup>A manuscript has been prepared for the work in this chapter for publication in Journal of Alloys and Compounds.

## 4.1 Introduction

The thermoelastic martensitic transformation behavior in binary NiTi, commonly referred to as Nitinol, is known for its shape memory and superelastic behaviors [1]. Though these properties remain the dominant attribute for engineering applications, a recent report by DellaCorte *et al.* revealed that very Ni-rich compositions of Nitinol have a hardness on par with tool steels when properly heat treated [2]. Coupling this high hardness with corrosion resistance, ability to be lubricated, and stably non-magnetic behavior, very Ni-rich Nitinol alloys position themselves as candidates for bearing applications [3,4]. To date, this high hardness has only been reported in one specific very Ni-rich Nitinol alloy, i.e. 55Ni-45Ti alloy (at.%), with little to no exploration of this effect in other similar binary compositions.

Recently the authors have reported on the mechanisms that resulted in this high hardness in the 55Ni-45Ti alloy [5]. These Ni<sub>4</sub>Ti<sub>3</sub> precipitates have previously been shown to be critical in allowing Ni-rich Nitinol shape memory alloys to exhibit stabilizing influence on the transformation temperatures and dimensional stability of Ni-rich Nitinol shape memory alloys upon repeated cycling through the martensitic transformation [6,7]. The seemingly anomalous hardness rise now noted in these alloys was attributed to the precipitation of a large volume fraction of nanoscale Ni<sub>4</sub>Ti<sub>3</sub> precipitates the promoted thin channels of B2 NiTi matrix phase. Since the matrix is the softer or more likely deforming phase, such a microstructure would result in a potent Orowan strengthening behavior. Though Ni<sub>4</sub>Ti<sub>3</sub> has been critical in each of the aforementioned attributes, most of this research focused on Ni contents  $\leq 52$  at.% because higher Ni concentrations significantly suppresses the transformation temperatures [8]. This explains the interest gap in researching very-Ni rich Nitinol until DellaCorte *et al.* [2] recently pursued these materials for bearing applications.

Consequently, a systematic study of hardness as a function of Ni content is explored here to determine the compositional range for this emerging new high hardness property. The aim of this work is to define the optimal compositional range where a maximum in hardness occurs and begin to determine the stability of the alloys within that finding. From this study, the optimal binary compositions and heat treatments for hardness can then be elucidated, particularly since the hardening phase,  $\text{Ni}_4\text{Ti}_3$ , is known to be metastable [9].

Several reports [1,9] have shown that when a Ni-rich Ni-Ti alloy is solutionized in the B2 phase field, quenched, and then aged at moderate temperatures of less than  $\sim 680^\circ\text{C}$ , the  $\text{Ni}_4\text{Ti}_3$  phase will precipitate. This phase has a rhombohedral structure and is thermodynamically metastable. With sufficient time, the  $\text{Ni}_4\text{Ti}_3$  will decompose to the metastable  $\text{Ni}_3\text{Ti}_2$  and then to the thermodynamically stable  $\text{Ni}_3\text{Ti}$  phase. If the aging temperature is between  $\sim 680$  to  $\sim 750^\circ\text{C}$ , the  $\text{Ni}_3\text{Ti}_2$  phase precipitates (with  $\text{Ni}_4\text{Ti}_3$  formation being bypassed), and it then decomposes to  $\text{Ni}_3\text{Ti}$ . Aging temperatures greater than  $\sim 750^\circ\text{C}$  result in the direct precipitation of the  $\text{Ni}_3\text{Ti}$  phase. Much, if not all, of this phase stability work was done using a 52Ni-48Ti (at.%) alloy. Since the  $\text{Ni}_4\text{Ti}_3$  phase has been identified as the critical strengthening phase in a broader range of Ni-Ti alloys, elucidating its stability as a function of even more Ni-rich compositions is essential for developing such alloys for proposed structural applications [2-4]. Consequently this effort explores the stability of the  $\text{Ni}_4\text{Ti}_3$  phase and its relationship to hardening in Ni-Ti alloys containing 53 – 58 at.% Ni.

## 4.2 Experimental Background

A series of binary Ni-rich Ni-Ti alloys (e.g., 53Ni-47Ti, 54Ni-46Ti, 56Ni-44Ti, 57Ni-43Ti, and 58Ni-42Ti(at.%)) were fabricated as arc-melted 80 g. buttons of ~ 4 cm diameter. Starting with the appropriate weights of high purity elemental Ni and Ti constituents, the alloys were melted, and the ingots reversed and re-melted at least 4 times under a protective partial pressure of argon. Following casting, the individual buttons were homogenized in vacuum at 1050°C for 24 hours and furnace cooled. The buttons were then sectioned into smaller pieces and re-solution annealed at 1050°C for 10 hours followed by a water quench and subsequent aging at 400, 625, and 750°C for various times. The 55Ni-45Ti (at.%) data presented in conjunction with these specimens was taken from reference [5]. The solution treatment and quench was critical in achieving the high hardness. In contrast, furnace cooling allowed the formation of coarse stable and metastable Ni-rich precipitate phases resulting in a much lower hardness [10]. All of these solution annealing and aging processes were conducted in a tube furnace under a continuous flow of ultra-high purity Ar with the specimens wrapped in Ta foil to reduce the amount of oxidation. For any aging conditions longer than 24 hours, the specimens were again wrapped in Ta foil but encapsulated within a quartz tube backfilled with Ar to further minimize oxidation for these extended aging times.

Phase identification and microstructural characterization were performed by transmission electron microscopy (TEM), scanning electron microscopy (SEM), and X-ray diffraction (XRD). TEM samples were prepared by cutting 3 mm discs, grinding the discs to ~100  $\mu\text{m}$  in thickness, followed by dimpling the discs using a 6  $\mu\text{m}$  diamond suspension to a final thickness < 10  $\mu\text{m}$  in a Fischione Model 200 Grinder. Once dimpled, the discs were then ion milled using a Gatan 691 Precision Ion Polishing System until electron transparent perforations occurred in the dimpled

region. All specimens were analyzed in a FEI Tencai G2 F-20 Supertwin (scanning) transmission electron microscope ((S)TEM) operated at 200 keV. SEM specimens were roughly polished with 800 grit SiC paper to remove any residual surface oxide layer formed during the heat treatment process. Once the oxide layer was removed, the specimens were then polished using a 9  $\mu\text{m}$  and 3 $\mu\text{m}$  diamond solution in consecutive steps with a final polish with 0.05 $\mu\text{m}$  colloidal Si in a Buehler AutoMet 250 Grinder Polisher. SEM back-scattered images were taken using a JOEL 7000F. Electron Backscattered Diffraction (EBSD) was performed using the Oxford Aztec 2.2 platform. XRD was conducted on a Phillips X'Pert XRD system operated with a Cu  $K_{\alpha}$  radiation source at 40keV and 35mA. Hardness testing was determined using a Buehler Model 1600-6100 microhardness tester equipped with a Vickers diamond-pyramid indenter using a 1 kg load with a 15 sec. dwell time. Each specimen condition was indented 10 times with the mean hardness and standard deviation reported.

For particular specimens, serial sectioning to reveal the 3D microstructure morphology was done using a Tescan Lyra 3 XM Focus Ion Beam (FIB) – Field Emission SEM (FESEM). Back-scattered electron (BSE) images were collected at each of the 500 slices taken of the surface providing atomic contrast which enabled easier identification of the secondary phases and their morphologies. The total analyzed volume was 10 x 10 x 10  $\mu\text{m}$  with each slice being 20 nm with the FIB settings of 30 keV and 2 nA. A fiducial marker was milled into the adjoining material for post-processing imaging alignment. The 3D visualization was constructed using the Avizo Fire 6 platform.



and the low volume fraction of some phases. With that caveat, the x-ray scans represent a preliminary assessment of the phases present, which need to be confirmed with other techniques as described below.

The precipitation of secondary phases from the solutionizing condition is a result of either (1) intrinsically rapid nucleation of the phases upon quenching and/or (2) the solutionizing temperature was inadequate to completely dissolve all the phases. This would be of particular concern for the highest Ni content alloys where the exact solidus line, shown in Figure 4.1(c), maybe less established. In regards to (1), the nucleation of  $\text{Ni}_4\text{Ti}_3$  precipitates from the B2 matrix phase occurs in a time scale of milliseconds making it nearly impossible to suppress in Ni-rich alloys [1,9]. For item (2), the liquidus solubility curve for the high temperature B2 single phase field at  $\sim 58\text{NiTi}$  is at  $\sim 1090^\circ\text{C}$ , Figure 4.1(c), which is very near the  $1050^\circ\text{C}$  solutionizing temperature used in this study. Increasing the temperature much further to ensure a single phase condition is impractical because it would result in entering the liquid + B2 phase field. It is also worth noting that the phase diagram boundaries themselves are based on approximations with some inherent uncertainty. The microstructure of the solution annealed/quenched  $57\text{NiTi}$ , Figure 4.2(a), as well as  $58\text{NiTi}$  (not shown but similar to Figure 4.2(a)), revealed coarse globular  $\text{Ni}_3\text{Ti}$  and plate-shaped  $\text{Ni}_3\text{Ti}_2$  phases. The coarse  $\text{Ni}_3\text{Ti}$  and  $\text{Ni}_3\text{Ti}_2$  precipitates suggest that at this composition, the solutionizing temperature was inadequate to dissolve all the secondary phases. In comparison, the BSE SEM micrograph of the  $54\text{NiTi}$  solution annealed specimen did not show any coarse precipitates, Figure 4.2(b). Note that the  $53\text{NiTi}$ ,  $55\text{NiTi}$ , and  $56\text{NiTi}$  alloys all exhibited similar microstructures to that of  $54\text{NiTi}$  in Figure 4.2(b).

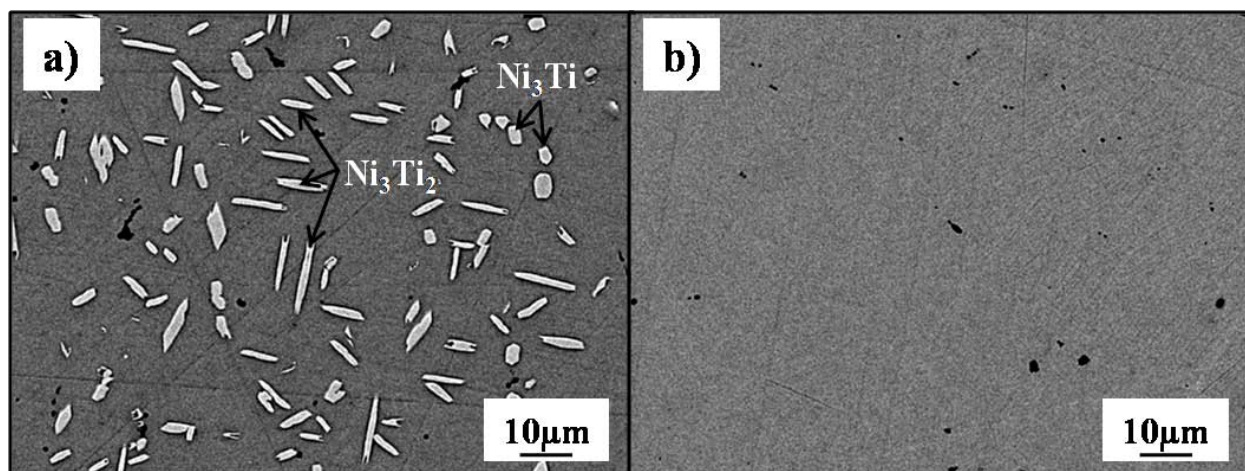


**Figure 4.2.** (a) BSE SEM micrograph of the 57NiTi solutionized/quenched microstructure revealing coarse  $\text{Ni}_3\text{Ti}$  and  $\text{Ni}_3\text{Ti}_2$  precipitates, indicated by the arrows, in a B2 matrix. The fine scale of  $\text{Ni}_4\text{Ti}_3$  precipitates at this magnification could not be observed. (b) BSE SEM micrograph of the 54NiTi solutionized/quenched microstructure where no obvious coarse precipitates were observed at this magnification.

TEM micrographs of the 53NiTi, 56NiTi, and 58NiTi specimens in the solutionized condition revealed that the  $\text{Ni}_4\text{Ti}_3$  phase identified in the XRD plots in Figure 4.1(b), was nanoscale in size. Several of these precipitates are indicated by white arrows in Figure 3, however, the strain contrast makes it difficult to resolve the individual  $\text{Ni}_4\text{Ti}_3$  precipitates, particularly in the higher Ni alloys. Selected area electron diffraction (SAED) patterns for the 54NiTi solution annealed sample are shown in Figure 4.3(d). The reflections were consistently indexed to the B2 and  $\text{Ni}_4\text{Ti}_3$  phases. In particular, the diffraction pattern taken from the [111] B2 matrix zone axis contains a series of extra reflections occurring at  $x/7$  positions along the  $\langle 123 \rangle$  reciprocal vector of B2. These reflections are indicative of  $\text{Ni}_4\text{Ti}_3$  [12]. Additional reflections indexed to the R-phase were noted in the [111] zone axis, which is not surprising since this phase is often associated with the precipitation of  $\text{Ni}_4\text{Ti}_3$  [1]. The microstructures of the 53NiTi, 55NiTi, and 56NiTi alloys were similar to the 54NiTi sample in the solution treated conditioned as determined by SEM and XRD. For the 57NiTi and 58NiTi, the coarse  $\text{Ni}_3\text{Ti}$  and

$\text{Ni}_3\text{Ti}_2$  precipitates observed in Figure 4.2(a), were not readily apparent in the TEM micrographs due to their size and spacing relative to the field of view typical of a TEM foil.

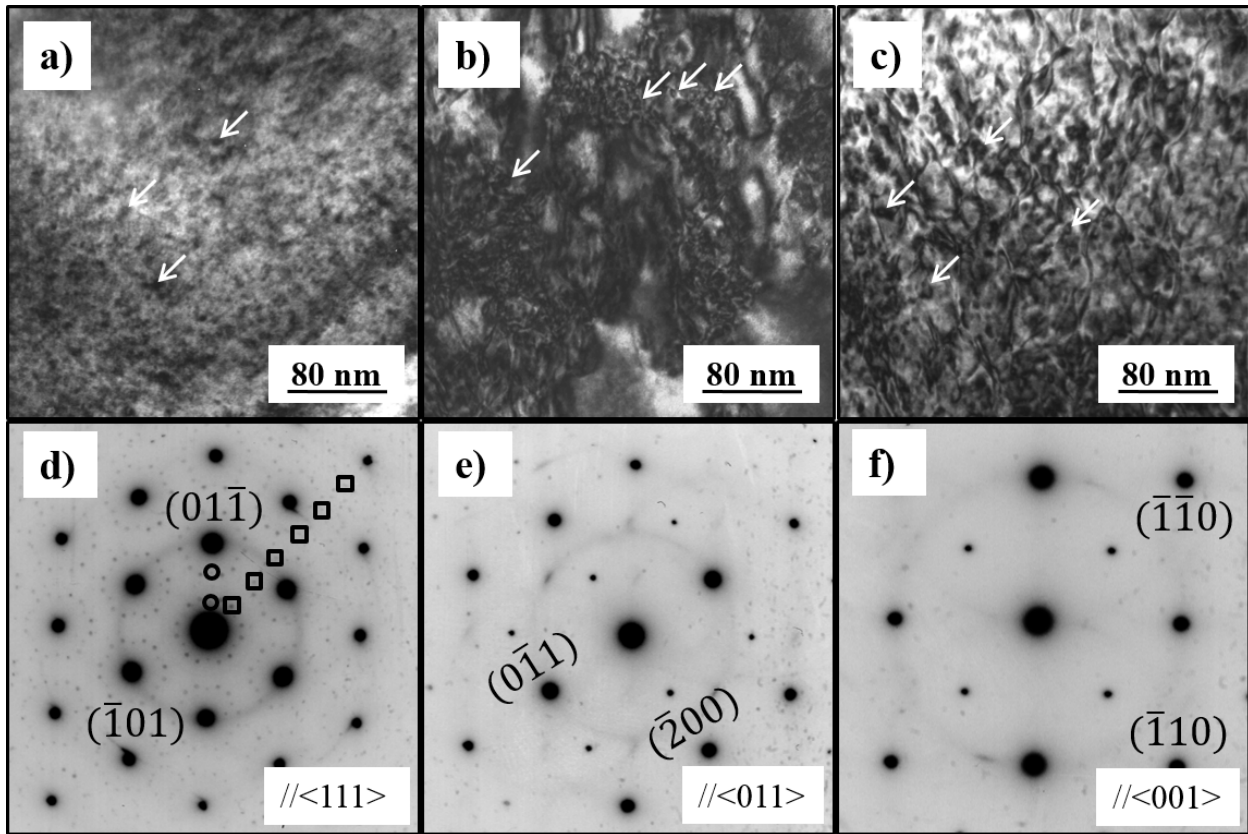


**Figure 4.3.** Multiple beam bright field image of the solution annealed condition for (a) 53NiTi, (b) 56NiTi, and (c) 58NiTi. Note the stark difference in strain contrast as Ni content is increased especially from 53NiTi to 56Ni. SAED patterns for the solution annealed condition for the 54NiTi sample from (d) the  $[111]$  zone axis of B2 matrix phase with squares highlighting the  $\text{Ni}_4\text{Ti}_3$  reflections and circles highlighting the R-phase, (e) the  $[011]$  zone axis of B2 matrix phase, and (f) the  $[001]$  zone axis of B2 matrix phase.

Upon extended aging at  $400^\circ\text{C}$ , the hardness quickly peaked and then continuously decreased for the 53NiTi and 54NiTi alloys, while much more modest reductions in hardness were noted for the higher Ni content alloys compared to their solution annealed and quenched versions. The SEM micrograph for the 300 hour aged 53NiTi specimen revealed coarsened versions of the  $\text{Ni}_4\text{Ti}_3$  phase, while the 56NiTi and 58NiTi specimens also began to decompose into the  $\text{Ni}_3\text{Ti}_2$  and equilibrium  $\text{Ni}_3\text{Ti}$  phases, Figure 4.4. Coarsening of the  $\text{Ni}_4\text{Ti}_3$  phase would

contribute to the loss of the optimal precipitate size and spacing that gave rise to a peak hardness value via an Orowan strengthening mechanism. Note that prior high resolution SEM micrographs were unable to easily resolve this phase until overaging occurred. The formation of  $\text{Ni}_3\text{Ti}_2$  and  $\text{Ni}_3\text{Ti}$  phases occurred at the expense of the  $\text{Ni}_4\text{Ti}_3$  phase, also contributing to a decrease in hardness.

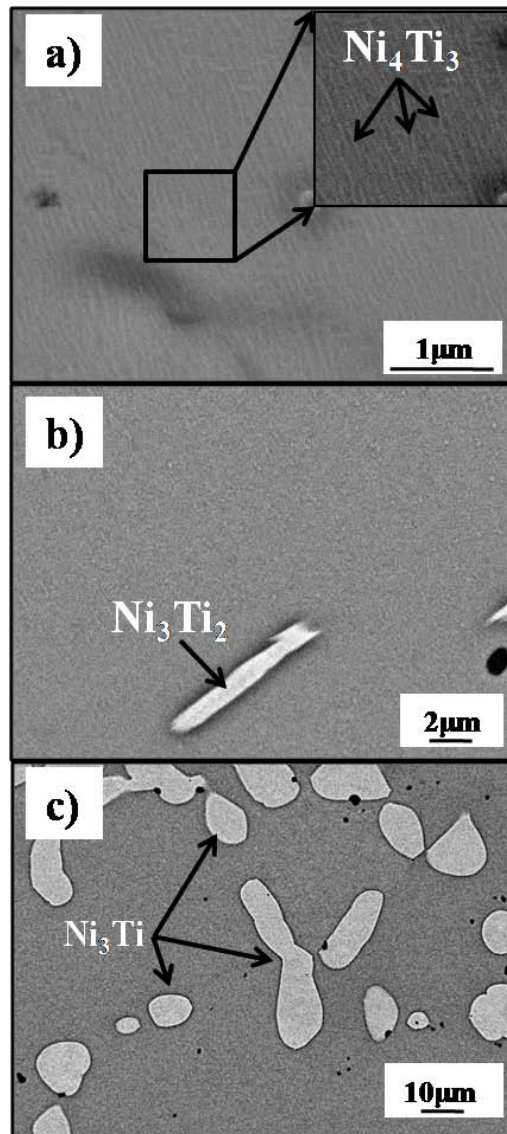


**Figure 4.4.** (a) BSE micrograph of 53NiTi specimen aged 300 hours at 400°C consisting of a B2 matrix phase and coarsened  $\text{Ni}_4\text{Ti}_3$  precipitates, (b) BSE micrograph of 56NiTi aged 300 hours at 400°C, and (c) BSE micrograph of 58NiTi specimen aged 300 hours at 400°C. In the latter two samples,  $\text{Ni}_3\text{Ti}_2$  (b) and  $\text{Ni}_3\text{Ti}$  (c) were observed in addition to  $\text{Ni}_4\text{Ti}_3$  and B2 matrix phases.

Finally to determine the stability of the  $\text{Ni}_4\text{Ti}_3$  precipitates with temperature for the various alloys, each alloy was subjected to  $625^\circ\text{C}$  and  $750^\circ\text{C}$  aging treatments for various times. These temperatures were based loosely on the  $\text{Ni}_3\text{Ti}_2$  and  $\text{Ni}_3\text{Ti}$  aging temperatures previously discussed in the introduction and detailed in reference [9].

Each alloy showed a decrease in hardness with increasing aging temperature and time, with the higher Ni content alloys showing a much quicker rate of hardness decrease, Figure 4.5, than seen in the  $400^\circ\text{C}$  aged conditions, Figure 4.1(a). The BSE SEM micrographs of the 53NiTi, 56NiTi, and 58NiTi aged for 48 hours at  $625^\circ\text{C}$  and  $750^\circ\text{C}$  are shown in Figure 4.6. For all alloys in both aging conditions, a variety of phases are present with each having a unique morphology. For these three alloys aged at  $625^\circ\text{C}$ , the B2 matrix phase was present with a high density of coarsened  $\text{Ni}_3\text{Ti}_2$  present, while the presence of equilibrium  $\text{Ni}_3\text{Ti}$  was seen in the two highest Ni content alloys, 56NiTi and 58NiTi. For the same alloys aged at  $750^\circ\text{C}$ , the B2 matrix phase remained present with a decreased amount of  $\text{Ni}_3\text{Ti}_2$  and an increased amount of coarsened  $\text{Ni}_3\text{Ti}$  present in the 53NiTi alloy, while 56NiTi and 58NiTi were found to have a B2 matrix with a distribution of coarse and fine  $\text{Ni}_3\text{Ti}$  present. This distribution is believed to be the result of a reduced amount of excess Ni present in the B2 matrix to allow for the fine  $\text{Ni}_3\text{Ti}$  to grow to the degree seen in the coarsened version. Clearly, the coarse precipitate microstructure resulted in the dramatic hardness drop.

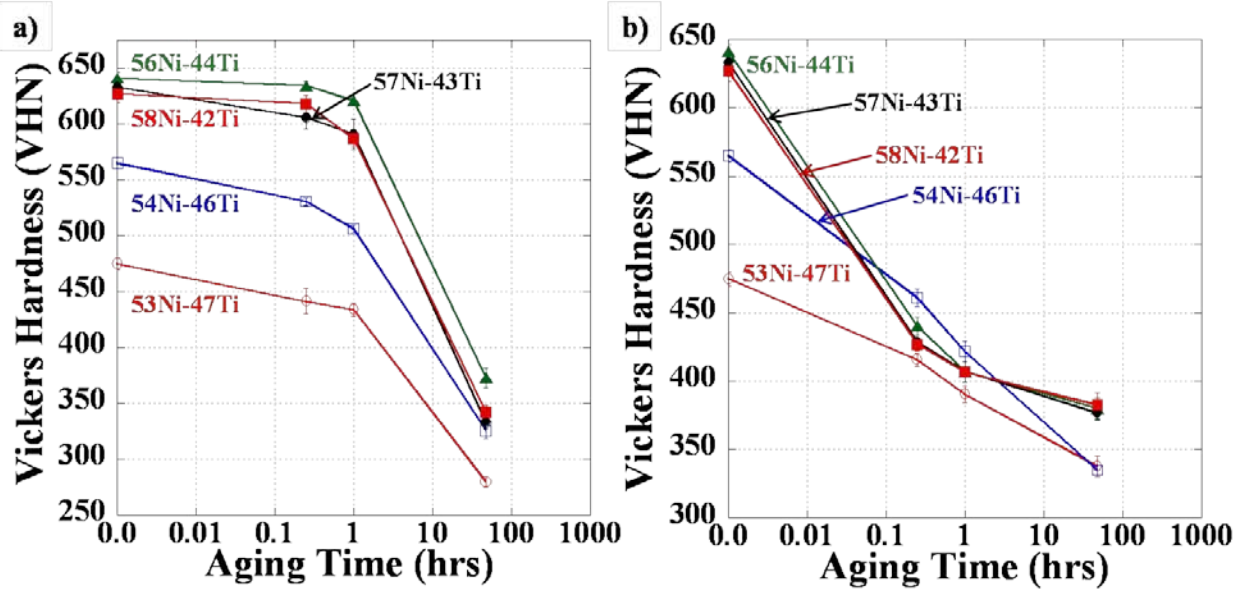


**Figure 4.5.** Aging curves for various Ni-rich Ni-Ti compositions aged at (a) 625°C and (b) 750°C for various times.

Phase identification of each of these phases was accomplished through observation of the morphology in the BSE SEM micrographs [13] and EBSD, Figure 4.6. Our EBSD results confirmed prior reports of the morphologies of these phases –  $\text{Ni}_4\text{Ti}_3$  being thin platelets,  $\text{Ni}_3\text{Ti}_2$  as coarse laths, and  $\text{Ni}_3\text{Ti}$  being globular in shape. Note, the SEM images and EBSD images do not necessarily correspond to the same field of view but are under the same processing conditions.

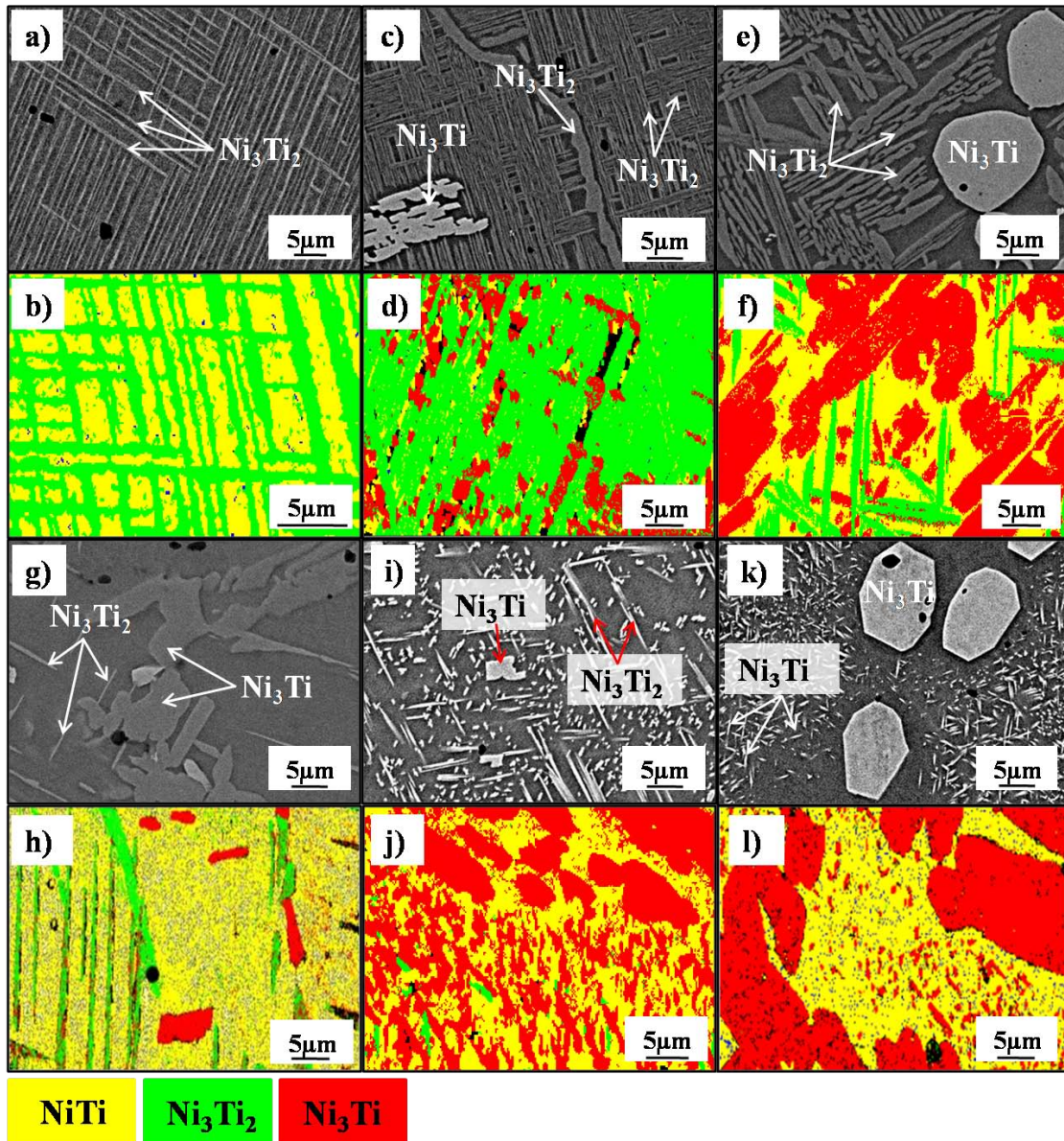


**Figure 4.6.** BSE micrographs of 53NiTi specimens aged 48 hours at (a) 625°C and corresponding (b) EBSD scan identifying phases present; BSE micrographs of 56NiTi specimens aged 48 hours at (c) 625°C and corresponding (d) EBSD scan identifying phases present; BSE micrographs of 58NiTi specimens aged 48 hours at (e) 625°C and corresponding (f) EBSD scan identifying phases present. BSE micrographs of 53NiTi specimens aged 48 hours at (g) 750°C and corresponding (h) EBSD scan identifying phases present; BSE micrographs of 56NiTi specimens aged 48 hours at (i) 750°C and corresponding (j) EBSD scan identifying phases present; BSE micrographs of 58NiTi specimens aged 48 hours at (k) 750°C and corresponding (l) EBSD scan identifying phases present.

#### 4.4 Discussion

Figure 4.1(a) indicated that there is an optimum level of Ni for maximum hardness, which is on the order of 55-56Ni. Lower Ni contents are significantly softer, whereas higher Ni contents also resulted in a slightly lower hardness. For these latter alloys, it is likely contributed to the difficulty to completely solutionize the alloys. The TEM micrographs showed that in each solution treated alloy (Figure 4.3), nanoscale  $\text{Ni}_4\text{Ti}_3$  phases were present, rationalized by their rapid precipitation kinetics upon quenching [1,4]. Since the precipitates can form within tens of microseconds [1,4], with higher Ni-content only increasing the driving force further, it was impossible to prevent their formation in this experimental set-up. As the Ni-content increased, the volume fraction of this phase would correspondingly increase. Based on a prior report for the 55NiTi alloy, the experimentally determined volume fraction, ~71%  $\text{Ni}_4\text{Ti}_3$  in the solution treated and quenched 55NiTi alloy, matched very well with the lever rule approximation taken from the phase diagram of Figure 4.2, where  $\text{Ni}_4\text{Ti}_3$  and NiTi are considered line compounds at temperatures under ~ 680°C. Using this lever rule principle, the 53NiTi content alloy would be ~43%  $\text{Ni}_4\text{Ti}_3$ , 54NiTi would be ~57%, 56NiTi would be ~86%, and 57NiTi would be 100% respectively. A volume fraction estimate for the 58NiTi was not done as it has a composition that would exceed this pseudo-binary approximation. A consequence of this higher volume fraction of  $\text{Ni}_4\text{Ti}_3$  in the microstructure would be a further decrease in the B2 matrix channel width between the precipitates, as shown in Figure 4.7.

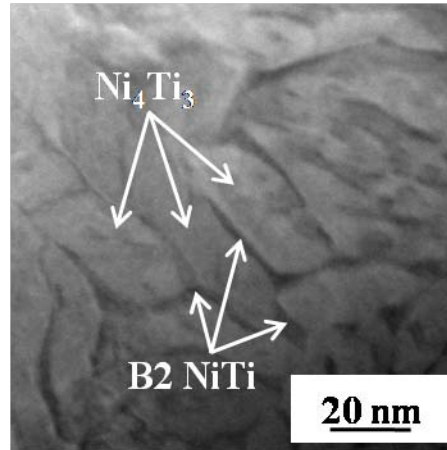


**Figure 4.7.** HAADF-STEM image from a 55NiTi alloy to give perspective of  $\text{Ni}_4\text{Ti}_3$  spacing and narrow B2 NiTi channels between the precipitates.  $\text{Ni}_4\text{Ti}_3$  volume fraction was  $\sim 71\%$  [5].

Since the shear stress is inversely proportional to the precipitate spacing for an Orowan strengthening mechanism [14], an increase in volume fraction, assuming a nearly constant precipitate size, would result in a corresponding increase in strength. The nanoscale formation of these precipitates, driven by the rapid nucleation kinetics, coupled with their platelet-like morphology, yielded a microstructure that is ideal for a high hardness alloy. The B2 phase is more ductile than the hard, brittle  $\text{Ni}_4\text{Ti}_3$  phase [5,15] resulting in likely dislocation propagation in the B2 matrix phase. Also, the relatively large size of the  $\text{Ni}_4\text{Ti}_3$  precipitates makes particle cutting less likely. Hence the narrow B2 channels provided a microstructural barrier for easy slip while alloys consisting of wider channels (lower  $\text{Ni}_4\text{Ti}_3$  precipitation fraction due to lower Ni-content) easier to deform. This was manifested in the lower hardness values, Figure 4.1(a).

In addition, the lower Ni content alloys qualitatively appeared to generate less strain contrast, Figure 4.3, which could also contribute in the loss of another hardening mechanism. Tirry *et al.* reported that in a 52NiTi alloy, the highest internal strains occurred with a precipitate spacing of  $\sim 16$  nm [16]. But the material was limited by the volume fraction of  $\text{Ni}_4\text{Ti}_3$  phase that could form. By increasing the fraction of  $\text{Ni}_4\text{Ti}_3$  precipitates, the inter-precipitate spacing would

decrease further and the corresponding strain created would increase, as evident by the qualitative strain contrast increase seen in the series of alloys in Figure 4.3. Unfortunately, due to the high strain contrast created by the precipitates, dislocation analysis was difficult, if not impossible, to perform in these narrower B2 matrix channels. Regardless, the increase in volume fraction of  $\text{Ni}_4\text{Ti}_3$  phase and corresponding increase in hardness in alloys containing up to 56% Ni provided further experimental evidence that this precipitate-driven microstructure contributed to the higher hardness.

Ideally, the 57NiTi alloy should be ~100%  $\text{Ni}_4\text{Ti}_3$ , which is expected to be an extremely hard and brittle phase. This was not observed due in part to the experimental difficulty in creating an exact line compound. The fact that  $\text{Ni}_3\text{Ti}_2$  and  $\text{Ni}_3\text{Ti}$  phases were present in the solutionized alloy indicated that an alloy composition may have been slightly off (or greater) than 57% Ni; but this could not be confirmed due to the limitation errors associated with our available measurement techniques. Consequently, this alloy would have a volume fraction of  $\text{Ni}_4\text{Ti}_3$ , similar to the 55NiTi and 56NiTi, and it did indeed have a hardness on par with those alloys. This alloy, as well as the 58NiTi alloy, exhibited coarse  $\text{Ni}_3\text{Ti}$  precipitates yet it was shown to have hardness values exceeding alloys that also had similar coarse precipitates, albeit after extending aging times and/or higher temperatures. This difference was attributed to the intrinsic nanoscale precipitation of a large volume fraction of  $\text{Ni}_4\text{Ti}_3$  upon quenching that occurred for this alloy as compared to the decomposition and coarsening of those phases by the other alloys. Additionally, the micro-indenter was able to sample these ‘nanoscale’ strengthened regions in 57NiTi and 58NiTi that was in between the large, but separated coarse  $\text{Ni}_3\text{Ti}$  precipitates. By increasing the Ni content to 58NiTi, the bulk composition was now driven past the  $\text{Ni}_4\text{Ti}_3$  composition, further supported by the increased amount of  $\text{Ni}_3\text{Ti}_2$  and  $\text{Ni}_3\text{Ti}$  present in

the alloy. Despite a bulk composition past the  $\text{Ni}_4\text{Ti}_3$  line composition, the alloy would still have a fraction of this phase based on a pseudo-equilibrium lever rule between  $\text{Ni}_4\text{Ti}_3$  and  $\text{Ni}_3\text{Ti}$  in Figure 4.1(c).

The four highest Ni content alloys, aged at  $400^\circ\text{C}$ , revealed reasonably stable hardness values out to  $\sim 100$  hours, Figure 4.1(a). Based on the initial as-quenched hardness, the alloys would be expected to have a similar volume fraction of  $\text{Ni}_4\text{Ti}_3$  phase. Also, within each alloy the nanoscale precipitates are essentially the same size, as seen in Figure 4.3. Hence there does not appear to be a high driving force for coarsening as each precipitate is relatively equivalent in size in the microstructure, i.e. a lack of Ostwald ripening to larger precipitates consuming smaller precipitates. In addition, the aging temperature ( $400^\circ\text{C}$ ) was relatively low and the interfaces being relatively flat in the platelet like morphology, i.e. an infinite radius of curvature, could all contribute to a low coarsening rate. Since the  $\text{Ni}_4\text{Ti}_3$  phase has been reported to take tens to hundreds of hours to decompose to the metastable  $\text{Ni}_3\text{Ti}_2$  and thermodynamically stable  $\text{Ni}_3\text{Ti}$  at this temperature [1,9], the hardness remained relatively constant over a long period of time. However, as the alloy deviated further from the high  $\text{Ni}_4\text{Ti}_3$  content, it does appear that coarsening became easier indicative of the classical parabolic age hardening curve seen for the 53NiTi and 54NiTi alloys in Figure 4.1(a).

When the temperature was increased to either  $625^\circ\text{C}$  or  $750^\circ\text{C}$ , sufficient thermal energy was present to accelerate the coarsening and decomposition of the  $\text{Ni}_4\text{Ti}_3$ , Figure 4.6. The dramatic drop in hardness, Figure 4.5, at these aging temperatures supports the contention that high hardness is indeed driven by the microstructure. As discussed previously, the initial presence of the  $\text{Ni}_3\text{Ti}_2$  and  $\text{Ni}_3\text{Ti}$  phases, Figure 4.2(b), was attributed to the lack of solutionizing in the single phase B2 region for the 57NiTi and 58NiTi alloys. With aging of all the alloys at

elevated temperatures, the  $\text{Ni}_3\text{Ti}_2$  phase formed an almost continuous film along the grain boundaries; such boundaries would act as heterogeneous nucleation sites as well as provided 'fast-track' pathways for Ni diffusion. This phase also nucleated homogeneously within the grains. In contrast, the  $\text{Ni}_3\text{Ti}$  phase, precipitated predominantly within the grains.

Using serial sectioning, the morphological relationship between the  $\text{Ni}_4\text{Ti}_3$  decomposition to that of the  $\text{Ni}_3\text{Ti}$  precipitation was studied in a 57NiTi alloy aged 1000 hours at 400°C. Figure 4.8 is micrographs from four successive slices with a marked region showing the morphological connection between a  $\text{Ni}_4\text{Ti}_3$  platelet and a globular  $\text{Ni}_3\text{Ti}$  phase. These images provide morphological insights as to how the phases evolved during the decomposition process. From these images, the  $\text{Ni}_4\text{Ti}_3$  precipitate appears to act as a heterogeneous nucleation site for the  $\text{Ni}_3\text{Ti}$  phase and then serves as a reservoir of Ni to the growing precipitate. As the  $\text{Ni}_4\text{Ti}_3$  phase decomposed, evident by its smaller size in Figure 4.8, the  $\text{Ni}_3\text{Ti}$  coarsened. These 3D images provide further insights into the decomposition. In the prior work [9], done with a 52NiTi alloy, at this aging temperature, the phases would decompose as  $\text{Ni}_4\text{Ti}_3 \rightarrow \text{Ni}_3\text{Ti}_2 \rightarrow \text{Ni}_3\text{Ti}$ . With this higher Ni content alloy shown here, at this equivalent temperature, the  $\text{Ni}_4\text{Ti}_3$  was able to directly decompose to the thermodynamically stable  $\text{Ni}_3\text{Ti}$  phase.

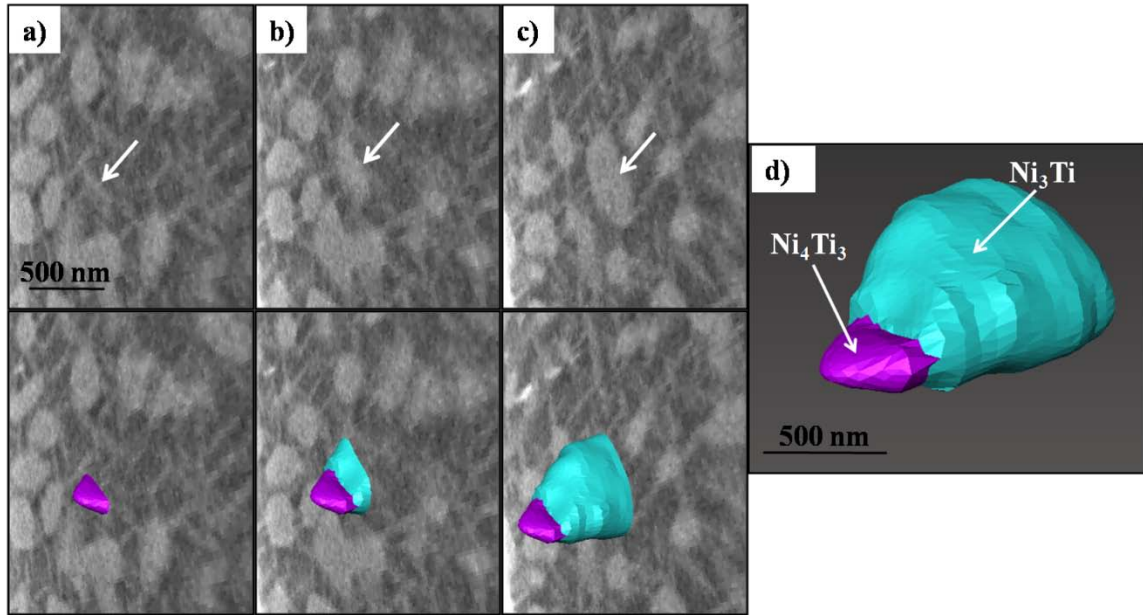


**Figure 4.8.** Consecutive images of 57NiTi specimen aged 1000 hours at 400°C starting at (a) and finishing at (c) from serial sectioning procedure highlighting a Ni<sub>3</sub>Ti heterogeneously growing off of Ni<sub>4</sub>Ti<sub>3</sub> precipitates, which act as a reservoir for the extra Ni needed for the growth of the Ni-rich phase; (d) Reconstructed model of the Ni<sub>3</sub>Ti growing from a Ni<sub>4</sub>Ti<sub>3</sub> precipitate.

#### 4.5 Conclusion

A series of Ni-rich Nitinol compositions spanning from 53NiTi to 58NiTi (at.%) have been solutionized at 1050°C and aged at 400, 625, and 750°C for varying lengths of time to determine the effect of microstructure and subsequent phase decomposition on hardenability. The 57NiTi and 58NiTi solutionized alloys revealed coarse Ni<sub>3</sub>Ti<sub>2</sub> and Ni<sub>3</sub>Ti precipitates suggesting that this temperature was inadequate to fully solutionize these alloys. Higher temperature annealing was not practical due to uncertainty in the liquidus and solvus lines. Upon quenching after solutionizing, all the alloys consisted of nanoscale Ni<sub>4</sub>Ti<sub>3</sub> precipitates, with the 55NiTi, 56NiTi, and 57NiTi alloys having peak hardness values of  $649.4 \pm 4.5$ ,  $649.4 \pm 4.7$ , and  $634.4 \pm 5.4$  respectively, which are on par with tool steels. The hardness was attributed to the high volume fraction of Ni<sub>4</sub>Ti<sub>3</sub> precipitates that resulted in narrow B2 NiTi matrix channels and

yielding a microstructure-driven morphology that would enhance Orowan strengthening mechanisms.

Upon aging at 400°C, the 53NiTi and 54NiTi alloys exhibited a significant drop in hardness after a few hours, while the higher Ni alloys exhibited stable hardness up to at least 100 hours. Upon increasing Ni content to greater than 56NiTi and increasing the aging time and temperature, the Ni<sub>4</sub>Ti<sub>3</sub> phase decomposed to either Ni<sub>3</sub>Ti<sub>2</sub> and/or Ni<sub>3</sub>Ti phases with all precipitates coarsening, resulting in a subsequent loss in hardness. The decomposition morphology between the precipitates was characterized in a 57NiTi alloy aged 1000 hours at 400°C by serial sectioning showing that Ni<sub>4</sub>Ti<sub>3</sub> acts as a heterogeneous nucleate site and Ni-reservoir for direct globular Ni<sub>3</sub>Ti precipitates.

Through this study, the optimal composition and aging treatments have been determined in binary Ni-rich Nitinol. Optimal hardness was found between 55-56NiTi in the solutionized 1050°C, water quenched and 15 minutes of 400°C aging.

#### **4.6 References**

- [1] K. Otsuka, X. Ren, Prog.Mater. Sci. 50 (2005) 511.
- [2] C. DellaCorte, R.D. Noebe, M.K. Stanford, S.A. Padula, Resilient and Corrosion-Proof Rolling Element Bearings Made from Superelastic Ni-Ti Alloys for Aerospace Mechanism Applications, in: Y.R. Takeuchi, W.F. Mandler (Eds.), Rolling Element Bearings, ASTM International, West Conshohocken, PA, 2012, p. 143-166.
- [3] W.J. Buehler, F.E. Wang, Ocean Eng. 1 (1968) 105.
- [4] W.J. Buehler, "Intermetallic Compound Based Materials for Structural Applications," 7th NAVY Science Symposium: Solution to NAVY Problems Through Advanced Technology, Office of Naval Research, Arlington, VA, report number AD421708(64N15101), May 1963.

- [5] B.C. Hornbuckle, X.X. Yu, T.T. Sasaki, M.L. Weaver, R.D. Noebe, G.B. Thompson, Under submission to *Scripta Mater.* (Chapter 3 in dissertation).
- [6] P. Filip, K. Mazanec, *Scripta Mater.* 45 (2001) 701.
- [7] M. Nishida, C.M. Wayman, A. Chiba, *Metallography* 21 (1988) 275.
- [8] W. Tang, *Metall. Mat. Trans A.* 28 (1997) 537.
- [9] M. Nishida, C.M. Wayman, T. Honma, *Metall Trans.A.*, 17 (1986) 1505.
- [10] H.E. Karaca, I. Kaya, H. Tobe, B. Basaran, M. Nagasako, R. Kainuma, Y. Chumlyakov, *Mat. Sci. Eng.* 580 (2013) 66.
- [11] T.B. Massalski, H. Okamoto, P.R. Subramanian, L. Kacprzak, *Binary alloy phase diagrams*, second ed. ASM International, Materials Park, OH; 1990. p. 2874.
- [12] T. Saburi, S. Nenno, T. Fukuda, *J. Less-Common Met.* 125 (1986) 157.
- [13] R.R. Adharapurapu, F. Jiang, K.S. Vecchio, *Mat. Sci. Eng.A* 527 (2010) 1665.
- [14] G. Gottstein, *Physical Foundations of Materials Science.* Springer Science, 2004. pp. 272.
- [15] M.F.X Wanger and W. Windl, *Scripta Mater.* 60 (2009) 207.
- [16] W. Tirry, D. Schryvers, *Acta Mater.* 53 (2005) 1041.

## CHAPTER 5

### NEXT-GENERATION HIGH HARDNESS NICKEL-RICH NITINOL VIA HAFNIUM SOLUTE INDUCED PRECIPITATION<sup>4</sup>

#### **Abstract**

Very Ni-rich Nitinol alloys have recently been shown to have an anomalous rise in hardness, comparable to tool steels, when solutionized and quenched. Consequently, they have been identified as a bearing material. This hardness has been associated to the precipitation of  $\text{Ni}_4\text{Ti}_3$  precipitates that create narrow B2 matrix channels. In this work, a series of Ni-rich ternary alloys with dilute solute additions of Hf (54Ni-45Ti-1Hf, 55Ni-44Ti-1Hf, 54Ni-44Ti-2Hf, and 56Ni-40Ti-4Hf (at.%) ) have been investigated. Transmission electron microscopy confirmed a B2 NiTi matrix phase containing nanoscale  $\text{Ni}_4\text{Ti}_3$  platelets, H-phase precipitates, and R-phase. At aging times greater than 100 hours at 400°C, all ternary alloys showed a slight secondary increase in hardness, which was attributed to the H-phase precipitates filling these narrow B2 channels. In particular to the 4% Hf alloy, the hardness increased to a maximum value of  $679.3 \pm 2.8$  VHN, which was greater than all other binary or ternary alloys. Additionally the H-phase appeared to alter or delay the typical breakdown sequence of the metastable  $\text{Ni}_4\text{Ti}_3$  strengthening phase by removing the excess Ni needed for its decomposition. The collective results provide new material insights for creating a next-generation Nitinol based bearing alloy.

<sup>4</sup> A manuscript has been prepared for the work in this chapter for publication in Advanced Engineering Materials.

## 5.1 Introduction

NiTi binary alloys, commonly referred to as Nitinol, have received considerable research and commercial interest because of their shape memory and superelastic behaviors. These properties are derived from a thermoelastic martensitic transformation [1]. Of the Nitinol alloys, the equiatomic and Ti-rich variations have received considerable attention because of their shape memory behaviors at moderate transformation temperatures of ~70-100°C [2,3]. The Ni-rich Nitinol alloys, with the exception of body-temperature superelastic behavior, have been less studied because they exhibit a rapid decrease in their transformation temperature, well below 0°C, with increasing Ni-content [4]. However, a recent study has indicated that a very Ni-rich Nitinol alloy, 55NiTi (at.%), has a hardness comparable to that of tool steels [5]. Considering the high strength, moderate elastic modulus, and corrosion resistance of this alloy, it is considered an ideal candidate for bearing applications where resistance to shock loading and corrosion would be a benefit [6]. It was recognized as one of the top 100 R&D technology advancements in 2014. This binary alloy has been considered for use as bearings in the water recycling system for the International Space Station [7] with other applications being actively explored.

The hardening mechanism for this particular alloy has been attributed to a high volume fraction of nanoscale  $\text{Ni}_4\text{Ti}_3$  platelets that precipitate extremely rapidly upon water quenching from a B2 solutionized condition [8]. These precipitates create narrow B2 matrix channels that provide a microstructural-driven Orowan hardening mechanism [9]. In addition, these coherent precipitates also create significant strain within the microstructure providing a strain hardening contribution as well [10]. If the alloy is furnace cooled from the solution temperature, coarse  $\text{Ni}_4\text{Ti}_3$  precipitation occurs as well as decomposition to the more thermodynamically stable  $\text{Ni}_3\text{Ti}_2$  and  $\text{Ni}_3\text{Ti}$  structures. All of which results in a precipitous drop in hardness. Hence solutionizing in the B2 phase field is requisite for the rapid nanoscale  $\text{Ni}_4\text{Ti}_3$  precipitation that results in the seemingly anomalous rise in hardness in the as-quenched condition [8].

As the Ni-content increases, the temperature necessary to place the alloy in the single-phase B2 phase field also increases. Based on the phase diagram of Massalski *et al.*, a 55NiTi alloy would require a

minimum solutionizing temperature of  $\sim 1000^{\circ}\text{C}$  [11]. Clearly, the ability to retain the high hardness, while lowering the necessary solutionizing temperature would be advantageous for industrial scale-up and production of these alloys. For example, if the alloy is 54NiTi, the solvus temperature is  $\sim 925^{\circ}\text{C}$  but the equilibrium fraction of  $\text{Ni}_4\text{Ti}_3$  precipitates decreases. To offset the volume fraction loss of  $\text{Ni}_4\text{Ti}_3$ , solid solution strengthening could be used as one alternative that could offset the loss in precipitation strengthening. In addition, the ability to explore additional strengthening mechanisms even for the higher volume fraction of  $\text{Ni}_4\text{Ti}_3$  (high Ni content) alloys could result in further increases in hardness and lead to second generation bearing alloys.

In the present study, we investigate micro-alloying additions of 1 – 4 at. % Hf in Ni-rich Nitinol to determine the effects on microstructure and hardenability. It is generally assumed that Hf would reside in the Ti sublattice as both metals are group IVB transition metals for low concentrations, yet no definitive investigations have addressed this assumption. Suspected advantages of Hf include its slow diffusivity in Nitinol, which could reduce the kinetics of  $\text{Ni}_4\text{Ti}_3$  decomposition (i.e. the strengthening phase in Nitinol alloys) as well as provide an additional component to hardening through solid-solution strengthening due to its larger atomic size. Of the prior ternary Hf additions in Nitinol, the majority of these efforts have been at the macro-alloy levels ( $\geq 15$  at.%), which has shown the precipitation of more complex phases, such as the H-phase [12-14]. The primary objective of those studies was the influence of the secondary precipitate on the shape memory and/or superelastic effect in slightly Ni-rich alloys. Though these properties are important, the current work addresses how ternary (solute) additions influence the phase stability and its high hardness properties in an emerging family of structural alloys.

## 5.2 Experimental Methodology

The four ternary compositions studied were the following: 54Ni-45Ti-1Hf; 55Ni-44Ti-1Hf; 54Ni-44Ti-2Hf; and 56Ni-40Ti-4Hf (at.%). The 54Ni-45Ti-1Hf alloy was induction melted

and then hot isostatic pressed at  $\sim 900^{\circ}\text{C}$  under a pressure of 15 ksi for 2 hours. The 55Ni-44Ti-1Hf, 54Ni-44Ti-2Hf, and 56Ni-40Ti-4Hf (at.%) were arc melted and then homogenized at  $1050^{\circ}\text{C}$  for 24 hours in a vacuum furnace and furnace cooled. The as-processed material was then sectioned into several smaller samples and solution annealed at  $1050^{\circ}\text{C}$  for 10 hours followed by a water quench to ensure uniformity in the initial processing history for each alloy. The solution annealed samples were then aged at  $400^{\circ}\text{C}$  for various times with each followed by a water quench. During all solution annealing and aging treatments, the samples were placed in a tube furnace under a continuous flow of ultra-high purity Ar and wrapped in Ta foil to reduce the amount of oxidation.

The microstructure of each sample was characterized by transmission electron microscopy (TEM) in a FEI Tecnai G<sup>2</sup> F-20 Supertwin (S)TEM operated at 200 keV and atom probe tomography (APT) using a Cameca Instruments Local Electrode Atom Probe (LEAP) 3000XSi. The TEM foils were prepared by cutting out a 3mm diameter disc, grinding the disc to  $\leq 100\ \mu\text{m}$  followed by dimpling with a  $6\ \mu\text{m}$  diamond suspension. This leaves  $\sim 10\ \mu\text{m}$  of foil below the dimple depth, which was then Ar ion milled until electron perforations occurred in the dimple. The atom probe specimens were prepared using a lift out procedure in a FEI Quanta 3D dual electron – focus ion beam microscope as outlined in references [15,16]. The atom probe tips were set to a base temperature of 30 K and field evaporated at a constant evaporation rate of 0.5% using a 250 kHz laser pulse at 0.2 nJ. The data was reconstructed using the IVAS 3.6 software platform. Hardness was measured using a Buehler Model 1600-6100 microhardness tester equipped with a Vickers diamond-pyramid indenter. A 1 kg load and 15 second dwell time was utilized for each of the ten separate hardness measurements from which an average and standard deviation was determined.

### 5.3 Results and Discussion

The age hardening curves for the four ternary alloys are plotted in Figure 5.1(a). Additionally, the aging curves for 54NiTi, 55NiTi and 56NiTi [8,17] are also included for comparison to the binary alloys. The aging curves in Figure 5.1(a) clearly indicate that the hardness scales primarily with Ni content, with higher Ni-containing alloys having a higher hardness value. It has previously been reported [8], that the high hardness was associated with a high volume fraction of nanoscale Ni<sub>4</sub>Ti<sub>3</sub> platelets. Based on the Ni-Ti phase diagram [11,18], where NiTi and Ni<sub>4</sub>Ti<sub>3</sub> are line compounds, the estimated volume fraction of precipitate phase for a 55NiTi alloy was ~ 71%, which was confirmed by TEM analysis [8]. The precipitates created significant strain contrast in the bright field image, Figure 5.1(b) and revealed narrow, linear B2 matrix channels between the Ni<sub>4</sub>Ti<sub>3</sub> platelets in the High Angle Annular Dark Field (HAADF) micrographs, as exemplified in Figure 5.1(c) for the 54Ni-44Ti-2Hf ternary alloy. Note, the HAADF image is based on atomic number or Z contrast; hence the brighter phases are those with higher atomic number, Z, elements. In this case, the Ni<sub>4</sub>Ti<sub>3</sub> phase appears brighter than the equiatomic B2 NiTi matrix because it is more Ni-rich. Since B2 NiTi is softer than Ni<sub>4</sub>Ti<sub>3</sub> [8,19], deformation at moderate strains would likely be constrained to these matrix channels. The narrow and tightly spaced channel microstructure would provide a microstructural induced hardening effect by pinning dislocations at the precipitates and stretching the dislocation line length through the channel.

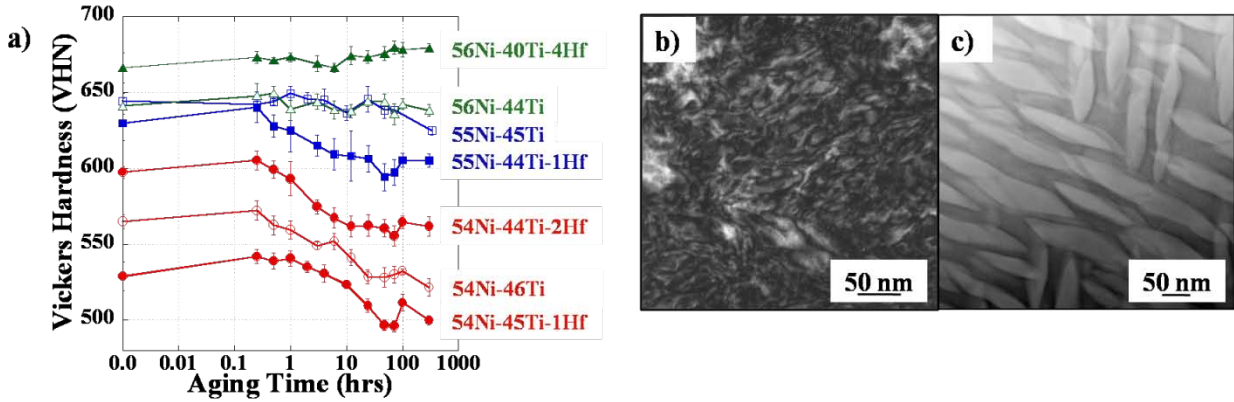


**Figure 5.1.** (a) 400°C aging curves for various Ni-rich binary and ternary Ni-Ti alloys; note the binary data is from [8, 17]. (b) Bright-field image and (c) STEM-HAADF image of the 54Ni-44Ti-2Hf solutionized/quenched microstructure. Note the significant strain contrast generated from the high volume fraction of  $\text{Ni}_4\text{Ti}_3$  precipitates in (b) and the nanoscale  $\text{Ni}_4\text{Ti}_3$  precipitates and narrow B2 matrix channels revealed in (c).

For a constant Ni-content, the Hf-containing alloys exhibited similar or superior hardness compared to the binary alloys. Assuming that Hf substitutes on the Ti sublattice, the 55Ni-44Ti-1Hf alloy would be expected to have a similar microstructure as the binary 55Ni-45Ti alloy. The TEM bright field and selected area diffraction images are shown in Figure 5.2(a)-(b) for the 55Ni-44Ti-1Hf alloy in the solution annealed and quenched condition. While very little detail can be resolved in the bright field micrograph due to high strain contrast, the diffraction pattern confirms the presence of the B2 and  $\text{Ni}_4\text{Ti}_3$  phases and is similar to what is observed in the comparable binary alloy [8]. Note that the  $\text{Ni}_4\text{Ti}_3$  reflections create the characteristic double reflection halo pattern around the fundamental  $\langle 110 \rangle$  B2 reflections. Occasionally, we noted in some diffraction patterns the R-phase, which is a martensite variation known to form in Ni-rich Nitinol [20]. This phase was only observed in samples in significantly overaged conditions and never in the solution annealed material. These reflections were seen as a single spot between the  $\text{Ni}_4\text{Ti}_3$  characteristic double reflection halo pattern around the primary  $\langle 110 \rangle$  B2 reflection noted

above. The other ternary alloys, in the solutionized condition, exhibited similar microstructures with equivalent phases.

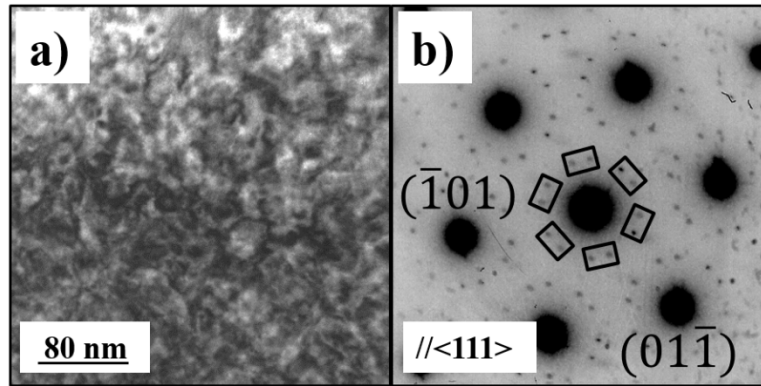


**Figure 5.2.** (a) Bright-field image and (b) SAED pattern from the  $\langle 111 \rangle$  zone axis of the 55Ni-44Ti-1Hf solutionized/quenched condition confirming the presence of the B2 and  $\text{Ni}_4\text{Ti}_3$  phases. The  $\text{Ni}_4\text{Ti}_3$  reflections are denoted by the rectangular boxes in Figure 5.2(b). Again note the significant strain contrast generated from the high volume fraction of  $\text{Ni}_4\text{Ti}_3$  precipitates in Figure 5.2(a).

With aging, the binary 55Ni-45Ti and 55Ni-44Ti-1Hf alloys had a near equivalent hardness after 15 minutes aging at 400°C. The slight increase in the 55Ni-44Ti-1Hf is attributed to the system having sufficient time to precipitate out the maximum  $\text{Ni}_4\text{Ti}_3$  volume fraction. Unlike the binary alloy, the Hf additions appear to slightly hinder the kinetics of  $\text{Ni}_4\text{Ti}_3$  precipitation upon quenching. Hf has been reported to diffuse slower than either the binary elements in Nitinol [21] and may have slightly reduced the volume fraction of  $\text{Ni}_4\text{Ti}_3$  that formed on quenching, but was recovered with aging. Nishida *et al.* has shown time-temperature-transformation curves for Ni-rich Nitinol that indicated tens of microseconds for  $\text{Ni}_4\text{Ti}_3$  precipitation [22], which is difficult, if not impossible, to suppress upon quickly removing samples from a furnace and water quenching.

The 54Ni-45Ti-1Hf and 54Ni-44Ti-2Hf alloys exhibited lower initial hardness than the 55 or 56 NiTi alloys upon solutionizing and quenching. But similar to the 55Ni-44Ti-1Hf alloy, a

modest increase to a peak hardness occurred after 15 minutes of aging at 400°C and is again attributed to the system reaching the maximum  $\text{Ni}_4\text{Ti}_3$  precipitate volume fraction. Using the simple lever rule approximation described above and assuming Hf substitutes for Ti, alloys containing 54 at.% Ni would result in ~57 vol.%  $\text{Ni}_4\text{Ti}_3$  phase. This is approximately a 14 % volume reduction in  $\text{Ni}_4\text{Ti}_3$  phase from the 55Ni-based to 54Ni-based alloys. Clearly, by reducing the fraction of the strengthening phase, i.e.  $\text{Ni}_4\text{Ti}_3$ , the hardness decreased. But there was some benefit of the Hf addition, compared to binary alloys with similar Ni content when the Hf content was greater than or equal to 2 at.%. For example, the 54Ni-44Ti-2Hf alloy was 40 to 60 VHN harder in the solution annealed condition and after short aging times at 400°C compared to the binary 54Ni-46Ti alloy.

The highest hardness was observed in the 56Ni-40Ti-4Hf alloy in both the solution treated condition and after aging at 400°C for up to 300 hrs, reaching  $679.3 \pm 2.8$  VHN. Based on the dependence of  $\text{Ni}_4\text{Ti}_3$  volume fraction with Ni content, one could initially assume that the higher hardness is associated completely with an increase in  $\text{Ni}_4\text{Ti}_3$  volume fraction. Based on the prior lever rule approximation, the  $\text{Ni}_4\text{Ti}_3$  content would be ~86 % by volume. However, the binary 56NiTi alloy has an approximate hardness value of that of the 55NiTi, suggesting a possible hardness limit as a function of composition (volume fraction) in the binary alloys. In fact, alloys with even higher Ni content actually exhibited a slight decrease in hardness compared to the 55-56NiTi alloys [17]. Hence, the increase in hardness for the 56Ni-40Ti-4Hf alloy, which is higher than the comparable 56NiTi binary, is attributed to solid solution strengthening by Hf, similar to the increase in hardness noted for the 54Ni-44Ti-2Hf alloy compared to the corresponding binary 54NiTi, for Figure 5.1(a).

With extended aging, all of the ternary alloys evolved microstructurally including the onset of H-phase precipitation [12-14]. Figure 5.3(a) is the bright field image for the 54Ni-45Ti-1Hf alloy after 400°C/24 hours aging. The precipitate morphology can be observed after aging with the HAADF image, Figure 5.3(b). The diffraction pattern, Figure 5.3(c), indicated the presence  $\text{Ni}_4\text{Ti}_3$  reflections (the double halo spots) around the (110) type of B2 reflections. An additional single spot reflection between these double spot reflections has been indexed to either the H-phase or R-phase indicated by the black arrows. By titling to the [001] zone of B2, reflections associated only with the H-phase (not R-phase) can be clearly discerned and indicated by the black arrows again, Figure 5.3(d). The other ternary alloys, after extended aging, showed equivalent diffraction characteristics.

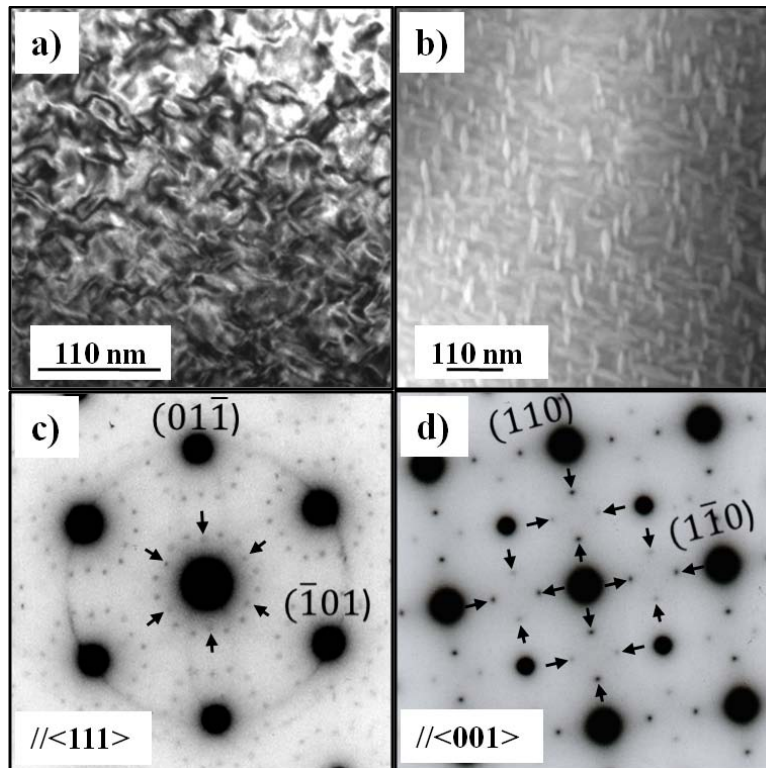


**Figure 5.3.** 54Ni-45Ti-1Hf alloy aged at 400°C/24 hours: (a) Bright-field image, (b) STEM-HAADF image, (c) SAED taken //<111>, and (d) SAED taken //<001>. The presence of the B2,  $\text{Ni}_4\text{Ti}_3$  precipitates, and H-phase precipitates (denoted by arrows), were all confirmed.

The ability to precipitate the H-phase at low Hf solute concentrations was surprising, since it has only previously been reported in macro-alloyed ( $\geq 15\text{Hf at.}\%$ ) systems [12,13]. The long aging time for formation of H-phase (as compared to the solutionized and quenched precipitation of  $\text{Ni}_4\text{Ti}_3$ ) is associated with the slower diffusion of Hf than either Ni or Ti in Nitinol [21], the low solute levels, and aging temperature, which significantly reduces the driving force for precipitation. The precipitation of the H-phase also appeared to hinder or prevent the typical decomposition sequence of  $\text{Ni}_4\text{Ti}_3$  to  $\text{Ni}_3\text{Ti}_2$  (metastable) and  $\text{Ni}_3\text{Ti}$  (stable) phases [1,8, 22], as neither of these phases were observed for the aging times and temperatures studied. This is attributed to the H-phase depleting the available Ni required for the higher Ni-content phases to form. This suggests that co-precipitation may provide a means for stabilizing  $\text{Ni}_4\text{Ti}_3$ .

The later precipitation of the H-phase has an effect on the secondary hardening behavior of the ternary alloys. At approximately 100 hours, the 54Ni-45Ti-1Hf, 55Ni-44Ti-1Hf, and 54Ni-44Ti-2Hf alloys revealed a modest secondary hardness peak, Figure 5.1(a). Moreover, the steady hardness for the 56Ni-40Ti-4Hf alloy also began to show the onset of a rise in hardness around the same aging time. The STEM-HAADF images and diffraction patterns for the solution annealed and 300 hour aged conditions of the 56Ni-40Ti-4Hf alloy are shown in Figure 5.4. The diffraction patterns confirm only the presence of B2 and  $\text{Ni}_4\text{Ti}_3$  for the solutionized condition, Figure 5.4(b-c), while these phases as well as the H-phase were confirmed in the 300 hours aged specimen's patterns, Figure 5.4(e-f). The STEM-HAADF image of the solutionized condition, Figure 5.4(a), shows extremely narrow channels of B2 matrix between the  $\text{Ni}_4\text{Ti}_3$  precipitates after solutionizing and quenching. Recall that these channels are created from the as-quenched microstructure by the rapid precipitation of  $\text{Ni}_4\text{Ti}_3$ , Figure 5.1(c). The HAADF image corresponding to the 300 hours aged specimen, Figure 5.4 (d), reveals the H-phase precipitates

forming within the narrow channel of B2 matrix. To further strengthen the assertion H-phase was forming in the narrow B2 channels, a dark field image, Figure 5.4(g) was taken using the H-phase reflection circled with the black dotted line in Figure 5.4(f). This image confirmed H-phase formed in narrow B2 channels surrounding the  $\text{Ni}_4\text{Ti}_3$  precipitates. A consequence of secondary H-phase precipitation is a strengthening of the softer B2 channels and an uptick in hardness. But for low Hf levels (1-2 at.%), the precipitation of a low volume fraction of H-phase is not enough to overcome the larger loss in hardness with aging that occurs due to coarsening of the  $\text{Ni}_4\text{Ti}_3$  platelets prior to precipitation of the H-phase. Upon continued aging, after the secondary hardening peak, the  $\text{Ni}_4\text{Ti}_3$  platelets continue to coarsen and the hardness once again begins to decrease in these alloys.

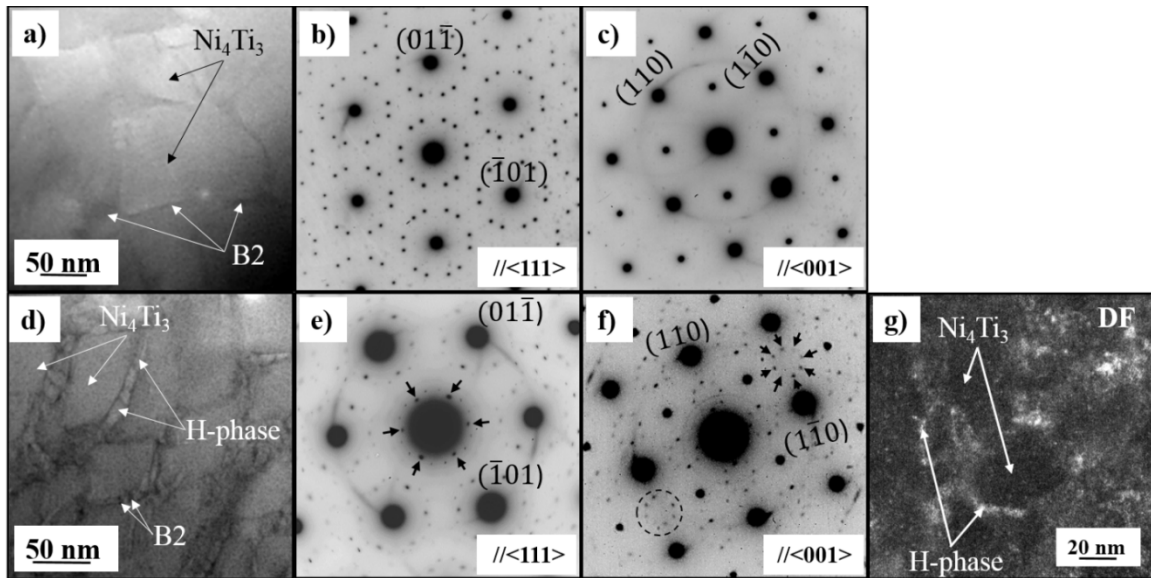


**Figure 5.4.** 56Ni-40Ti-4Hf alloy solutionized and quenched condition: (a) STEM-HAADF image; (b) SAED taken  $//\langle 111 \rangle$ ; (c) SAED taken  $//\langle 001 \rangle$ . The presence of the B2 and  $\text{Ni}_4\text{Ti}_3$  precipitates were confirmed. 56Ni-40Ti-4Hf aged at 400°C/300hrs: (d) STEM-HAADF image; Note the formation of H-phase filling the narrow channels of B2 between the as-quenched  $\text{Ni}_4\text{Ti}_3$  microstructure. (e) SAED taken  $//\langle 111 \rangle$ ; (f) SAED taken  $//\langle 001 \rangle$ ; and (g) Dark field image generated using the H-phase reflection circled with the black dotted line in (f). The presence of the B2,  $\text{Ni}_4\text{Ti}_3$  precipitates, and H-phase precipitates (denoted by arrows) were all confirmed.

The exception is the 56Ni-40Ti-4Hf alloy. In this alloy, the B2 channels are nearly filled with the H-phase, Figure 5.4(d), because of the smaller initial channel spacing, Figure 5.4(a), due to the higher Ni-content and because of the higher Hf content. Thus, there are only very narrow strips (2-4 nm) of B2 left in the alloy after aging, indicated by the dark regions in this HAADF image. The SAED patterns, Figure 5.4(e-f), confirmed the presence of all three phases (B2, Ni<sub>4</sub>Ti<sub>3</sub>, and H-phase). It is reasonable to assume that as the Hf content increased, the volume fraction of H-phase would also increase, though the complete phase equilibrium in the Ni-Ti-Hf system has yet to be determined. The addition of the higher Hf content also appeared to reduce the diffusivity (or coarsening) of the Ni<sub>4</sub>Ti<sub>3</sub> platelets evident by the lack of a classical parabolic hardening curve observed in the lower Hf containing alloys or even a decrease in hardness at longer aging times as observed for the higher Ni-containing binary alloys. Hf is known to be a slower diffusing species relative to Ti or Ni [21]. The formation of the H-phase, which is Hf enriched relative to the matrix and a complex face-centered orthorhombic structure with 192 atoms in the unit cell [12], would be a difficult structure to diffuse through as compared to the simple 2 atom basis of B2. The precipitation of the H-phase would also alter the availability of excess Ni from which the Ni<sub>4</sub>Ti<sub>3</sub> phase could coarsen or decompose to the Ni-rich Ni<sub>3</sub>Ti<sub>2</sub> or Ni<sub>3</sub>Ti phases [22]. All of which may explain the sluggish coarsening behavior of the Ni<sub>4</sub>Ti<sub>3</sub> platelets in this alloy.

The solutionized and quenched version of the 54Ni-45Ti-1Hf alloy is shown in Figure 5.5(a-c). In this condition, only the B2 and Ni<sub>4</sub>Ti<sub>3</sub> phases are present. The matrix appears to be slightly enriched in Hf, which is attributed to Ni and Ti being able to diffuse faster and chemically order into Ni<sub>4</sub>Ti<sub>3</sub> (confirming that Hf is the slower diffusing species [21]). The peak aged condition's (15 minutes) Hf atom map, proximity histogram, and diffraction pattern, are

shown in Figure 5.5(d-f), respectively. Equivalent to the solutionized and quenched specimen, the same phases are present (no H-phase), but the Hf content appears to be homogenizing between the B2 and  $\text{Ni}_4\text{Ti}_3$  phases. The Hf in solution would act as a strengthening addition and is in agreement to the rise in hardness for this alloy as combined to the binary. The 72 hours aged condition's Hf atom map, 1D compositional profile, and diffraction pattern are shown in Figure 5.5(g-i) respectively. The Hf atom map, Figure 5.5(g), clearly shows Hf partitioning to a precipitate phase. The diffraction pattern, Figure 5.5(i), confirmed the presence of the B2,  $\text{Ni}_4\text{Ti}_3$ , and H- phases. While the atom probe provides chemical analysis, it unfortunately does not provide diffraction information, so the exact identity of the precipitate within the atom probe data cannot be obtained.

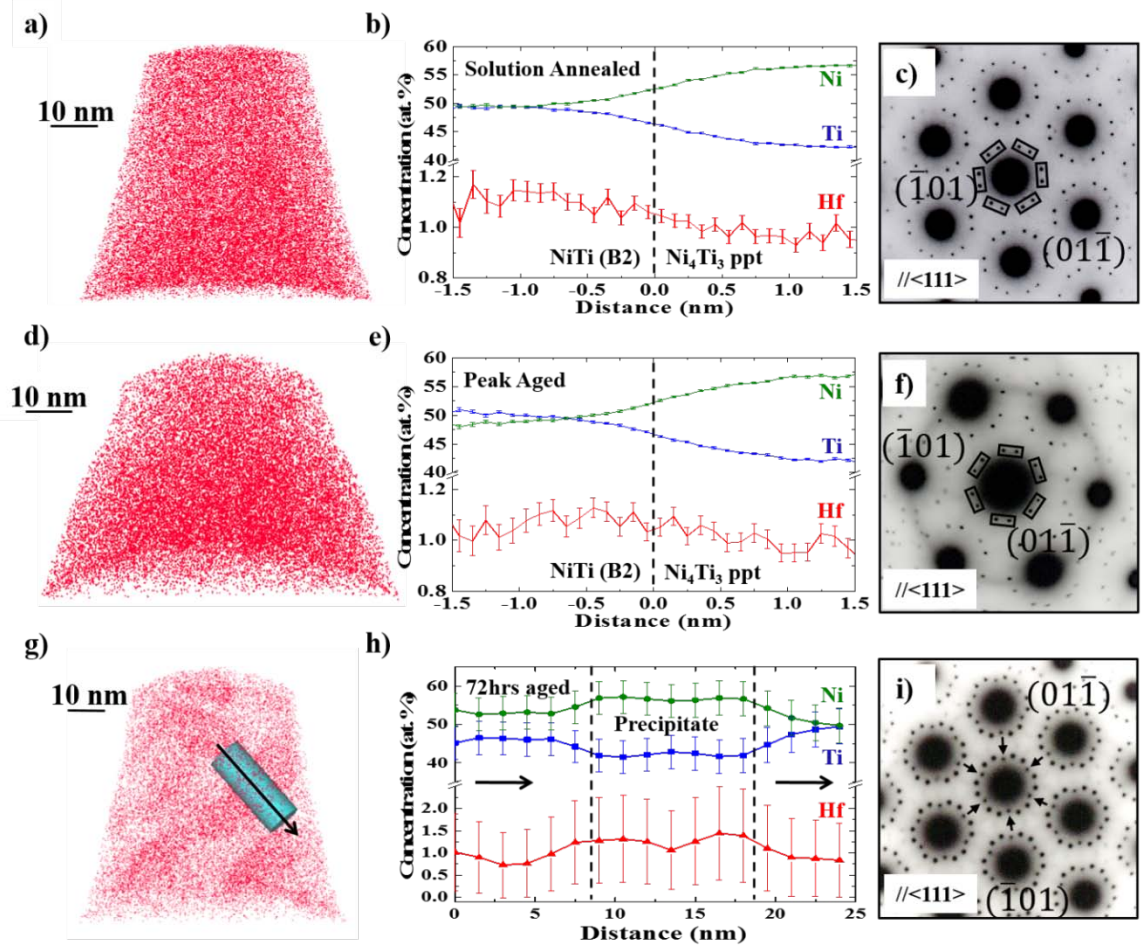


**Figure 5.5.** 54Ni-45Ti-1Hf alloy: Solutionized and quenched condition (a) Atom map of Hf showing no clear Hf partitioning, (b) Proximity histogram generated from a 52.48% Ni isoconcentration surface showing slight enrichment of Hf in the matrix, (c) SAED taken  $//\langle 111 \rangle$  confirming B2 and  $\text{Ni}_4\text{Ti}_3$  precipitates (denoted by rectangular boxes). 400°C/15 minutes aged condition: (d) Atom map of Hf showing no clear Hf partitioning, (e) Proximity histogram generated from a 52.25% Ni isoconcentration surface showing Hf homogenizing between the two phases, (f) SAED taken  $//\langle 111 \rangle$  confirming B2 and  $\text{Ni}_4\text{Ti}_3$  precipitates (denoted by rectangular boxes). 400°C/72 hours aging: (g) Atom map of Hf showing Hf partitioning to the  $\text{Ni}_4\text{Ti}_3$  phase with cylinder displayed used to create 1D concentration profile, (h) 1D concentration profile indicating  $\text{Ni}_4\text{Ti}_3$  phase is enriched in Hf and Ni compared to the matrix, (i) SAED taken  $//\langle 111 \rangle$  confirming B2,  $\text{Ni}_4\text{Ti}_3$  precipitates, and H-phase (denoted by arrows), but not observed in the limited volume of the APT analysis.

## 5.4 Conclusion

A series of micro-alloyed Hf additions were made to very Ni-rich Nitinol alloys and compared to similar binary versions. All the samples were solutionized at 1050°C for 10 hours and water quenched with subsequent aging at 400°C for various times. The hardness, in general, increased with Ni content, which seems to be the major factor in controlling the volume fraction of Ni<sub>4</sub>Ti<sub>3</sub> precipitate phase, which occurs rapidly upon quenching. The 54Ni-45Ti-1Hf, 55Ni-44Ti-1Hf, and 54Ni-44Ti-2Hf alloys all exhibited classic age hardening behavior with a peak after very short aging times (between 15 min and 1hr). The loss in hardness with aging is attributed to coarsening of the Ni<sub>4</sub>Ti<sub>3</sub> precipitates. It was noted that the Hf-containing alloys did not decompose to the typical Ni<sub>3</sub>Ti<sub>2</sub> or Ni<sub>3</sub>Ti phases from the metastable Ni<sub>4</sub>Ti<sub>3</sub> but rather the co-precipitation of the H-phase occurred with extended aging times. The H-phase likely biased the Ni content in the alloy needed for Ni<sub>4</sub>Ti<sub>3</sub> to decompose, though extended aging times (possibly out to several thousand hours) are needed to truly determine the phase equilibrium behavior.

At approximately 100 hours, a modest secondary hardness peak was noted in the Hf-containing alloys and was attributed to the precipitation of H-phase, as this secondary peak was not observed in any of the binary alloys. This secondary peak was significantly lower in hardness than either the solutionized or peak aged conditions. At these low Hf levels, precipitation of H-phase could not compensate for the loss in hardening due to the coarsening of the Ni<sub>4</sub>Ti<sub>3</sub> phase. The 54Ni-44Ti-2Hf alloy also appeared to show benefits in hardness due to solid solution strengthening.

Of all the alloys investigated, the 56Ni-40Ti-4Hf composition showed the highest hardness and was able to retain as well as increase its hardness with aging up to 300 hours (679.3± 2.8VHN), the longest time investigated. This hardness was associated with solid solution

strengthening as well as H-phase precipitation. The H-phase precipitates occupied a significant volume fraction of the softer B2 matrix channels furthering the hardening of the alloy. The lack of softening over time was attributed to the slow Hf diffusion kinetics and complex precipitate phase structures that hinder atomic mobility. These results demonstrate that next-generation high hardness very Ni-rich Nitinol alloys can be processed with tunable microstructures, and thus variable mechanical attributes through micro-alloy additions.

Finally, this work has demonstrated that Hf, in very Ni-rich Nitinol alloys does not necessarily stay in solid solution even for dilute concentrations, but instead precipitates out as H-phase. Previously H-phase has been observed in slightly Ni-rich alloys at concentrations of  $\geq 15$  at.% Hf, but has never been reported in such dilute Hf-containing alloys. This suggests that much more work is still required in identifying the compositional stability and phase relationships in the Ni-Ti-Hf system.

## 5.5 References

- [1] K. Otsuka, X. Ren, *Prog.Mater. Sci.* 50 (2005) 511.
- [2] J.E. Hanlon, S.R. Butler, R.J. Wasilewski, *Trans. Metall. Soc. AIME*, 239 (1967) 1323.
- [3] I.I. Kornilov, Y.Y. Kachur, O.K. Belousov, *Phys. Met. Metall.* 32 (1971) 420.
- [4] W. Tang: *Metall. Mater. Trans. A*, 28 (1997) 537.
- [5] C. DellaCorte, R.D. Noebe, M.K. Stanford, S.A. Padula, Resilient and Corrosion-Proof Rolling Element Bearings Made from Superelastic Ni-Ti Alloys for Aerospace Mechanism Applications, in: Y.R. Takeuchi, W.F. Mandler (Eds.), *Rolling Element Bearings*, ASTM International, West Conshohocken, PA, 2012, p. 143-166.
- [6] T.L. Oberle, "Properties Influencing Wear of Metals", *J. Metals*, June 1951.

- [7] C. DellaCorte, W.A Wozniak, Design and Manufacturing Considerations for Shockproof and Corrosion-Immune Superelastic Nickel-Titanium Bearings for a Space Station Application, NASA/TM 2012-216015 (May 2012).
- [8] B.C. Hornbuckle, X.X. Yu, T.T. Sasaki, M.L. Weaver, R.D. Noebe, G.B. Thompson, Under submission to Scripta Materialia (2014) (Chapter 3 in dissertation).
- [9] G. Gottstein, Physical Foundations of Materials Science. Springer Science, 2004.pp. 272.
- [10] W. Tirry, D. Schryvers, Acta Mater. 53 (2005) 1041.
- [11] T.B. Massalski, H. Okamoto, P.R. Subramanian, L. Kacprzak, Binary alloy phase diagrams, second ed. ASM International, Materials Park, OH; 1990. p. 2874.
- [12] F. Yang, D.R. Coughlin, P.J. Phillips, L. Yang, A.Devaraj, L. Kovarik, R.D. Noebe, M.J. Mills, Acta Mater. 61 (2013) 3335.
- [13] X.D. Han, R. Wang, Z. Zhang, D.Z. Yang, Acta Mater. 46 (1998) 273.
- [14] R. Santamarta, J. Pons, A. Evirgen, R. Arroyave, I. Karaman, H.E. Karaca, R.D. Noebe, Acta Mater. 61 (2013) 6191.
- [15] K. Thompson, D. Lawrence, D.J. Larson, J.D. Olson, T.F. Kelly, B. Gorman, Ultramicroscopy 107 (2007) 131.
- [16] L.A. Giannuzzi, Microsc. Microanal.12 (2006) 1260.
- [17] B.C. Hornbuckle, R.D. Noebe, R. Martens, G.B. Thompson, In preparation for submission to Journal of Alloys and Compounds (Chapter 4 in dissertation).
- [18] J. Zhang, PhD thesis, University of Tsukuba, 2000.
- [19] M.F.X Wanger and W. Windl, Scripta Mater. 60 (2009) 207.
- [20] S. Miyazaki, K. Otsuka, Metall. Trans A. 17 (1986) 53.
- [21] X.L. Meng, W. Cai, Y.F. Zheng, L.C. Zhao, Mat. Sci. Eng. A, 438-440 (2006) 666.
- [22] M. Nishida, C.M. Wayman, T. Honma, Metall. Trans. A, 17 (1986) 1505.

## CHAPTER 6

### CONCLUSIONS AND FUTURE WORK

In this work, the phase stability and mechanical attributes in Ni-rich Nitinol with and without Hf additions were investigated through an array of microanalysis techniques. The work had two distinct areas of interest: (1) establishing the structure-properties relationship for a slightly Ni-rich ternary shape memory alloy with macro-additions of Hf for use as solid-state actuators and (2) determining the primary strengthening mechanisms and its compositional limit in very Ni-rich alloys with and without solute additions of Hf for bearing applications.

In chapter 2, a Ni-29.7Ti-20Hf (at.%) alloy had its transformation temperature and load-bias thermomechanical behavior correlated to its microstructure as a function of aging times at 550°C. The alloy was found to have short range ordering in the solution annealed condition and 0.3 hrs aged condition that yielded a transformation temperature  $< 100^{\circ}\text{C}$ ; however the transformation temperature was not consistent with thermal cycling. Once the H-phase precipitate formed after 3 hours of aging, the transformation temperature was still greater than 100°C and stabilized. Correspondingly the load-bias response was nearly vertical, dimensional stability was excellent due to negligible retained strain, and a narrow temperature hysteresis. With aging to 30 hours, the shape memory response slightly degraded indicating 3 hours was the optimal aging condition; despite the H-phase's number density and composition remaining within the error for both conditions.

A 55NiTi (at.%) alloy, known to possess a hardness on par with tool steels when properly aged, had its primary strengthening mechanism determined in chapter 3. After solution annealing and quenching the alloy, its hardness was  $644 \pm 5.1$  VHN and remained steady until  $\sim 100$  hours aging at  $400^\circ\text{C}$ . TEM revealed the microstructure to be composed of two phases: the B2 NiTi matrix and metastable  $\text{Ni}_4\text{Ti}_3$ . The volume fraction of  $\text{Ni}_4\text{Ti}_3$  was found to be  $\sim 69\%$  matching nicely to a lever rule calculation for an alloy of this composition. Additionally, GSFE for each phase was calculated, and it was found  $\text{Ni}_4\text{Ti}_3$  required nearly twice the energy to slip compared to the B2 matrix phase. These GSFE values plus the microstructure of narrow B2 channels between the much harder  $\text{Ni}_4\text{Ti}_3$  explained the high hardness. The retained hardness was found to be due to the slow kinetics at  $400^\circ\text{C}$  preventing the coarsening/decomposition of  $\text{Ni}_4\text{Ti}_3$  that occurred in a sample aged at  $750^\circ\text{C}$ .

The work in chapter 4 built off the work in chapter 4 by determining if the  $\text{Ni}_4\text{Ti}_3$  strengthening mechanism had a compositional limit by characterizing a series of binary compositions from 53NiTi to 58NiTi (at.%). It was found the 56NiTi alloy had a near equivalent aging behavior and hardness as the 55NiTi alloy, while the lower Ni content alloys displayed classic, parabolic aging curve as their lower volume fraction of  $\text{Ni}_4\text{Ti}_3$  coarsened. The high Ni content alloy appeared to not have been solutionized at  $1050^\circ\text{C}$  due to the presence of coarse  $\text{Ni}_3\text{Ti}$ , but a higher temperature was not possible due to the solid-liquidus line. Additionally, the alloys hardness and microstructure were observed at  $625^\circ\text{C}$  and  $750^\circ\text{C}$  to observe the precipitation sequence in these lesser studied, very Ni-rich compositions. It has found  $\text{Ni}_4\text{Ti}_3$  quickly decomposed at these higher temperatures and acts as a Ni reservoir for  $\text{Ni}_3\text{Ti}$  during its nucleation and growth.

Finally, chapter 5 was a second generation study of these possible bearing alloys with Ni-rich composition containing solute additions of Hf. The lower Hf containing alloys (1-2 at.% Hf) displayed typical overaging behavior due to the coarsening of their primary strengthening mechanism. Interestingly with extended aging H-phase co-precipitated rather than the formation of  $\text{Ni}_3\text{Ti}_2$  and/or  $\text{Ni}_3\text{Ti}$  seen in Ni-rich binary alloys. This composition has substantially less Hf than any other composition currently reported to have produced H-phase. Despite the lower Hf-containing alloys appearing less promising as bearing alloys, the highest Hf containing alloy produced tremendous results. Its hardness was greater than the original 55NiTi alloy after solution annealing; furthermore its hardness continued steadily climbing out to 300 hours. The microstructure responsible for this extreme hardness after 300 hours was again a high volume fraction of  $\text{Ni}_4\text{Ti}_3$  encased in narrow channels of B2, plus H-phase formed in the narrow B2 channels. The H-phase precipitation essentially eliminated the B2 matrix phase, which is the phase where slip is most likely to occur, and replaced it with a harder, intermetallic alternative.

With regard to future work, perform precession electron diffraction on the Ni-29.7Ti-20Hf (at.%) alloy to more quantitatively examine the strain fields as they evolve from the solution annealed condition through aging and formation of the H-phase precipitate. Then apply this knowledge to a study of strain as a function of Hf content to determine if there is a minimum Hf requirement to ascertain the required strain fields yielding the outstanding shape memory properties noted in the 20% Hf alloy. Since the transformation temperature continued to increase in the 300 hours aged specimen, perform an extend aging at 550°C to observe the possible decomposition sequence for the H-phase, and its effect on the SMA properties. For the ternary solute additions, continue aging of the 4% Hf alloy to monitor its hardness and microstructure. Finally, perform a compositional study by lowering Ni content and raising Hf in the 56Ni-40Ti-

4Hf (at.%) alloy to try and lower the required solution annealing temperature, while maintaining the incredible hardness.

## REFERENCES

- [1] T.W. Duerig, K.N. Melton, D. Stockel, C.M. Wayman (eds.), *Engineering Aspects of Shape Memory Alloys*, Butterworth-Heinemann, London, 1990.
- [2] W. Tang, *Metallurgical and Materials Transaction A* 27 (1997) 537.
- [3] L. Kovarik, F. Yang, A. Garg, D. Diercks, M. Kaufman, R.D. Noebe, and M.J. Mills, *Acta Materialia* 58 (2010) 4660.
- [4] T.T. Sasaki, B.C. Hornbuckle, R.D. Noebe, G.S. Bigelow, M.L. Weaver, and G.B. Thompson, *Metallurgical and Materials Transaction A* 44 (2013) 1388.
- [5] F. Yang, D.R. Coughlin, P.J. Phillips, L. Yang, A. Devaraj, L. Kovarik, R.D. Noebe, and M.J. Mills, *Acta Materialia* 61 (2013) 3335.
- [6] R. Santamarta, R. Arroyave, J. Pons, A. Evirgen, I. Karaman, H.E. Karaca, and R.D. Noebe, *Acta Materialia* 61 (2013) 6191.
- [7] N. Morgan: Eng.D.Dissertation, Cranfield University, Oxfordshire, United Kingdom, 1999.
- [8] G.S. Bigelow, A. Garg, S.A. Padula II, D.J. Gaydos, and R.D. Noebe, *Scripta Materialia* 64 (2011) 725.
- [9] W.J. Buehler and F.E. Wang, *Ocean Engineering* 1 (1968) 105.
- [10] L.C. Chang and T.A. Read, *Transactions of the American Institute of Mining, Metallurgical, and Petroleum Engineers* 189 (1951) 47.
- [11] M.W. Burkart and T.A. Read, *Transactions of the American Institute of Mining, Metallurgical, and Petroleum Engineers* 197 (1953) 1516.
- [12] Z.S. Basinski and J.W. Christian, *Acta Metallurgica* 2 (1954)101.
- [13] W.J. Buehler, J.V. Gilfrich, R.C. Wiley, *Journal of Applied Physics*, 34 (1963) 1475.
- [14] G. Bigelow, "Effects of Palladium Content, Quaternary Alloying, and Thermomechanical Processing on the Behavior of Ni-Ti-Pd Shape Memory Alloys for Actuator Applications," NASA/TM 2008-214702 (July 2008).

- [15] K. Otsuka and X. Ren, *Progress in Materials Science* 50 (2005) 511.
- [16] K. Otsuka, T. Sawamura, K. Shimizu, *Physica Status Solidi (a)* 5 (1971) 457.
- [17] R.F. Hehemann and G.D. Sandrock, *Scripta Metallurgica* 5 (1971) 801.
- [18] G.M. Michal and R. Sinclair, *Acta Crystallographica B* 37 (1981) 1803.
- [19] W. Buhner, R. Gotthardt, A. Kulik, O. Mercier, F. Staub, *Journal of Physics F* 13 (1983) L77.
- [20] Y. Kudoh, M. Tokonami, S. Miyazaki, K. Otsuka, *Acta Metallurgica* 33 (1985) 2049.
- [21] Y. Shugo, F. Hasegawa, T. Honma, *Bull Research Institute of Mineral Dressing and Metallurgy, Tohoku University* 37 (1981) 79 [in Japanese].
- [22] T. Tadaki and C. Wayman, *Metallography* 15 (1982) 247.
- [23] P.L. Potapov, A.V Shelyakov, D. Schryvers, *Scripta Materialia* 44 (2001) 1.
- [24] T.Y. Nam, T. Saburi, Y. Nakata, K. Shimizu. *Materials Transactions The Japanese Institute of Metals* 31 (1990) 1050.
- [25] M.B. Salamon, M.E. Meichle, C.M. Wayman, *Physical Review B* 31 (1985) 7306.
- [26] S. Miyazaki, S. Kimura, K. Otsuka, *Philosophical Magazine A* 57 (1988) 467.
- [27] S. Vatanayon, R.F. Hehemann. In: (ed.) J. Perkins, *Shape Memory Effects in Alloys*. New York: Plenum Press 1975 p. 115.
- [28] E. Goo, R. Sinclair, *Acta Metallurgica* 33 (1985) 1717.
- [29] T. Ohba, Y. Emura, K. Otsuka, *Materials Transactions of the Japanese Institute of Metals* 33 (1992) 29.
- [30] T. Hara, T. Ohba, E. Okunishi, K. Otsuka, *Materials Transactions of the Japanese Institute of Metals* 38 (1997) 11.
- [31] D. Schryvers, P.L Potapov, *Materials Transactions* 43 (2002) 774.
- [32] J. Jansen, D. Tang, H.W. Zandbergen, H. Schenk, *Acta Crystallographica A* 54 (1998) 91.
- [33] H. Sitepu, *Textures and Microstructures* 35 (2003) 185.

- [34] S. Miyazaki and K. Otsuka, *Metallurgical and Materials Transaction A* 17 (1986) 53.
- [35] M.C. Carroll, C. Somsen, G. Eggeler, *Scripta Materialia*. 50 (2004) 187.
- [36] J. Michutta, C. Somsen, A. Yawny, A. Dlouhy, G. Eggeler, *Acta Materialia*. 54 (2006) 3525.
- [37] J. Khalil Allafi, *Acta Materialia*. 50 (2002) 793.
- [38] T.B. Massalski, H. Okamoto, P.R. Subramanian, L. Kacprzak (ed.), *Binary alloy phase diagrams*, 2nd edition, vol. 3. Materials Park, OH: ASM International; 1990. p. 2874.
- [39] J. Zhang, PhD thesis, University of Tsukuba, 2000.
- [40] M.H. Mueller and H.W. Knott, *Transactions of the American Institute of Mining, Metallurgical, and Petroleum Engineers* 227 (1963) 674.
- [41] M. Nishida, C.M. Wayman, T. Honma, *Metallurgical and Materials Transactions A* 17 (1986) 1505.
- [42] T. Tadaki, Y. Nakata, K. Shimizu, and K. Otsuka, *Materials Transactions of the Japan Institute of Metals* 27 (1986) 731.
- [43] T Saburi, S Nenno, and T Fukuda, *Journal of Less-Common Metals* 125 (1986) 157.
- [44] T. Hara, T. Ohba, K. Otsuka, M. Nishida, *Materials Transactions of the Japan Institute of Metals* 38 (1997) 277.
- [45] A. Taylor and R.W. Floyd, *Acta Crystallographica*, 3(1950) 285.
- [46] R.J. Wasilewski, S.R. Butler, J.E. Hanlon, *The Metal Science Journal* 1 (1967) 104.
- [47] J.E. Hanlon, S.R. Butler, and R.J. Wasilewski, *Transactions of the American Institute of Mining, Metallurgical, and Petroleum Engineers* 239 (1967) 1323.
- [48] I.I. Kornilov, Ye V. Kachur, O.K. Belousov, *Fizika Metallov I Metallovedenie* 32 (1971) 420.
- [49] R.J. Wasilewski, S.R. Butler, J.E. Hanlon, D. Worden, *Metallurgical and Materials Transactions* 2 (1971) 229.
- [50] J.F. Smith, Q. Jiang, R. Luck, B. Predel *Material Science and Engineering A* 149 (1991) 111.
- [51] K.N. Melton and O. Mercier, *Acta Metallurgica* 29 (1981) 393.

- [52] S. Miyazaki, K. Otsuka, Y. Suzuki, *Scripta Metallurgica* 15(1981) 287.
- [53] X. Ren and K. Otsuka, *Material Science Forum* 327 (2000) 429.
- [54] X. Ren, K. Taniwaki, K. Otsuka, T. Suzuki T, K. Tanaki, Y.I. Chumlyakov, and T. Ueiki, *Philosophical Magazine A* 75 (1999) 31.
- [55] X. Ren and K. Otsuka, *Scripta Materialia* 38 (1998) 1669.
- [56] T. Suzuki and U. Shigeaki, (eds.) H. Kimura and O. Izumi, *Proceedings of the 4<sup>th</sup> International Conference on Titanium, The Metallurgical Society of AIME.* (1980) pp. 1255–1263
- [57] NASA Glenn Research Center, High-Temperature Shape Memory Alloy Group, unpublished research, 2004.
- [58] Y. Nakata, T. Tadaki, K. Shimizu, (eds.) K. Inoue, K. Mukherjee, K. Otsuka, H. Chen, *Displacive phase transformations and their applications in materials engineering.* TMS; 1998. p. 187.
- [59] S.K. Wu and C.M. Wayman, *Metallography* 20 (1987) 359.
- [60] S.K. Wu and C.M. Wayman, *Scripta Metallurgica* 21 (1987) 83.
- [61] N.G. Boriskina and E.M. Kenina, *Titanium Science and Technology, 4th International Conference on Titanium, 1980:* pp. 2917.
- [62] L.L. Meisner, V.N. Grishkov, V.P. Sivokha, (eds.) C. Youya, T.U. Hailing *International Symposium on Shape Memory Materials, International Academic Publishers, 1994:* pp. 263.
- [63] X.D. Han, W.H. Zou, R. Wang, Z. Zhang, D.Z. Yang, *Acta Metallurgica* 44 (1996) 3711.
- [64] L.L. Meisner, V.P. Sivokha, *Journal De Physique IV.* 5 (1995) C8.
- [65] Z. Pu, H. Tseng, K. Wu, *SPIE Conference: Smart Structures and Materials 1995: Smart Materials, 1995:* pp. 171–178.
- [66] R. Noebe, T. Biles, S. Padula, ‘NiTi-Based High-Temperature Shape-Memory Alloys: Properties, Prospects, and Potential Applications’, in: W. Soboyejo, T. Srivastan (Eds.), *Advanced Structural Materials: Properties, Design Optimization, and Applications*, CRC Press, 2007: p. 145.
- [67] H.C. Donkersloot and J.H.N Van Vucht, *Journal of Less Common Metals* 20 (1970) 83.

- [68] K. Otsuka, K. Oda, Y. Ueno, M. Piao, T. Ueki, H. Horikawa, *Scripta Metallurgica et Materialia* 29 (1993) 1355.
- [69] Y. Xu, K. Shimizu, Y. Suzuki, K. Otsuka, T. Ueki, K. Mitose, *Acta Materialia* 45 (1997) 1503.
- [70] NASA Glenn Research Center, High-Temperature Shape Memory Alloy Group, unpublished research, 2003.
- [71] T. Biggs, M.B. Cortie, M.J. Witcomb, L.A. Cornish, *Metallurgical and Materials Transactions A* 32 (2001) 1881.
- [72] G.S. Bigelow, S.A. Padula II, A. Garg, D. Gaydos, R.D. Noebe, *Metallurgical and Materials Transaction A* 41 (2010) 3065.
- [73] L.L. Meisner and V.P. Sivokha, *Physica B* 344 (2004) 93.
- [74] R.D. Noebe, D. Gaydos, S.A. Padula II, A. Garg, T Biles, and M. Nathal 2005. *Proceedings of SPIE*, 5760 (2005) 364.
- [75] S.F. Hsieh and S.K. Wu, *Materials Characterization* 41 (1998) 151.
- [76] D.N. AbuJdom, P.E. Thoma, M.Y. Kao, D.R. Angst, US patent #5114504; 1992.
- [75] D.R. Angst, P.E. Thoma, M.Y. Kao, *Journal of Physics IV C8* (1995) 747.
- [76] J. van Humbeeck, *Journal of Engineering Materials and Technology* 12 (1999)98.
- [77] G.S. Firstov, J. van Humbeeck, Y.N. Koval. *Material Science and Engineering A* 378 (2004) 2.
- [78] S.F. Hsieh and S.K. Wu, *Journal of Alloys and Compounds* 270 (1998) 237.
- [79] S.K. Wu and S.F. Hsieh, *Journal of Alloys and Compounds* 297 (2000) 294.
- [80] G.S. Firstov, J. van Humbeeck, Y.N. Koval. *Scripta Materialia* 50 (2004) 243.
- [81] R.D. Noebe, S. Draper, D. Gaydos, A. Garg, B. Lerch, N. Penney N, et al. 2008 *Proceedings of SMST* p. 409.
- [82] X.L. Meng, W. Cai, F. Chen, L.C. Zhao, *Scripta Materialia* 54 (2006) 1599.
- [83] C.C. Wojcik, *Journal of Materials Engineering and Performance* 18 (2008) 511.
- [84] X.D. Han, R. Wang, Z. Zhang, D.Z. Yang, *Acta Materialia* 46 (1998) 273.

- [85] A.M. Sandu, K. Tsuchiya, M. Tabuchi, S. Yamamoto, Y. Todaka, M. Umemoto, *Materials Transactions* 48 (2007) 432.
- [86] A. Evirgen, I. Karaman, R.D. Noebe, R. Santamarta, J. Pons, *Scripta Materialia* 69 (2013) 354.
- [87] W.J. Buehler, “Intermetallic Compound Based Materials for Structural Applications,” 7th NAVY Science Symposium: Solution to NAVY Problems Through Advanced Technology, Office of Naval Research, Arlington, VA, report number AD421708(64N15101), May 1963.
- [88] H. Hertz, “On the Contact of Rigid Elastic Solids and on Hardness”, *Verh. Ver. Beford, GewFleiss*, November 1882.
- [89] D. Dowson,; *History of Tribology*, Chapter 9, “The Industrial Revolution”, pages 187-285, Professional Engineering Publishing Limited, London, 1998.
- [90] D.H. Stone and R.K. Steele, “The Effect of Mechanical Properties Upon the Performance of Railroad Rails” *Rail Steels-Developments, Processing and Use*, ASTM STP 644, D.H. Stone and G.G. Knupp, (eds.), American Society for Testing Materials, 1978, pages 21-62.
- [91] T.L. Oberle, “Properties Influencing Wear of Metals”, *Journal of Metals*, June 1951.
- [92] A. Matthews and A. Leyland, “Design Criteria for Wear-Resistant Nanostructured and Glassy-Metal Coatings”, *Surface Coatings and Technology*, 177-178 (2004), pages 317-324.
- [93] C. DellaCorte, R.D. Noebe, M.K. Stanford, S.A. Padula, *Resilient and Corrosion-Proof Rolling Element Bearings Made from Superelastic Ni-Ti Alloys for Aerospace Mechanism Applications*, in: Y.R. Takeuchi, W.F. Mandler (eds.), *Rolling Element Bearings*, ASTM International, West Conshohocken, PA, 2012, p. 143-166.
- [94] C. DellaCorte, S.V. Pepper, R. Noebe, D.R. Hull, G. Glennon, “Intermetallic Nickel-Titanium Alloys for Oil-Lubricated Bearing Applications,” *NASA/TM 2009-215646* (March 2009).
- [95] C. DellaCorte, W.A. Wozniak, *Design and Manufacturing Considerations for Shockproof and Corrosion-Immune Superelastic Nickel-Titanium Bearings for a Space Station Application*, *NASA/TM 2012-216015* (May 2012).
- [96] R.R. Adharapurapu, F. Jiang, K.S. Vecchio, *Materials Science and Engineering A* 527 (2010) 1665.
- [97] H.E. Karaca, I. Kaya, H. Tobe, B. Basaran, M. Nagasako, R. Kainuma, Y. Chumlyakov *Materials Science and Engineering A* 580 (2013) 66.

- [98] E.J. Kirkland, R.F. Loane, J. Silcox, *Ultramicroscopy* 23 (1987) 77.
- [99] R.F. Loane, P. Xu, J. Silcox, *Ultramicroscopy*. 40 (1992) 121.
- [100] K. Thompson, D. Lawrence, D.J. Larson, J.D. Olson, T.F. Kelly, B. Gorman, *Ultramicroscopy* 107 (2007) 131.
- [101] L.A. Giannuzzi, *Microscopy and Microanalysis* 12 (2006) 1260.

## APPENDIX

## APPENDIX A

### A PROCEDURE FOR ESTABLISHING ISOCONCENTRATION SURFACES FOR THE DETERMINATION OF PRECIPITATE COMPOSITION AND VISUALIZATION<sup>5</sup>

#### **Abstract**

Proximity histograms, or proxigrams, are a prevailing means of representing compositional profiles between two phases. Though the technique has been around for over one decade, the procedures on how isoconcentration surfaces are selected is largely user defined, which can result in potential inconsistencies in how data is reported between users. This is particularly concerning in weakly partitioning systems where clear chemical segregation is not obvious. This paper addresses a methodology on how to identify the most appropriate elemental species and its value used to create the isoconcentration surface. From these selections, the highest fidelity visual representation of the precipitate and its compositional profile can be determined for atom probe data analysis. The case system used to illustrate these constructions is a Ni-Ti-Hf shape memory alloy.

<sup>5</sup> A manuscript has been prepared for the work in this chapter for publication in Ultramicroscopy.

## A.1 Motivation

Atom probe tomography has grown from its groundbreaking infancy as a field ion microscope, which allowed for the first viewing of individual atoms [1], to an established technique capable of generating 3D reconstructions with near atomic resolution [2-5]. The atom probe data can be represented in a variety of manners such as individual atom maps, 1-dimensional (1D) compositional profiles, 2-dimensional (2D) concentration maps, as well as isoconcentration or isodensity surfaces which highlight secondary phases within the microstructure [6-8]. In each representation, the quantitative capability of the atom probe is manifested in how atomic species partition within a microstructure.

In the past decade, wide field-of-view detectors have enabled the atom probe to reconstruct specimens over 100 nm in diameter with millions of ions being collected in the reconstructed volume [8-10]. These larger data sets have enabled more of the material's microstructural features to be captured, including entire precipitates. From these features, the compositional partitioning between the phases can be quantified. For example, by using a cylindrical data volume, the 1D compositional profile across the matrix-precipitate interface can be plotted by simply counting the number of atoms within the volume as a function of the distance within the cylinder. [7] If this cylinder is not perfectly normal to the interface, the interfacial profile can be wider than the actual partitioning behavior in the material resulting in a loss of fidelity. Moreover when the precipitates are small, the diameter of the cylinder must be decreased to ensure that it captures the correct feature size. A consequence of this reduction is an increase in the error of the measurement because of the lower atom count [7]. Hence, 1D profiles can be plagued with user defined settings that may not provide the necessary quantitative reproducibility between results.

In 2000, Hellman *et al.* [11] introduced the proximity histogram or proxigram to overcome several of these issues. The proxigram is based off of a pre-defined isoconcentration surface with the compositional profile determined normal to that surface on either side [11], as shown in Figure A.1. These surfaces provide clear visual representation of precipitate features that can allow direct cross-correlation comparison to more conventional imaging of such phases by transmission electron microscopy [12,13]. Using this surface, the summed values of the compositions across the entire surface as a function of distance out of and into the surface are used to generate the compositional profile. A major advantage of the proxigram is the ability to take repeatable compositional measurements normal to the surface, even if it is anisotropic or curved. This provides a reliable means of capturing the compositional interfacial gradient between phases.

The data in these proxigrams are binned by voxels. Hence, the voxel size is critical in determining how the compositional data is binned and quantified. Torres *et al.* [14] reported a means to determine the optimal voxel size as function of feature size in reconstructed atom probe data sets. As the voxel size decreased, the spatial resolution increased at the expense of the compositional certainty, and vice versa. Through simulated and experimental data sets, a procedure was established for determining the optimal voxel settings for a fixed delocalization setting that was kept constant at one-half of the voxel size. Felfer *et al.* [15] have also reported new approaches for determining how to bin data to increase the fidelity of the characterization. Clearly, how atom probe data is binned is critical in how the compositional results are interpreted.

Using the binned data, various visualization and compositional analysis methods are undertaken. Unfortunately, many atom probe results only report the voxel size without the

procedure of how that binning was optimized for that particular material. The establishment of procedures on how data is reconstructed, reported, and represented in data plots is essential in providing reproducibility between different research entities. A study by Hudson *et al.* [16] reported widely varying results for a simulated data set analyzed by a sample of over twenty experienced atom probe tomography (APT) users. The results revealed that the standard deviation between the true composition and that ranged by these users was as high as 22.60%; this extreme difference was noted for species that were the lowest in composition (1 at.%). Arguably, these differences between users can be tied to a lack of consistent procedures on how atom probe data is processed after its collection.

Here, a procedure for identifying the most appropriate isoconcentration surfaces is discussed and developed. The selection of the isoconcentration surface is paramount in how the proxigram will report the compositional profiles and how the microstructural features are visually represented. Simply stating the isoconcentration value in a reconstruction does not necessarily provide insight into how or why that value was chosen, yet its value significantly impacts the interpretation of the results. For the proxigram, the profiles are relative values to the selected isoconcentration surface. In the cases when chemical partitioning is clearly observed in the atom map, such as shown in Figure A.1, the identification of the isoconcentration species and the value that delineates the partitioned features are easily established. However, for specimens where chemical partitioning is weak or modest, the selection of the isoconcentration species and the value which created the visual surface can be an ambiguous decision.

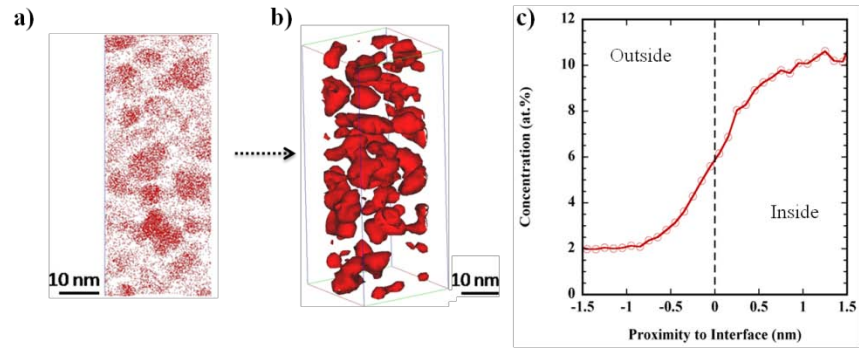


**Figure A.1.** (a) Fe atom map from a Co-Fe-Zr-Hf alloy showing clear Fe partitioning; (b) A 6 at.% isoconcentration surface for Fe; (c) Proxigram of the composition profile into and out of the defined isoconcentration surfaces. These images were adapted from those previously reported in reference [14].

In prior work done by the authors [17], a series of Ni-Ti-Pd shape memory alloys have been shown to precipitate a nanoscale P-phase that are instrumental in regulating the shape memory attributes of the alloy. Though the alloy was macro-alloyed with Pd, the chemical partitioning between the matrix and the precipitates, particularly at shorter aging times, was not visually obvious in any atom map. Subsequent work by the authors on other shape memory alloys, such as Ni-Ti-Hf [18], has also shown this weak partitioning behavior. Since chemical composition between phases is paramount in regulating the shape memory transformation temperature [19], the fidelity of the atom probe reconstructions and compositional data representations is essential. Using the Ni-Ti-Hf alloy as a case study, we provide a procedure on how to properly select the correct element to create the isoconcentration surface that gives the highest fidelity to how the species partition and are visually represented in the reconstruction. The results of which provide a more general procedure on how to approach atom probe reconstruction and data representation using existing analysis tools and methods for other alloys.

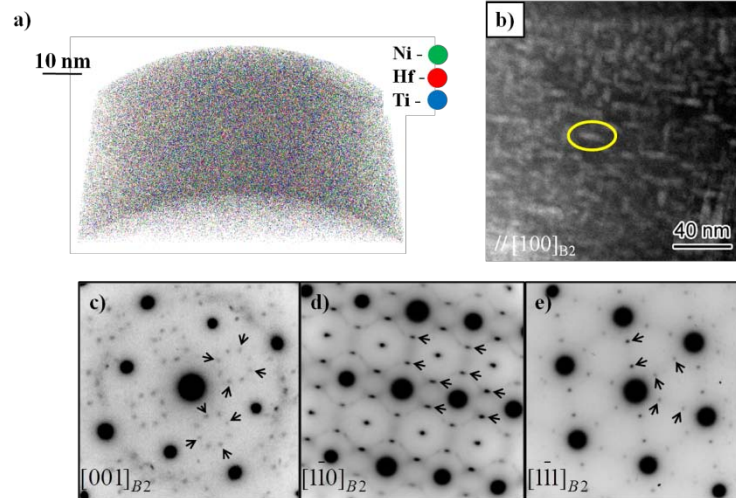
## A.2 Experimental

The atom probe specimen was taken from an ingot with a nominal composition of 50.3Ni-29.7Ti-20Hf (at.%). The specimen studied was solution annealed at 1050°C for 3 hours and immediately water quenched followed by an aging treatment at 550°C for 3 hours and water quenched. The 3 hours aged condition resulted in the precipitation of the H-phase [13,20]. All solution annealing and aging treatments were conducted in a tube furnace under a continuous flow of ultra-high purity Ar with the specimens wrapped in Ta foil to reduce oxidation of the specimen. Further details about the specimen can be found in reference [18].

The atom probe specimen was prepared using a Focused Ion Beam (FIB) lift-out procedure [21,22] in a FEI Quanta 200 3D dual scanning electron beam-FIB microscope equipped with an Omniprobe micromanipulation lift-out system. The atom probe analysis was performed on a Cameca 3D Local Electrode Atom Probe (LEAP) 3000XSi. The specimen was maintained at a base temperature of 30K (-243°C) and thermally assisted field evaporated using a laser at a pulse rate of 200 kHz, pulse energy 0.2 nJ, and a target evaporation set point at 0.5. The atom probe data was reconstructed using the IVAS 3.6.6 software package.

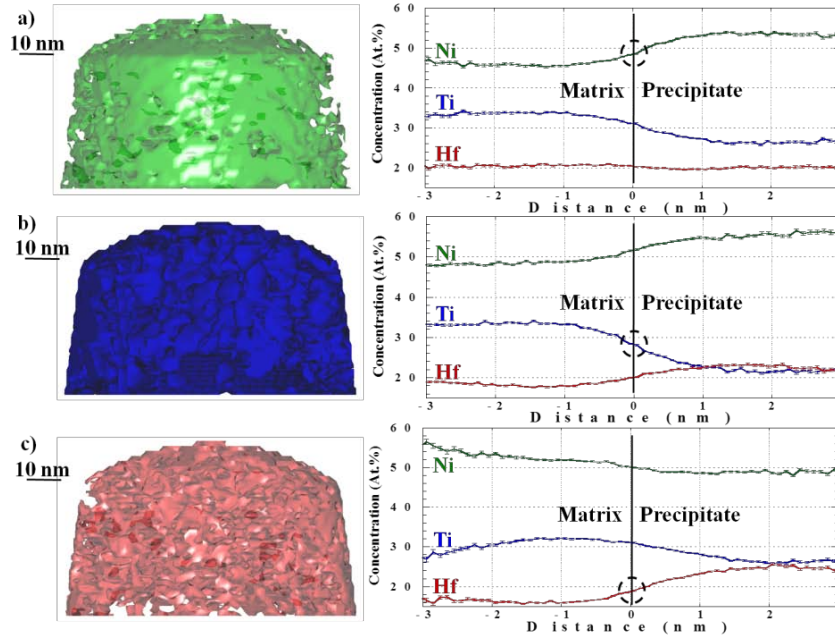
## A.3 Results and Discussion

Figure A.2(a) is the atom map of the 50.3Ni-29.7Ti-20Hf alloy aged at 550C for 3 hours. From this image no obvious partitioning of the species was observed. The STEM-HAADF image, Figure A.2(b), clearly showed the presence of nanoscale precipitates which were identified to be H-phase in the selected area electron diffraction patterns in Figure A.2 (c)-(e).



**Figure A.2.** (a) Atom map of 50.3Ni-29.7Ti-20Hf (at.%) aged 3 hours @ 550°C; (b) STEM-HAADF image of the same aged condition with Hf-enriched nanoscale precipitate present throughout the microstructure; (c) Selected area electron diffraction patterns from the [001],  $[1\bar{1}0]$  and  $[\bar{1}\bar{1}1]$  zone axes of the B2 phase with additional reflections (indicated with the arrows) indexed to the H-phase precipitate.

An isoconcentration surface for each element - Ni, Ti, and Hf respectively – are shown in Figure A.3. The value of the isoconcentration surface was determined by where the mid-point in the compositional profile is at ‘zero’ (referred to in this paper as the mid-point) on the proxigram. By selecting this compositional value for the isoconcentration surface, a user is able to center the profile relative to the matrix-precipitate interface where the compositional change in one species relative to another is approximately equal. For this particular alloy, these isoconcentration values are unable to yield a clear visual reconstruction that delineation the precipitates in the matrix.



**Figure A.3.** 50.3Ni-29.7Ti-20Hf (at.%) aged at 550°C specimen for 3 hours: **(a)** 48.39 at. % Ni isoconcentration surface and its corresponding proximity histogram with its mid-point marked with a dashed circle; **(b)** 28.24at.% Ti isoconcentration surface and its corresponding proximity histogram with its mid-point marked with a dashed circle; **(c)** 18.71at.% Hf isoconcentration surface and its corresponding proximity histogram with its mid-point marked with a dashed circle.

The high and low compositional values for each profile from the Figure A.2's proxigrams are tabulated in Table A.1. Using the composition of the precipitate phase, the isoconcentration surfaces are re-generated using these new values for each specific species, Figure A.4. In the IVAS 3.6 program, this data is referred to as the higher and lower gradient values with respect to the individual surfaces. Hence, the determination of the mid-point is critical in correctly identifying these high and low gradient compositional numbers. For certain species these new isoconcentration surfaces are able to clearly delineate the precipitate morphologies within the matrix. This is essential as the determination of the value and its relative encapsulation of the precipitate value will influence the microstructure quantification of number density, volume fraction, etc. For this system the Ti and Hf surfaces generate the precipitates with morphologies

most closely matching those seen in Figure A.2. The Ni surfaces clearly do not provide a good visual match thereby eliminating it as the proper choice for any further partitioning analysis.

**Table A.1.** The compositional values taken of the matrix and precipitate phase using the proxigrams in Figure A.3 for the 50.3Ni-29.7Ti-20Hf (at.%) alloy aged at 550°C for 3 hours. Note how the composition of the matrix and precipitate phase was altered by the choice of the isoconcentration value used for the Ni, Ti, and Hf species.

Phase Compositions from 48.39% Ni isoconcentration surface		Phase Compositions from 28.24% Ti isoconcentration surface		Phase Compositions from 18.71% Ti isoconcentration surface	
Matrix (at.%)	Precipitate (at.%)	Matrix (at.%)	Precipitate (at.%)	Matrix (at.%)	Precipitate (at.%)
Ni - 53.31	Ni - 46.27	Ni - 48.32	Ni - 54.59	Ni - 51.92	Ni - 48.97
Ti - 27.15	Ti - 33.14	Ti - 32.61	Ti - 23.44	Ti - 31.38	Ti - 28.33
Hf - 19.54	Hf - 20.59	Hf - 19.07	Hf - 21.97	Hf - 16.70	Hf - 22.69

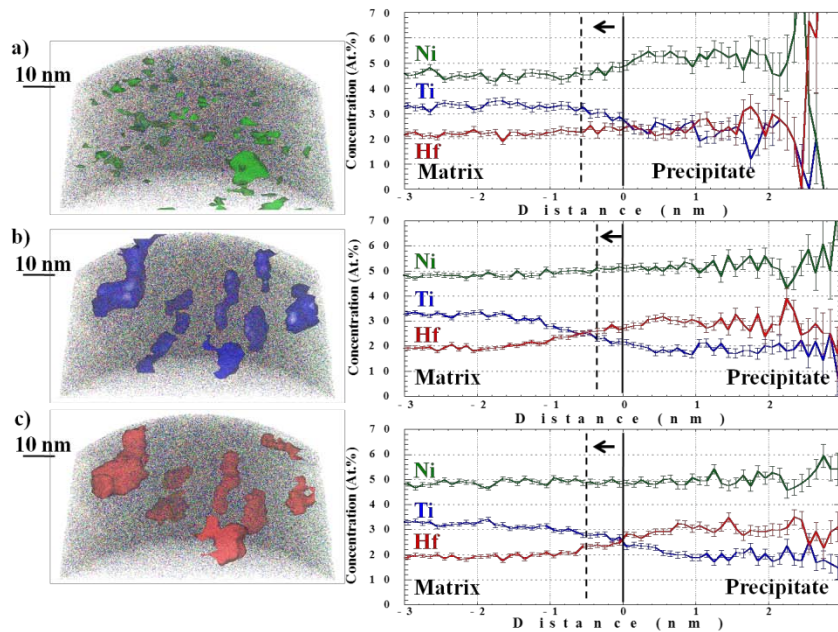


**Figure A.4.** 50.3Ni-29.7Ti-20Hf (at.%) aged at 550°C for 3 hours: (a) 46.27 at.% Ni isoconcentration surface and its proximity histogram generated using the listed Ni composition from the precipitate phase in the original 48.39 at.% Ni surface (Table A.1); (b) 23.44 at.% Ti isoconcentration surface and its proximity histogram generated using the listed Ti composition from the precipitate phase in the original 28.24 at.% Ti surface (Table A.1); (c) 22.69 at.% Hf isoconcentration surface and its proximity histogram generated using the listed Hf composition from the precipitate phase in the original 18.71 at.% Hf surface (Table A.1). Note the shift for all.

All three species showed a relative shift of the gradient profiles away from the mid-points where the compositional gradient changed, Figure A.4. Moreover, the highest and lowest compositional values for the matrix and precipitate phases in the proxigrams from Figure A.4 and tabulated in Table A.2 have deviated slightly from those seen from Figure A.3 and Table A.1. The compositional deviation, or error bar, also increased for the proxigrams in Figure A.4 as compared to those in Figure A.3. This increased error is because of the lower atom count in the smaller volume created by the re-generated surface. Hence, the creation of the most visually pleasing isoconcentration surface that may match the correct morphology does not necessarily yield the highest compositional fidelity profile. Based on these trends, compositional information should be extracted from the mid-point inflection procedures used in Figure A.3's proxigrams. Hence, the isoconcentration surface that yields the most visually pleasing reconstruction match may not necessarily be ideal for the compositional analysis.

**Table A.2.** The compositional values taken of the matrix and precipitate phase using the proxigrams in Figure A.4 for the 50.3Ni-29.7Ti-20Hf (at.%) alloy aged at 550°C for 3 hours. Note how the composition of the matrix and precipitate phase was altered by the choice of the isoconcentration value used for the Ni, Ti, and Hf species.

Phase Compositions from 46.27% Ni isoconcentration surface		Phase Compositions from 23.44% Ti isoconcentration surface		Phase Compositions from 22.69% Ti isoconcentration surface	
Matrix (at.%)	Precipitate (at.%)	Matrix (at.%)	Precipitate (at.%)	Matrix (at.%)	Precipitate (at.%)
Ni – 50.30	Ni – 52.23	Ni – 50.30	Ni – 51.55	Ni – 50.31	Ni – 49.44
Ti – 29.72	Ti – 23.70	Ti – 29.76	Ti – 19.09	Ti – 29.77	Ti – 21.04
Hf – 19.98	Hf – 24.07	Hf – 19.94	Hf – 29.36	Hf – 19.92	Hf – 29.52

Though Ti and Hf yield more idealized isoconcentration surfaces that match the precipitates' true morphology, the proxigram profiles used for the compositional determination for each phase, Figure A.3, have compositional trends (and values) that differ between the Ti and Hf surface, i.e. the Ni appears enriching the precipitate for the Ti-based surface and depleting in the precipitate with the Hf-based surface. This is critical to shape memory alloys as the Ni:Ti

ratio has a significant influence on the transformation temperature. To determine which species should be used as the isoconcentration surface that yields the highest compositional fidelity, a 1D profile is sliced through the isoconcentration surfaces in Figure A.4 for direct comparison. These 1D profiles are shown in Figure A.5. Though this type of composition profile may not be ideal for the reasons listed in the introduction section, it does not bias how the atoms are counted to a predefined surface. Rather it simply counts the species as a function distance. This profile clearly indicates Ti depletion and Hf and Ni enrichment in the precipitate. Comparing this profile to the proxigrams in Figure A.3, the proxigram generated from the Ti based isoconcentration surface was in the best agreement. In both profiles, the species partitioning behavior to each phase was the same. The advantage of the proxigram, as compared to the 1D profile, is seen by its reduced error in the compositional uncertainty as a function of distance since it is able to provide an aggregate average over all the precipitate in the analyzed tip volume. In addition, the proxigram profile is computed to being truly normal to the interface to yield a higher fidelity in the compositional width.

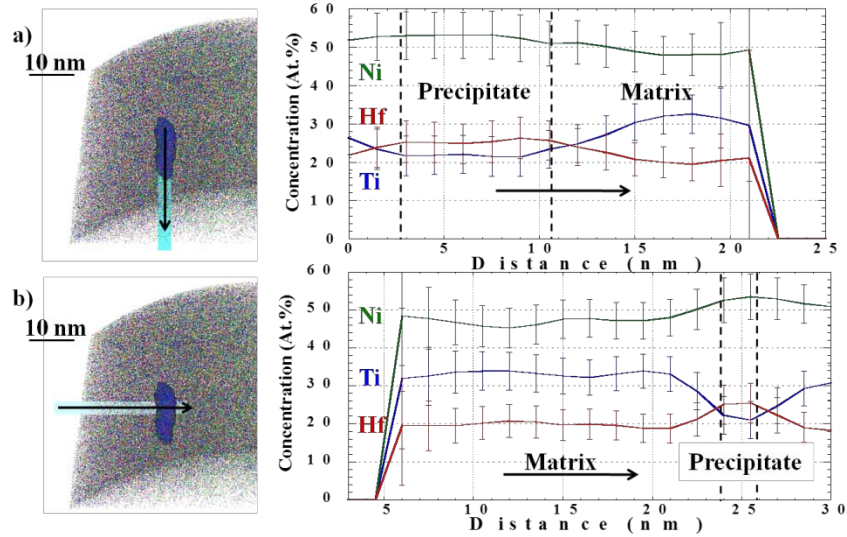


**Figure A.5.** 50.3Ni-29.7Ti-20Hf (at.%) aged 3 hours @ 550°C specimen: **(a)** Atom map with a precipitate isoconcentration surface displayed showing the cylinder used to generate the corresponding 1D profile; **(b)** Atom map with a precipitate isoconcentration surface displayed showing the cylinder, turned 90 degrees to generate a second orientation, used to generate the corresponding 1D profile.

#### A.4 Conclusion

Atom probe data sets by their very nature allow different means of visualization and data analysis. This paper has reported a procedure in how to identify isoconcentration surfaces that optimize both compositional and visual representations of precipitates within a microstructure. These procedures provide standardization practices in how one may consistently reconstruct atom probe data from proxigrams for quantitative analysis within a system and between systems where chemical partitioning occurs. As noted, the isoconcentration surfaces used to yield the most visually pleasing agreement to the morphology in the microstructure may not necessarily be the best suited surfaces to create the proxigrams for the compositional analysis. Rather by combining a series of steps and surfaces, one is able to achieve both needs in the atom probe data analysis. These steps are summarized below:

1. Create an isoconcentration surface at the value where that particular species exhibits an midpoint (or inflection point) in composition where it is equally divided between the two phases. This proxigram has the highest counting statistics (lowest error) in determining the composition between the two phases. From this surface, the high and low compositional values from each profile can be generated.
2. Using these values relative to the initial species' isoconcentration surfaces, a new surface is generated based on the precipitate phase's composition. At least one of these new surfaces yields features with morphologies consistent with the precipitate phase. This step in the procedure lends itself to the generation of the best visual representation of the precipitates, though it was found these proxigrams are not ideal for the compositional analysis.
3. Returning to the initial midpoint based proxigrams (#1 above), the compositional profiles are better for the overall compositional analysis of the matrix and precipitate phases. To determine which species' isoconcentration surface should be used for the compositional analysis from the proxigram, a 1D compositional profile should be placed through the precipitate surface generated in step #2. The compositional values and trends from this 1D profile that best matches the individual species' midpoint proxigram identifies that proxigram as the one with the highest compositional fidelity to the multi-phase material.

## **A.5 References**

- [1] E.W. Müller, K. Bahadur, Field Ionization of Gases at a Metal Surface and the Resolution of the Field Ion Microscope, *Physical Review* 102 (1956) 624.

- [2] L. Yao, M.P. Moody, J.M. Cairney, D. Haley, A.V. Ceguerra, C. Zhu, S.P. Ringer, Crystallographic structural analysis in atom probe microscopy via 3D Hough transformation, *Ultramicroscopy* 111 (2011) 458.
- [3] M.P. Moody, B. Gault, L.T. Stephenson, D. Haley, S.P. Ringer, Qualification of the tomographic reconstruction in atom probe by advanced spatial distribution map techniques, *Ultramicroscopy* 109 (2009) 815.
- [4] M.P. Moody, B. Gault, L.T. Stephenson, R.K.W Marceau, R.C. Powles, A.V. Ceguerra, A.J. Breen, S.P. Ringer, Lattice rectification in atom probe tomography: toward true three-dimensional atomic microscopy, *Microscopy and Microanalysis* 17 (2011) 226.
- [5] D.J. Larson, B. Gault, B.P. Geiser, F. De Geuser, F. Vurpillot, Atom probe tomography spatial reconstruction : Status and directions, *Current Opinion in Solid State and Materials Science* 17 (2013) 236.
- [6] E.A. Marquis, J.M. Hyde, Applications of atom-probe tomography to the characterization of solute behaviours,” *Material Science and Engineering R.* 69 (2010) 37.
- [7] M.K. Miller, Atom Probe Tomography, Springer Publishing, 2000.
- [8] B. Gault, M.P. Moody, J.M. Cairney, S.P. Ringer, Atom Probe Microscopy, Springer Publishing, 2012.
- [9] J. Bunton, D. Lenz, J. Olson, K. Thompson , R. Ulfing, D. Larson, T. Kelly, Instrumentation Developments in Atom Probe Tomography: Applications in Semiconductor Research, *Microscopy and Microanalysis* 12 (2006) 1730.
- [10] B.P. Geiser, D.J. Larson, E. Oltman, S. Gerstl, D. Reinhard, T.F. Kelly, T.J. Prosa, Wide-Field-of-View Atom Probe Reconstruction, *Microscopy and Microanalysis* 15 (2009) 292.
- [11] O.C. Hellman, J.A. Vandenbroucke, J. Rüsing, D. Isheim, D.N. Seidman, Analysis of Three-dimensional Atom-probe Data by the Proximity Histogram, *Microscopy and Microanalysis* 6 (2000) 437.
- [12] V. Radmilovic, A. Tolley, E.A. Marquis, M.D. Rossell, Z. Lee, D. Dahmen, Monodisperse Al<sub>3</sub>(LiScZr) core/shell precipitates in Al alloys, *Scripta Materialia* 58 (2008) 529.
- [13] F. Yang, D.R. Coughlin, P.J. Phillips, L. Yang, A. Devaraj, L. Kovarik, R.D. Noebe, and M.J. Mills, *Acta Materialia* 61 (2013) 3335.
- [14] K.L. Torres, M. Daniil, M.A. Willard, and G.B. Thompson, The influence of voxel size on atom probe tomography data, *Ultramicroscopy* 111 (2011) 464.

- [15] P. Felfer, A. Ceguerra, S.P. Ringer, J.M. Cairney, Applying computational geometry techniques for advanced feature analysis in atom probe data, *Ultramicroscopy* 132 (2013) 100.
- [16] D. Hudson, G.D.W. Smith, B. Gault, Optimisation of mass ranging for atom probe microanalysis and application to the corrosion processes in Zr alloys, *Ultramicroscopy* 111 (2011) 480.
- [17] T.T. Sasaki, B.C. Hornbuckle, R.D. Noebe, G.S. Bigelow, M.L. Weaver, and G.B. Thompson, Effect of Aging on Microstructure and Shape Memory Properties of a Ni-48Ti-25Pd (At. Pct) Alloy, *Metallurgical and Materials Transaction A* 44 (2013) 1388.
- [18] B.C. Hornbuckle, T.T. Sasaki, G.S. Bigelow, R.D. Noebe, M.L. Weaver, G.B. Thompson, Under submission to *Material Science and Engineering A* (Chapter 2 in dissertation).
- [19] W. Tang, Thermodynamic Study of the Low-Temperature Phase B19' and the Martensitic Transformation in Near-Equatonic Ti-Ni Shape Memory Alloys, *Metallurgical and Materials Transactions A* 28 (1997) 537.
- [20] X.D. Han, R. Wang, Z. Zhang, D.Z. Yang, A new precipitate phase in a TiNiHf high temperature shape memory alloy, *Acta Materialia* 46 (1998) 273.
- [21] K. Thompson, D. Lawrence, D.J. Larson, J.D. Olson, T.F. Kelly, B. Gorman, In situ site-specific specimen preparation from atom probe tomography, *Ultramicroscopy* 107 (2007) 131.
- [22] L.A. Giannuzzi, Reducing FIB Damage Using Low Energy Ions, *Microscopy and Microanalysis* 12 (2006) 1260.